

6201 924

2

AD-A279 405

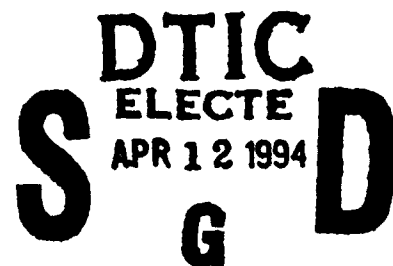


PL-TR-94-2018

**SOURCE CONTRIBUTIONS AT
FAR-REGIONAL DISTANCES**

**Karl Koch
Brian Stump**

**Southern Methodist University
Department of Geological Sciences
Dallas, TX 75275**



12 December 1993

Scientific Report No. 1

QHP **94-11039**

Approved for public release; distribution unlimited



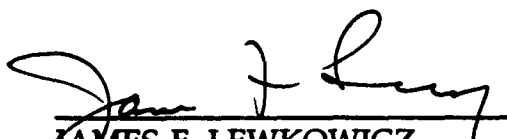
**PHILLIPS LABORATORY
Directorate of Geophysics
AIR FORCE MATERIEL COMMAND
HANSCom AIR FORCE BASE, MA 01731-3010**

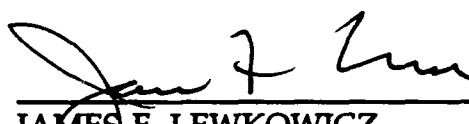
DTIC QUALITY INSPECTED 3


94 4 11 132

The views and conclusions contained in this document are those of the authors and should not be interpreted as representing the official policies, either express or implied, of the Air Force or the U.S. Government.

This technical report has been reviewed and is approved for publication.


JAMES F. LEWKOWICZ
Contract Manager
Solid Earth Geophysics Branch
Earth Sciences Division


JAMES F. LEWKOWICZ
Branch Chief
Solid Earth Geophysics Branch
Earth Sciences Division


JAMES F. LEWKOWICZ, Acting Director
Earth Sciences Division

This report has been reviewed by the ESC Public Affairs Office (PA) and is releasable to the National Technical Information Service (NTIS).

Qualified requestors may obtain additional copies from the Defense Technical Information Center. All others should apply to the National Technical Information Service.

If your address has changed, or if you wish to be removed from the mailing list, or if the addressee is no longer employed by your organization, please notify PL/TSL, 29 Randolph Road, Hanscom AFB, MA 01731-3010. This will assist us in maintaining a current mailing list.

Do not return copies of this report unless contractual obligations or notices on a specific document requires that it be returned.

REPORT DOCUMENTATION PAGE			Form Approved OMB No. 0704-0188	
Public reporting burden for this collection of information is estimated to average 1 hour per response, including the time for reviewing instructions, searching existing data sources, gathering and maintaining the data needed, and completing and reviewing the collection of information. Send comments regarding this burden estimate or any other aspect of this collection of information, including suggestions for reducing this burden, to Washington Headquarters Services, Directorate for Information Operations and Reports, 1215 Jefferson Davis Highway, Suite 1204, Arlington, VA 22202-4302, and to the Office of Management and Budget, Paperwork Reduction Project (0704-0188), Washington, DC 20503.				
1. AGENCY USE ONLY (Leave blank)		2. REPORT DATE 12 December 1993		3. REPORT TYPE AND DATES COVERED Scientific No. 1
4. TITLE AND SUBTITLE Source Contributions at Far-Regional Distances			5. FUNDING NUMBERS PE 69120C PR T121 TA TC WU AA Contract F19628-91-K-0016	
6. AUTHOR(S) Karl Koch Brian Stump				
7. PERFORMING ORGANIZATION NAME(S) AND ADDRESS(ES) Southern Methodist University Department of Geological Sciences Dallas, TX 75275			8. PERFORMING ORGANIZATION REPORT NUMBER	
9. SPONSORING / MONITORING AGENCY NAME(S) AND ADDRESS(ES) Phillips Laboratory 29 Randolph Road Hanscom AFB, MA 01731-3010 Contract Manager: James Lewkowicz/GPEH			10. SPONSORING / MONITORING AGENCY REPORT NUMBER PL-TR-94-2018	
11. SUPPLEMENTARY NOTES				
12a. DISTRIBUTION / AVAILABILITY STATEMENT Approved for public release; distribution unlimited			12b. DISTRIBUTION CODE	
<p>13. ABSTRACT (Maximum 200 words) In order to investigate source contributions at far-regional distances (as far as 2000 km), a reliable model of the upper mantle structure is necessary. In many cases successful discriminants are based on the S wave part of far-regional seismograms including Sn, Sg, Lg and surface waves. Therefore it is mandatory to place corresponding weight on constraining the upper mantle S wave structure for the region under consideration.</p> <p>This current report hence provides an investigation of the mantle shear structure for the Western U.S. from body and surface wave inversion. Earthquakes on the coast of northern California and off the coast off southern Oregon ($5.5 < M_s < 7.1$) have provided a set of data at LTX showing clear mantle S arrivals that become very impulsive at distances near 2400 km. The great circle paths for these events to LTX coincide with the LTX-NTS path. These data allow the interpretation of the S velocity structure for the Western U.S. to depths of the upper mantle transition zone from the body waves and give constraints for the shallower structure from surface waves from inversion of Rayleigh and Love waves, summarized in the two papers contained in this report.</p>				
14. SUBJECT TERMS regional seismograms - upper mantle - shear velocity structure - waveform matching - surface wave inversion			15. NUMBER OF PAGES 94	
			16. PRICE CODE	
17. SECURITY CLASSIFICATION OF REPORT Unclassified	18. SECURITY CLASSIFICATION OF THIS PAGE Unclassified	19. SECURITY CLASSIFICATION OF ABSTRACT Unclassified	20. LIMITATION OF ABSTRACT SAR	

CONTENTS

ON SHORT PERIOD MANTLE S WAVES FOR LARGE REGIONAL PROPAGATION PATHS IN THE WESTERN UNITED STATES	1
1. Introduction	2
2. Data Set	3
3. Focal Mechanisms	7
4. Travel Time Analysis	7
5. Synthetic Seismograms	10
6. Conclusion	14
References	17
 CONSTRAINTS FOR UPPER MANTLE SHEAR WAVE MODELS OF THE BASIN AND RANGE FROM SURFACE WAVE INVERSION	 39
1. Introduction	40
2. Data and Dispersion Analysis	41
3. Surface Wave Inversion	44
Single Event Love Wave Data	46
Average Love Wave Data	46
Average Rayleigh Wave Data	47
Simultaneous Inversion of Love and Rayleigh Waves	47
4. Discussion and Conclusion	48
References	51
Appendix: A Summary of the Theory of Phase-Matched Filtering	53

Accession For	
NTIS CRA&I	<input checked="" type="checkbox"/>
DTIC TAB	<input type="checkbox"/>
Unannounced	<input type="checkbox"/>
Justification	
By _____	
Distribution /	
Availability Codes	
Dist	Avail and/or Special
A-1	

ON SHORT-PERIOD MANTLE S WAVES FOR LARGE REGIONAL PROPAGATION PATHS IN THE WESTERN UNITED STATES

Karl Koch
Southern Methodist University
Department of Geological Sciences
Dallas, TX 75275-0395

Abstract

Five earthquakes ($5.5 < M_s < 7.1$) in the Mendocino/Gorda plate region on the coast of Northern California and off the coast of Southern Oregon were recorded at Lajitas, Texas (LTX) at distances of 2200-2500 km. The waveforms at LTX exhibit mantle S waves that become impulsive beyond 2300 km. Previously studied far-regional seismograms of waves propagating across the Basin and Range to LTX (ranges less than 1800 km) demonstrated that at these shorter distances the only identifiable shear arrival was the Lg phase and thus could not be used to constrain upper mantle S structure. Mantle P waves were found to generate the dominant first arrivals beyond 1200 km and constrain the P wave structure of the upper mantle to 200 km depth.

The new data reported here allow the extension of the S velocity model for the Western U.S. to the upper mantle transition zone. The great circle paths for these events to LTX coincide with the LTX-NTS path that was used in earlier studies, with rays bottoming beneath NTS. Travel times for these mantle S phases at distances larger than 2400 km are close to those predicted for PcP, but the ground motion is transversely polarized. Teleseismic and regional velocity models do not predict the observed arrival times. Synthetic reflectivity seismograms further show, that models with large 400 and 700 km discontinuities introduce waveform complexities that are not observed. A new model has been developed characterized by a low velocity region extending to 400 km depth followed by a gradient zone between 400 and 700 km fitting the travel times as well as amplitude observations. This new model compares favorably at these depths with the surface wave model WUS of Cara (1979) although WUS includes lower velocities in the upper 200 km and hence predicts arrival times that are delayed by 10-15 sec relative to the observations. The revised velocity model along with source constraints from the Harvard-CMT solutions is used to model the S wave ground motion. The excellent agreement in

absolute amplitude and waveshape between the observations and the synthetic data further validates the new model. This modeling exercise also shows how regional broadband data can be used to constrain the source depth to within a few kilometers when the propagation path is well calibrated.

1. Introduction

The structure of the Earth's upper mantle has been the subject of extensive study starting in the last decade, as high-quality digital data and advanced computational methods provided the opportunity to investigate the three-dimensional (3-D) distribution of structural parameters. Global studies of 3-D models of the upper mantle are mostly based on fundamental and higher mode surface waves (e.g. Woodhouse & Dziewonski, 1984; Romanowicz, 1990; Tanimoto, 1990) and free oscillations (e.g. Roult et al., 1990) describing lateral heterogeneity within the Earth in terms of higher order angular velocity anomalies. Since surface waves are strongly dependent on the shear velocities of the near-surface structure, these 3-D models focus on shear velocity variations within the upper mantle.

Other studies have considered mantle shear heterogeneity on a regional scale. Shear wave studies of North America include those by Priestley & Brune (1978) and Cara (1979) using surface wave data, and a second group using long period body waves, i.e. Helmberger & Engen (1974), Grand & Helmberger (1984), or Grand (1987). Although the global 3-D models argue for lateral heterogeneities throughout the entire upper mantle on a world-wide scale, regional studies often attribute lateral variations between different regions to the depth range above 400 km (e.g. Grand & Helmberger, 1984), and assume that the deeper upper mantle is fairly homogeneous, at least on the regional scale. These models may only include large scale heterogeneities since longer period data are used and thus localized structures might be averaged along the propagation path.

Although global and regional 3-D models have strong lateral variations, they are usually based on standard earth models, like e.g. PREM (Dziewonski & Anderson, 1981) or TNA (Grand & Helmberger, 1984), which, as simple 1-D-models, include several discontinuities within the upper mantle. Extensive work has been done to map the depth of the well-established 400 and 700 km discontinuities (which are

also sometimes referred to as 420 km and 660 km discontinuities, respectively) on a global scale using underside reflections from these discontinuities and comparison with later arriving corresponding surface reflections for both P and S waves (Nakanishi, 1988; Shearer & Masters, 1992). While the reflections from the 700 km discontinuity are quite stable, the 400 km discontinuity is more intermittent. Results from these studies indicate a topographic change on the order of 30 km for the 700 km discontinuity.

The subject of this study is the constraint of the western US regional shear velocity model from far-regional seismograms to depths that include the two upper mantle discontinuities with a less ambitious 1-D model and to fill a void between regional and teleseismic investigations. In a previous study (Koch & Stump 1993), the upper mantle structure of the Basin and Range province was investigated with short period and broadband regional data. It was found that P phases turning in the upper mantle at depths of less than 200 km, dominate the P waves at distances larger than 1200 km. In contrast, no corresponding S arrivals from the upper mantle could be unambiguously identified for distances less than 1800 km.

A number of magnitude 6 events in July/August 1991, however, provided the first observable mantle S phases at distances between 2200 and 2400 km, or 20-22 degrees, respectively. As the events were in a small source region in the Cape Mendocino/Gorda plate area and we used data from a single station, their great circle path are nearly identical. The rays are therefore sampling the same region suggesting a simple 1-D interpretation is applicable implying that waveform changes are the result of waves bottoming at different depths and not lateral variations in the structure. This geometry, the mismatch of observed arrival times with global and regional models and the simplicity of the waveforms motivated this study as they provide strong constraints on the upper mantle transition zone in the western U.S. by travel time analysis and extensive synthetic waveform modeling. The results are then discussed with respect to global and regional 3-D models.

2. Data Set

The set of observations used in this study consists of the seismograms recorded at Lajitas, TX (LTX) from five earthquakes on the coast of Northern California and off the shore of Southern Oregon. Four earthquakes with magnitudes greater than 6 in

July and August 1991 with a fifth event in Jan. 1990 provided a set of data with clear S arrivals that turn in the upper mantle. Similar arrivals were not observed from events at distances less than 1800 km. The locations are summarized in Table 1, along with moment tensor source parameters published by Harvard and the USGS. Two of the events at 2200 km were located on shore, while the epicenters of the three remaining events were about 200 km offshore. The station and event locations with their great circle paths are displayed with a schematic outline of the Basin and Range province in Figure 1. Also shown in the figure are radial and transverse component seismograms at LTX from the Loma Prieta event, indicating a relatively weak arrival only identifiable on the broadband transverse component. However, these data were only used here in the travel time analysis, as the event had a different azimuth from all other events. Event locations in California and the Nevada Test Site (NTS) studied earlier in Koch & Stump (1993) at distances less than 2000 km are also shown which show no shear arrivals for closer events. The primary motivation for our study was the fact that these earthquake data (2200-2500 km) are located so that their great circle paths to LTX coincides with the path from NTS to LTX, with the rays bottoming in the vicinity of NTS.

Data are recorded at LTX with three-component, short-period velocity transducers (SP) with eigenfrequency of 1 Hz and three-component broad-band accelerometers (BB) with linear amplification to 5 Hz. Two events with superior S/N ratios are illustrated in the following figures, where representative data for one on-shore event [event #4, Table 1 - 1991229(1)] are shown in Figure 2 and for one event off the coast [Event #2, Table 1 - 1991194] are reproduced in Figure 3. Both events are about the same magnitude ($m_b=6.0$) and at the same, shallow depth (≈ 10 -12 km, see Table 1) and thus should include similar source excitation and source depth effects.

The waveforms from event #4 (near coast of N. California at 2219 km) are characterized by a high-frequency P wave, two secondary arrivals, and surface waves (Figure 2). The short period records emphasize the P waves at ~ 20 sec from the (arbitrary) trace origin as well as the Lg phase at about 400 sec. The broad-band seismograms emphasize the first S arrival and the long-period surface waves. Rotating the horizontal broad band records into radial and transverse components results in a good separation of Rayleigh waves on the vertical and radial component and Love waves on the transverse component. Based on this single record it is difficult to unambiguously identify the first S arrival (mantle S wave) as primarily

SV or SH. The transverse waveform is higher frequency than on the radial or vertical component, why it is speculated that the transverse energy of this mantle S arrival is primarily due to scattering close to the station. It should also be noted that Lg can be observed for the Basin and Range propagation to distances of at least 2200 km, where Lg has the strongest energy of all later arrivals.

The data of the more distant event in Figure 3 (#2; off coast of Oregon at 2431 km) has a comparable P wave but shows a significantly different first S arrival, which is clearly developed in both the SP and BB records. This arrival is pronounced on both horizontal components and after rotation appears as an isolated impulsive signal in the transverse direction. This SH phase is much simpler than the S waves from the previous event, while the radial component shows an emergent arrival with a low amplitude, long duration wavetrain similar to the on-shore event (Figure 2). The off-shore event has no clearly identifiable L_g phase, even after high-pass filtering the data to eliminate Love wave contributions arriving at about the same time. Although the epicentral distance of the first event was only 200 km shorter, it had a strong Lg phase. The second event is off the coast and thus the missing L_g energy must be blocked when it encounters the transition from oceanic to continental crust. As the P and S arrivals sample the deeper upper mantle they seem relatively unaffected by this lateral transition. An important result from this observed Lg blockage however is, that the fate of a strong Lg phase is decided in the immediate vicinity of the source as a path length variation of only 10 percent can produce this remarkable pattern.

The radial and transverse broadband records from all five events are compared in Figures 4(a,b) in order to further identify event to event phase variations and document range effects. The Rayleigh waves (Figure 4a) from the two closest events (no.1 and 4, Table I) are almost identical on the radial seismograms. The mantle S arrival and the Loves waves (Figure 4b), following the fundamental mode arrival, show large variations for these 2 events. All 3 events in the 2400 km range show nearly identical seismograms from the onset of the mantle S wave to some 10 cycles into both Rayleigh and Love waves. Later arriving surface wave energy shows more significant differences. These variations may in part be attributed to the source itself, whether it is a source depth or spectral excitation effect. The complexity of the mantle S wave on the radial component might be associated with the source excitation as illustrated by the second and third trace from the top, which are

relatively small events ($m_b < 6$). In these traces the mantle SV arrival is of high frequency compared to the lower frequency character for the other events. The strong SH motion for distances larger than 2300 km appears to be unaffected by source differences as this S phase has the same simple waveform for all three events, even for the third trace that showed high frequency SV arrivals. These observations are used later to constrain the size of the upper mantle discontinuities.

In order to evaluate spectral differences between individual earthquakes, the broadband (acceleration) data were used to calculate spectra for the P wave and mantle S wave arrivals on the vertical, radial and transverse components of motion. Since no instrument corrections have been made, the spectra will exhibit a f^2 slope for the spectral plateau at long periods and a flat spectrum where the source spectra decay as f^{-2} . Figure 5a shows an example of the P wave amplitude spectra for event #2 (Figure 3, Table 1) and Figure 5b displays the amplitude spectra of the mantle S wave for the same event. Prior to spectral estimation, a 10% cosine taper was applied to the beginning and end of each 102.4 sec-long window. The given noise spectra, taken from 20 sec windows prior to the P arrival, demonstrate the signal-to-noise ratio and the bandwidth of the data from 100 sec to the antialias filter corner at about 4 Hz. Although the focus in this paper is on the mantle S waves, the P wave spectras may give additional information in characterizing source differences for the two clusters of events.

The vertical and radial spectra for the P wave generally compare well while the transverse component, reflective of the scattered P wave energy, is 2-5 times smaller at longer periods. The P spectra for all 5 events have a plateau between 0.1 and 0.5 Hz. For the mantle S wave spectra there is a significant shift of the spectral peaks to lower frequencies, which can be expected (Hanks & Wyss, 1972). The two closer events show no spectral separation between all three components and have a simple, peaked spectrum around 0.1-0.2 Hz, supporting the argument of scattered SV on the transverse component. For the larger distances of 2400 km the transverse motion mantle S gives considerably larger amplitude spectra as documented in Figure 5b. The spectra have a narrow plateau below 0.1 Hz nearly independent of source size, which can be interpreted as all S frequencies near and higher than the corner frequency being strongly attenuated on their propagation path. This in turn indicates that the Q for shear waves in the upper mantle must be considerably lower than for P waves.

3. Focal Mechanisms

In order to quantify the effect of source mechanisms on the seismograms of individual events, we have used the available moment tensor solutions of all examined events (Table 1) and compare their major double-couple fault-plane solutions in Figure 6. The objective was to determine whether the particular mantle S wave observations can be attributed in part to different source orientations.

All but one event are represented by primarily strike-slip mechanisms with planes striking about NE-SW or NW-SE, respectively. These mechanisms fit the tectonic model for Gorda plate earthquakes (Dengler et al., 1991), which show left-lateral faulting on NE planes. Since Lajitas is at an azimuth of about 120° , we expect maximum SH radiation from the strike-slip events. The only abnormal event in the sequence (#4 in Table 1 - 08/17/91), located on the coast of Northern California and referred to as the Honeydew earthquake (Oppenheimer et al., 1991), shows a dominant thrust component in the moment tensor solutions. Previous work by Oppenheimer et al. (1991) and McPherson et al. (1991) indicates the active fault for this event strikes NW-SE and dips between $45\text{--}55^\circ$.

Comparison of the two closest events (#1, 4 in Table 1), located in the same area but having different source mechanisms, was used in estimating the significance of these source effects. The strong similarities between the waveforms for these events (Figures 4/ upper two traces), suggests that the source mechanism differences do not lead to the major difference in the mantle S wave observations. Differences in source size might produce small waveform variations as suggested by the spectral comparisons.

4. Travel Time Analysis

The far-regional events of this study between 2200 and 2500 km (Table 1) and the events from Koch & Stump (1993) provide a data set to investigate travel times across the Basin and Range from 800 to 2500 km as first step in constraining the

shear wave model. The travel times at these distances can be compared with predictions from a variety of upper mantle models, spanning regional to teleseismic wave propagation. We have considered standard travel time tables (Jeffreys-Bullen (JB), 1958; Herrin, 1968; Kennett & Engdahl, 1991), which are based on global travel time observations, and travel times from regional models (e.g. Cara, 1979; Grand & Helmberger, 1984) for initial comparison with the data.

The arrival times for P, L_g , and mantle S (S_m) phases were picked and first contrasted against standard travel time tables. P waves and L_g phases are observed throughout the source-receiver range while the mantle S wave observations are only available at the greatest ranges. No L_g observations were made beyond 2200 km, where L_g is blocked at the oceanic-continental crustal transition. The travel times of P and S (a weak mantle S is present beyond about 1900 km; Koch & Stump, 1993), follow the trend of the JB as well as the Herrin times. However, there is a significant delay, on the order of 10-20 seconds, for the mantle S arrivals relative to the JB model. The P times are much more consistent with both the JB and Herrin travel time curves. To quantify these results we compare the travel time differences of the observations to the Herrin (only for P) and JB times in Figure 7a. The P arrival data seem to follow the JB table clustering around 0 sec residual with a scatter on the order of a few seconds. This scatter may be due to our assumption of surface foci adopted for the shallow nuclear explosion and crustal events in California, source location errors introduced through the source-receiver distance, and origin time errors.

A new set of tables (IASPEI-91) for regional and teleseismic observations has recently been proposed by Kennett & Engdahl (1991). These tables were derived from a high quality data set of arrivals gathered between 1964 and 1987. While the JB tables were established with arrival times of limited accuracy, the new tables promise more overall travel time consistency. We tested our set of travel times with this new model (IASPEI-91). A plot of the main phases for these tables with the data is shown in Figure 7b. The P travel times match the model with a similar scatter as for JB while the shear arrivals beyond 2000 km are some 15 sec late relative to the model. This result is consistent with differences found in the JB model comparison. It is important to note that the core-mantle reflection, PcP, crosses the mantle S wave travel time curve between 20-22°. The complexity of the vertical and radial component mantle S arrivals documented in Figures 2-4 was initially attributed to the interference of the S and PcP travel time branches, although PcP should be small

in amplitude for a distance of 20° and for a strike-slip mechanism. The mantle S arrival, as exemplified by the simple pulse on the transverse component (Figure 4b) must not be strongly affected by multipathed PcP with its steep incidence angle (less than 12°).

In order to explain the variations in observed travel times and ultimately model the mantle S waveforms, additional global and regional velocity models were considered. The teleseismic models included PREM (Dziewonski & Anderson, 1981) and 1066B (Gilbert & Dziewonski, 1975), while the regional models were those from Cara (1979) (WUS) and Grand & Helmberger (1984) (TNA, SNA). The shear velocity models are summarized in Figure 8a. Additional models that were developed from previous work (Koch & Stump, 1993) are also included. The SNA model of Grand & Helmberger (1984) was included for completeness, but is not considered a suitable candidate, as it was developed for the shield area of the Eastern U.S, while we are concerned in this study with shear wave propagation in the tectonically active Western U.S. There is great variation in the upper mantle for the velocity distribution for the different models, with shear velocity ranging from 4.3 - 4.8 km/sec just below the Moho and 4.0-4.4 km/sec in the low velocity zone, often associated with the ductile asthenosphere. In spite of these differences at shallower depths, the velocities are similar at the 400 km discontinuity with a shear velocity of 4.7 km/sec. Except for Cara's WUS model and the ones developed in this study, all other models are quite similar in their structure between 400 and 700 km with significant velocity discontinuities at each depth. Due to the similarity of many models we emphasize models 1066B and WUS in the following discussion.

Travel times for the two representative upper mantle shear models were calculated and compared in Figure 8b with the observations. Both models include a single crustal layer with a velocity of 3.5 km/sec, which is consistent with the Lg arrivals to 2000 km. The upper mantle S wave arrival times are not well explained by either 1066B nor WUS. Although 1066B shows several travel time branches at this distance range, none of these branches matches the slope of the mantle S arrivals. In addition, the first arrivals are too early. The S arrival times of WUS are 10-15 sec late between 2000-2500 km. The slope of the traveltime branches for this model appears to be in better agreement with the observations. The travel time branches shown for WUS result from shear waves bottoming below the asthenosphere. The late arrival time predictions suggest that the velocities for the WUS asthenosphere

are too low producing the large delays. The slope of the arrival times for the mantle S waves between 20 and 22° suggests that the WUS model below the asthenosphere might be appropriate for modelling shear waves propagating in this upper mantle depth range. Travel time curves for a new model, discussed in the section below, which is close to the velocity distribution of WUS in the 400-700 km depth range, and which match the observations well, are also shown.

5. Synthetic Seismograms

Due to the sparsity of the mantle S observations, the upper mantle model to be adopted for the Basin and Range province can not and should not be constrained from travel time analysis alone. One strength of this study is that a high quality set of seismograms from a common station have been recorded that are: (1) high dynamic range; (2) broadband; and (3) three component. The waveform data, as discussed above, show a distinct transition zone between 2200 and 2400 km distance, where the SH wave transforms from an emergent and complex arrival to a simple and high-amplitude waveform. With the aid of synthetic seismograms, these waveform variations were used to constrain the shear model particularly where velocity discontinuities can introduce travel time triplications and associated waveform complexities.

The waveform modeling technique chosen is the extended reflectivity method (Müller 1985), which provides the opportunity to simultaneously model P, S, L_g , Love and Rayleigh waves at regional distances. This methodology was used in a previous modelling study of far-regional data (Koch & Stump, 1993) and is warranted by the very narrow range of propagation paths (see Figure 1). The previous study focused on distances less than 1800 km and produced synthetic seismograms that match arrival times, frequency content and duration of individual regional phases. Since there were no identified mantle S wave arrivals at these distances (< 1800 km), there was only limited constraint placed on the upper mantle shear structure. This new work extends the regional shear wave model to greater observation distances, where mantle shear arrivals are observed, and hence to greater depths within the upper mantle. One disadvantage of the reflectivity model is that it is one-dimensional and thus existing lateral variations in the velocity structure cannot be taken into account. The use of this modelling

technique is thus seen as a first simple characterization of the propagation path effects. The simplicity of the shear arrivals shown in Figure 4b argues that 1-D models may be quite successful. The consistency of arrival times, relative and absolute amplitudes and wave packet duration between observations and synthetics will be used as a measure of the effectiveness of the 1-D model.

A double-couple source mechanism was used for the reflectivity calculations according to the strike-slip mechanisms shown in Figure 6 (strike, dip, slip: 314° , 74° , -175° , resp.). The source duration was set to 2 sec as a lower bound and intended to include the higher frequency contributions from smaller events. This duration was also required as the source wavelet used (Brüstle & Müller, 1983) has a f^{-4} decay, thus underestimating higher frequencies that are found in the mantle P waves and the Lg phases. Calculations were done at a sampling rate of 8 Hz with an effective bandwidth from 0.05-2 Hz. The source depth for all synthetic calculations was assigned a constant value of 5 km in order to keep the temporal separation of S and sS small and minimize additional waveform complexities that were not observed.

The first set of synthetic SH seismograms (Figure 9) was calculated for the 1066B velocity model (Gilbert & Dziewonski, 1975), which includes distinct upper mantle discontinuities in the transition zone. A complex waveform pattern was found for the SH motion in the distance range between 2200 and 2400 km, as is suggested by the triplications in the travel time calculations. The feature easiest to identify in these seismograms is the arrival from the forward branch below 400 km and the reflection from the 700 km discontinuity both contributing to an extended wavetrain. The reflections from this model extend backwards in distance to less than 2000 km and hence the velocity distribution and particularly the discontinuities in this shear wave model are not supported by our observations. The Q_θ values used for the shear waves were 200 in the crust and topmost mantle and 80 in the low velocity layer down to the 400 km discontinuity, close to values suggested in PREM (Dziewonski & Anderson, 1981). Below 400 km Q_θ was increased to between 300 and 400. Radial seismograms, not shown here, have a rapidly growing mantle S arrival starting at about 1600 km resulting from the velocity distribution in the 400-600 km depth range, again not observed in the data. Reflections from the upper mantle discontinuities produce significant SV energy for distances greater than 2000 km which are much more complicated than those observed (Figure 4a). With a crustal velocity of 3.5 km/sec and a Moho shear wave

speed of 4.76, model 1066B produces an efficient Lg wavetrain, which can be propagated beyond 20° distance, much like the observations. These initial synthetic waveforms show that the velocity model parameters between 400 and 700 km depth are quite important in reproducing the mantle S phases observed between 20 and 22°.

It is this depth range that will be the focus of our modeling exercise. The WUS model of Cara (1979) offers an alternate velocity structure in this depth range incorporating a relatively smooth gradient in the transition zone without any first order discontinuities. This second model was tested if capable of predicting the observed mantle S wave pattern at Lajitas. The corresponding synthetic SH seismograms for this model are shown in Figure 10. The mantle SH phase produced by this model shows a simple and impulsive arrival near 2400 km, while arrivals for shorter distances are emergent. The energy in the synthetic seismograms at 1600 km is produced by the strong positive gradient around 300 km depth. For this model we have also used Q values similar to those for model 1066B. Although not shown here, the mantle S arrival on the radial component is also more like the observations although the amplitudes of the first cycle are overestimated at 2400 km.

A third model is introduced based upon a revision of the model proposed by Koch & Stump (1993) extending the shear velocities to greater depths. Previously a constant velocity in the LVZ of the upper mantle was assumed due to the lack of mantle S energy for distances less than 1500 km. The complexities in the shear waves introduced by velocity discontinuities in the 400-700 km depth range of 1066B are not found in our observations. Thus, the discontinuities in the shear model were removed and a simple velocity gradient for S below 400 km was introduced into the regional model. This model however delayed the shear arrivals of the synthetics by more than 30 sec. A positive shear velocity gradient has to be introduced below the lid in order to compensate for this delay. The SH waveforms for this case are shown in Figure 11a, and exhibit some minor shear arrivals at distances less than 2200 km. By systematically decreasing the negative jump to the low velocity layer and reducing the size of the positive gradient above 400 km depth, the mantle S wave contributions can be further reduced (Figure 11b).

As both 1066B and WUS include a negative gradient below the Moho, we developed an alternative model, where the transition to the low velocity zone in the upper mantle is represented by a negative gradient zone to about 150 km and the velocity turns smoothly to positive values. This model compensates for the travel times of phases propagating through the deeper upper mantle, while the smaller positive gradient above 400 km does not produce significant amplitudes for turning rays. The gradient in the transition zone below 400 km depth was however held fixed. The transverse synthetic seismograms are shown in Figure 12a. They show small mantle S contributions for all distances less than 2400 km, while maintaining the location of the transition zone to strong mantle S arrivals.

The vertical seismograms corresponding to those in Figure 12a are shown in Figure 12b. All three models presented before, produce similar SV contributions as shown in this figure, where the waveforms are somewhat more impulsive than the observations. The amplitudes of the mantle S waves for the radial component is smaller than the amplitudes generated by models 1066B and WUS. Further work refining the P structure throughout the considered depth range should eliminate some of these discrepancies. In particular, the size and depth of the 400 and 700 km discontinuities in the Western U.S. has to be studied with respect of producing significant SV contributions from reflections and conversions.

In a comparison of synthetic seismograms from all the models (see Figure 8), we display the synthetic data from the mantle S onset to a few cycles into the surface waves for the two distinguished distances of 2200 and 2400 km in Figure 13. While most seismograms show reasonably strong mantle S arrivals at the larger range, only WUS and the model developed in this study show only minor mantle S energy at the shorter distance. Due to a non-causal Q in the reflectivity calculations, the seismograms tend to have a low frequency swing before the arrival as well as a 6 sec early arrival time. To compensate for this effect as well as to the range difference of about 30 km between observations and synthetics, the synthetic seismograms were shifted by 12 seconds. The bottom seismograms and the observations (bold lines) are well matched from the mantle S arrival through the Love waves, which will be used to further constrain of the uppermost part of the S wave model in another paper.

While most of the synthetic seismogram comparisons to this point were qualitatively, i.e. displaying trace-normalized data, we have tried to match the absolute amplitudes of the mantle shear arrivals for two off-shore events. We used both short-period and broadband data in this comparison, which is shown in Figure 14. We ran synthetic seismogram calculations for events #2 and #3 from Table 1, with the source parameters (moment, source duration) for a Brune source model as given by the Harvard-CMT solutions listed in Table 1, and a source mechanism of a vertical strike slip with one fault plane striking N45E. Both waveforms, broadband and short-period, at either distance are matched in amplitude and duration by our model, although the first down-swing in the synthetics may mostly be due to the acausal Q model used in the calculations. An interesting result from this waveform matching is that the source depth of the point source in the calculations was constrained to 5 km, and is very much controlled by the short period data. When using larger source depths, the delay between S and sS in the SH seismograms becomes too large, and therefore the match especially for the higher frequency event #3 (right side of Figure 14) decreases. Absolute amplitude comparisons for the shorter ranges show, that absolute amplitudes are underestimated from the synthetic seismograms, supporting to some extent the interpretation as mostly scattered or multipathed SV energy. Thus, it appears that careful waveform modelling can be used to constrain event depth at these distances (20-22°) using mantle S arrivals.

6. Conclusions

We have identified strong mantle S arrivals at Lajitas for events at distances greater than 2000 km. For distances less than 1800 km, Koch & Stump (1993) could not identify any coherent arrivals between the initial P waves and Lg in short period and broad band data and the only S observations are emergent arrivals for broadband data from the Loma Prieta event. New observations between 20 and 22° show large amplitude, simple phases on the transverse component of motion between these phases. These mantle shear phases can be attributed to the shear velocity structure between 400-700 km, which is best modelled by a strong velocity gradient.

There is no evidence from our data that the P and S velocity discontinuities at 400 and 700 km, incorporated in standard teleseismic Earth models, are significant for the S structure of the upper mantle beneath the Western U.S. These discontinuities, if as large as given in previous models, would produce much more complicated shear arrivals than those observed at Lajitas. In contrast, the simple pulses observed argue for smooth velocity changes in both vertical and horizontal directions, if present at all. It further indicates that the 1-D modeling applied in this study is fully adequate for the observations in the distance range of 20-22°.

This result compares favorably with the shear velocity distribution derived by Cara (1979), except that his model appears to be too slow through the low velocity zone, producing travel time differences with the observations of 10-15 sec. The tectonic model of Grand & Helmberger (1984) follows the basic trend of model 1066B and is thus not adequate for our Lajitas data. The extended low velocity zone reaching down to 400 km, which was modelled with low Q, has been identified in other regions. Bowman & Kennett (1991) report a deep low-velocity zone under the Australian shield, inferred from travel time delays of up to 20 sec relative to the IASPEI-91 model. They compared these low velocities with tomographic images of the upper mantle, which predict high velocities for the Australian shield to depths of 400 km and greater. While most tomographic inversions show a high-velocity area for the Australian shield, the image is less clear for the upper mantle under the Western U.S. Tanimoto (1988) or Roullet et al. (1990) show that this region is not associated with an anomalously high or low velocity. Grand's (1987) study, however, finds a low-velocity anomaly in the upper 400 km compared to TNA for the Western U.S. This result is somewhat at odds with the results obtained here, as TNA has smaller velocities in the upper 150 km. It is interesting to note, that Grand's result for the 405-670 km depth range shows a change from a negative anomaly in the 405-490 km range to a slightly positive anomaly for the 575-670 km depth range, which is consistent with the gradient zone we have introduced in the transition zone (Figure 8).

The Q_g structure adopted throughout this work incorporated a value of 100 below the Moho and about 70-80 in the low-velocity zone to 400 km depth. These values were taken from standard earth models. Using higher values for Q_g produces significant arrivals from the mantle in the depth range between 200-400 km. Only the model used in Figure 12 produces a less pronounced increase of these mantle S

amplitudes for higher Q_β and is thus favored. Higher Q_β might however not be warranted as Al-Khatib & Mitchell (1991) have found Q values as low as 15 for the upper mantle of the Western U.S. from surface wave analysis. Lay & Wallace (1988) also found very low Q values of about 95 for multiple ScS data. Amplitudes of reflected phases from the upper mantle discontinuities can be reduced by lower Q values above the transition zone; therefore, a trade-off between Q and impedance across a discontinuity exists. This apparent trade-off between upper mantle shear structure and low Q_β values needs to be further addressed through a detailed quantitative study of absolute amplitudes from additional mantle S wave data, although matching of absolute amplitudes was successful in this study. Additional work appears to be warranted with the P -velocity structure for the quantitative interpretation of radial and vertical seismograms.

Acknowledgements

Data at the Lajitas station are acquired through the efforts of Prof. E.Herrin and his team, which provided access to their data. Brian Stump is thanked for his interest and fruitful reviews of the manuscript. This work was sponsored by the Air Force/Phillips Laboratory under contract F19628-91-K-0016.

References

- Al-Khatib, H. & B.Mitchell (1991): Upper mantle anelasticity and tectonic evolution of the western United States from surface wave attenuation, *J.Geophys.Res.*, **96**, 18129-18146
- Bowman, J.R. & B.L.N.Kennett (1991): Seismic travel times and a deep low-velocity zone beneath the Australian shield, (abstract), *EOS*, **72(44)**, 317
- Brüster, W. & G.Müller (1983): Moment and duration of shallow earthquakes from Love-wave modelling for regional distances, *Phys.Earth Planet.Int.*, **32**, 312-324
- Cara, M. (1979): Lateral variations of S velocity in the upper mantle from higher Rayleigh modes, *Geophys.J.R.astr.Soc.*, **57**, 649-670
- Dengler, L.A., G.Carver & B.McPherson (1991): Potential sources of large earthquakes in North coastal California, (abstract), *EOS*, **72(44)**, 315
- Dziewonski, A.M. & D.L.Anderson (1981): Preliminary reference Earth model, *Phys. Earth Planet.Int.*, **25**, 297-356
- Gilbert, F. & A.Dziewonski (1975): An application of normal mode theory to the retrieval of structural parameters and source mechanisms from seismic spectra, *Phil.Trans. Roy.Soc.*, **A278**, 187-269
- Grand, S.P. & D.V.Helmberger (1984): Upper mantle shear structure of North America, *Geophys.J.R.astr.Soc.*, **76**, 399-438
- Grand, S.P (1987): Tomographic inversion for shear velocity beneath the North American plate, *J.Geophys.Res.*, **92**, 14065-14090
- Hanks, T.C. & M.Wyss (1972): The use of body-wave spectra in the determination of seismic-source parameters, *Bull. Seism.Soc.Am.*, **62**, 561-589
- Helmberger, D.V. & G.R. Engen (1974): Upper mantle shear structure, *J.Geophys. Res.*, **79**, 4017-4028
- Herrin, E.T. (1968): Introduction to "1968 seismological tables for P-phases", *Bull. Seism.Soc.Am.*, **58**, 1193-1195
- Jeffreys, H. & K.E.Bullen (1958): Seismological tables, British Association Seismological Committee, London
- Kennett, B.L.N. & E.R.Engdahl (1991): Travel times for global earthquake location and phase identification, *Geophys.J.Int.*, **105**, 429-465
- Koch, K. & B.Stump (1993): Implications for upper mantle structure in the Western United States from complete far-regional seismograms, submitted to *Bull.Seism.Soc.Am.*

- Lay, T. & T.C.Wallace (1988): Multiple ScS attenuation and travel times beneath western North America, *Bull.Seism.Soc.Am.*, 78, 2041-2061
- McPherson, B.C, L.Dengler & D.Oppenheimer (1991): Evidence of compressional tectonics in the Kings range, California: the 1991 Honeydew earthquake, (abstract), *EOS*, 72(44), 315
- Müller, G. (1985): The reflectivity method: a tutorial, *J.Geophys.*, 58, 153-174
- Nakanishi, I. (1988): Reflections of P'P' from upper mantle discontinuities beneath the mid-Atlantic ridge, *Geophys.J.*, 93, 335-346
- Oppenheimer, D.H. & M.E.Magee (1991): The 1991 M6.0 Honeydew, California, earthquake, (abstract), *EOS*, 72(44), 311
- Priestley, K. & J. Brune (1978): Surface waves and the structure of the Great Basin of Nevada and western Utah, *J.Geophys.Res.*, 83, 2265-2272
- Romanowicz, B. (1990): The upper mantle degree 2: constraints and inferences from global mantle wave attenuation measurements, *J.Geophys.Res.*, 95, 11051-11071
- Roult, G., B.Romanowicz & J.P.Montagner (1990): 3-D upper mantle shear velocity and attenuation from fundamental mode free oscillation data, *Geophys.J.Int.*, 101, 61-80
- Shearer, P.M. & T.G.Masters (1992): Global mapping of topography on the 660-km discontinuity, *Nature*, 355, 791-796
- Tanimoto, T. (1990): Long-wavelength S-wave velocity structure throughout the mantle, *Geophys.J.Int.*, 100, 327-336
- Woodhouse, J.H. & A.M.Dziewonski (1984): Mapping the upper mantle: three-dimensional modeling of Earth structure by inversion of seismic waveforms, *J.Geophys.Res.*, 89, 5953-5986

Table 1: Summary of event parameters ^{o)}

No.	Date	Origin Time	Latitude	Longitude	Depth	M _B	M _{sz}	Range ^{†)}	D
1	01/16/1990(016)	200822.0	40.232N	124.138W	2	5.1	5.5	2223	
2	07/13/1991(194)	025014.7	42.182N	125.641W	11	6.2	6.9	2431	
3	08/16/1991(228)	222617.2	41.697N	125.385W	10	5.5	6.3	2395	
4	08/17/1991(229)	192940.0	40.235N	124.348W	12	6.0	6.2	2219	
5	08/17/1991(229)	221714.7	41.821N	125.397W	14	6.2	7.1	2397	

Harvard - Centroid Moment Tensor

No.	OT	Lat.	Long.	Depth	HD	P	Pl	Az	T	Pl	Az	N	Pl	Az	Mo(DC)	α	δ	λ
1	200830.6	40.06N	124.94W	15.0	2.2	1.73	0	262	0.46	90	180	-2.19	0	172	2.0e17	37	90	0
2	025020.8	42.09N	125.86W	15.6	10.4	2.07	7	271	-0.03	78	36	-2.04	10	180	2.1e19	128	75	179
3	222618.9	41.23N	125.56W	15.0	6.1	3.21	20	261	-0.16	67	113	-3.05	11	355	3.1e18	40	68	6
4	192942.3	40.02N	124.38W	15.0	3.9	2.09	60	103	-0.40	14	348	-1.70	27	251	1.9e18	173	73	104
5	221720.8	41.71N	125.63W	15.0	13.1	4.55	22	273	-0.24	62	53	-4.31	16	177	4.4e19	46	86	28

USGS - Moment Tensor Solutions

No.	Depth	P	Pl	Az	T	Pl	Az	N	Pl	Az	Mo(DC)	α	δ	λ
1	-	-	-	-	-	-	-	-	-	-	-	-	-	-
2	6	1.80	10	87	0.18	80	253	-1.98	2	356	1.9e19	131	81	175
3	13	3.81	8	82	-0.02	81	287	-3.79	4	173	3.8e18	218	82	3
4	6	3.39	56	40	-0.09	28	184	-3.30	17	283	3.3e18	171	68	59
5	12	2.33	1	93	0.00	77	185	-2.33	13	3	2.3e19	47	82	-9

^{o)}

NEIC: PDE - Monthly Listings

^{†)}

Epicentral distance to Lajitas, TX (LTX) from QED's

Figure Captions

- 1: Upper part: Sketch map of the Basin and Range showing location of station Lajitas (LTX) and epicenters with great circle paths - also shown are event locations used by Koch & Stump (1993); outlines and labels are: (B-R) Basin and Range, (C-P) Colorado Plateau; lower part: short period and broad band seismograms (R-radial component, T-transverse comp.) at LTX from the Loma Prieta earthquake (solid circle in upper part).
- 2: Three-component seismograms for event #4 (1991229 (1) - see Table 1) from (a) short-period velocity instrument, (b) broad-band accelerometer data and the (c) BB traces rotated into radial and transverse component
- 3: Three-component seismograms for event #2 (1991194 - see Table 1); see Figure 2 for further details
- 4: Seismogram sections for radial (a) and transverse (b) seismograms demonstrating mantle S wave development between 20° and 22°. The mantle S phase on the radial component shows little variability while the transverse component is very impulsive near 2400 km.
- 5: Spectra of P wave and mantle S wave segment for vertical, radial and transverse component for data shown in Figure 3c. Left panel shows time windows analyzed. The noise spectra were calculated from 20 sec windows prior to the P wave. P wave data (acceleration) show spectral plateau characteristic for f^2 slope, while missing in S wave spectra indicating strong attenuation of higher S frequencies
- 6: Moment tensor solutions for all five events. Both HRV and USGS solutions show strike-slip types except for one thrust event. The simple double couple mechanism, representative for all strike slip events was used in the waveform modelling.
- 7: Comparison of differential travel times at LTX with (a) the Jeffreys-Bullen (JB) and Herrin tables for the P and S waves, and (b) the IASPEI-91 tables for

all identified phases. P times are predicted consistently while mantle S arrival times are later than expected.

- 8: Regional/teleseismic S wave velocity models and corresponding calculated travel time curves (1066B-dashed, TNA-dotted, this study-solid lines). None of previous models is able to predict mantle S wave data.
- 9: Reflectivity seismograms from model 1066B for the transverse component (SH seismograms) at distances between 600 and 2400 km.
- 10: Reflectivity seismograms for model WUS (see also Figure 9) (SH seismograms) for regional distances
- 11: Reflectivity seismograms for upper mantle model with thin lid and two different sets of LVZ velocities and gradient zones in the upper mantle and gradient zone between 400 and 700 km depth; (a) large gradient and small velocity in LVZ, (b) higher velocity in LVZ and smaller gradient
- 12: Synthetic seismograms for upper mantle model with negative gradient in LVZ and smallest positive gradient to 400 km depth. As in Figure 11, zone with strong velocity gradient between 400 and 700 km depth; (a) transverse component (SH seismograms), (b) vertical component (P-SV seismograms)
- 13: Synthetic seismogram comparison for upper mantle models from Figure 8 at the two crucial distances of 2200 and 2400 km. The observed data and the synthetics from the model developed here are highlighted by bold lines.
- 14: Absolute waveform matching for events #2 (left side) and #3 (right side) in Table 1 and the synthetic data from Figure 12. Both short-period (top) and broad-band (bottom) recordings are shown. Broadband velocity seismograms were high-pass filtered at 1 Hz for simulation of SP records and were differentiated for the BB data. The timing was adjusted by delaying the synthetics by 2 and 3 seconds, respectively.

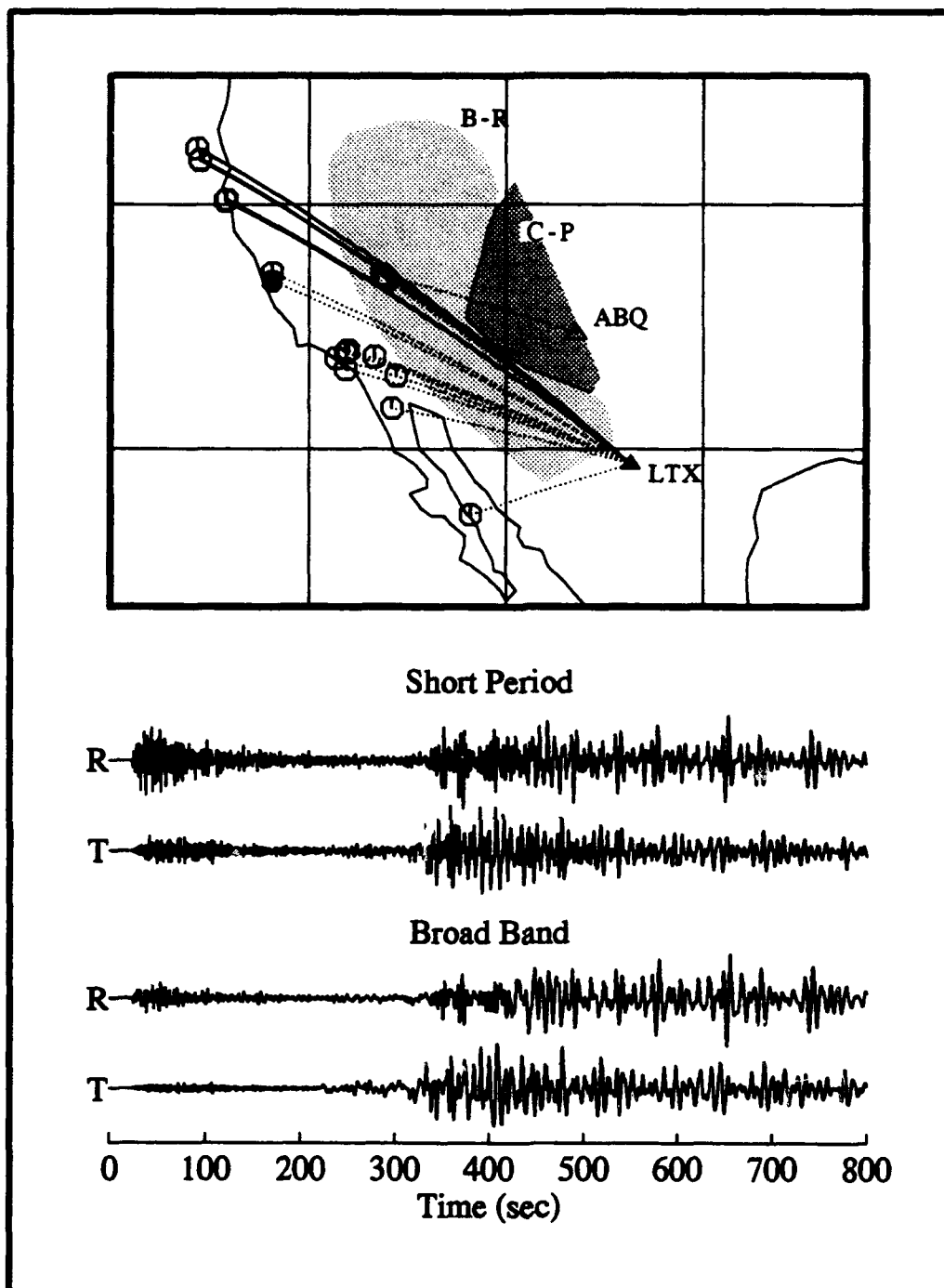


Figure 1

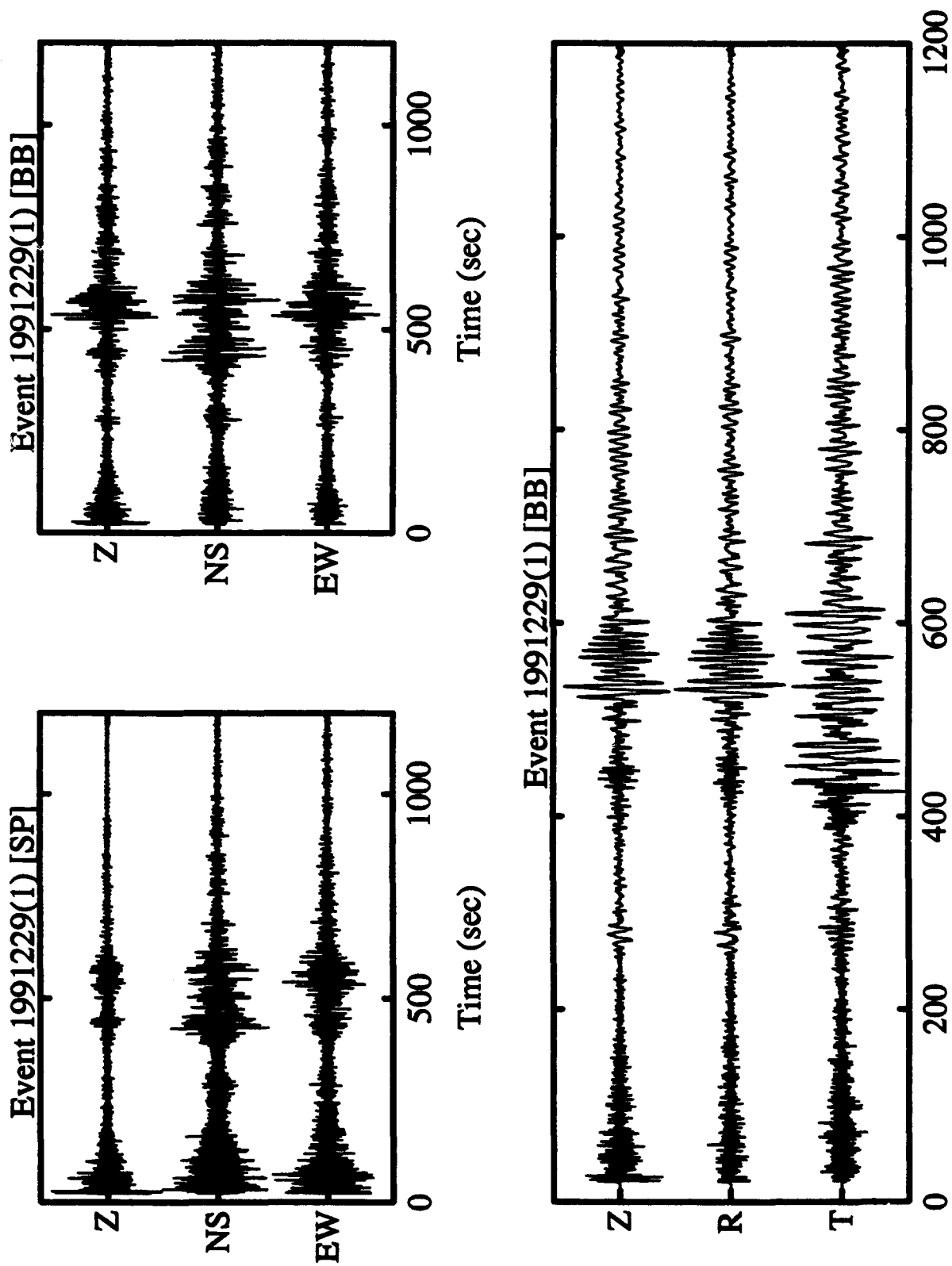


Figure 2

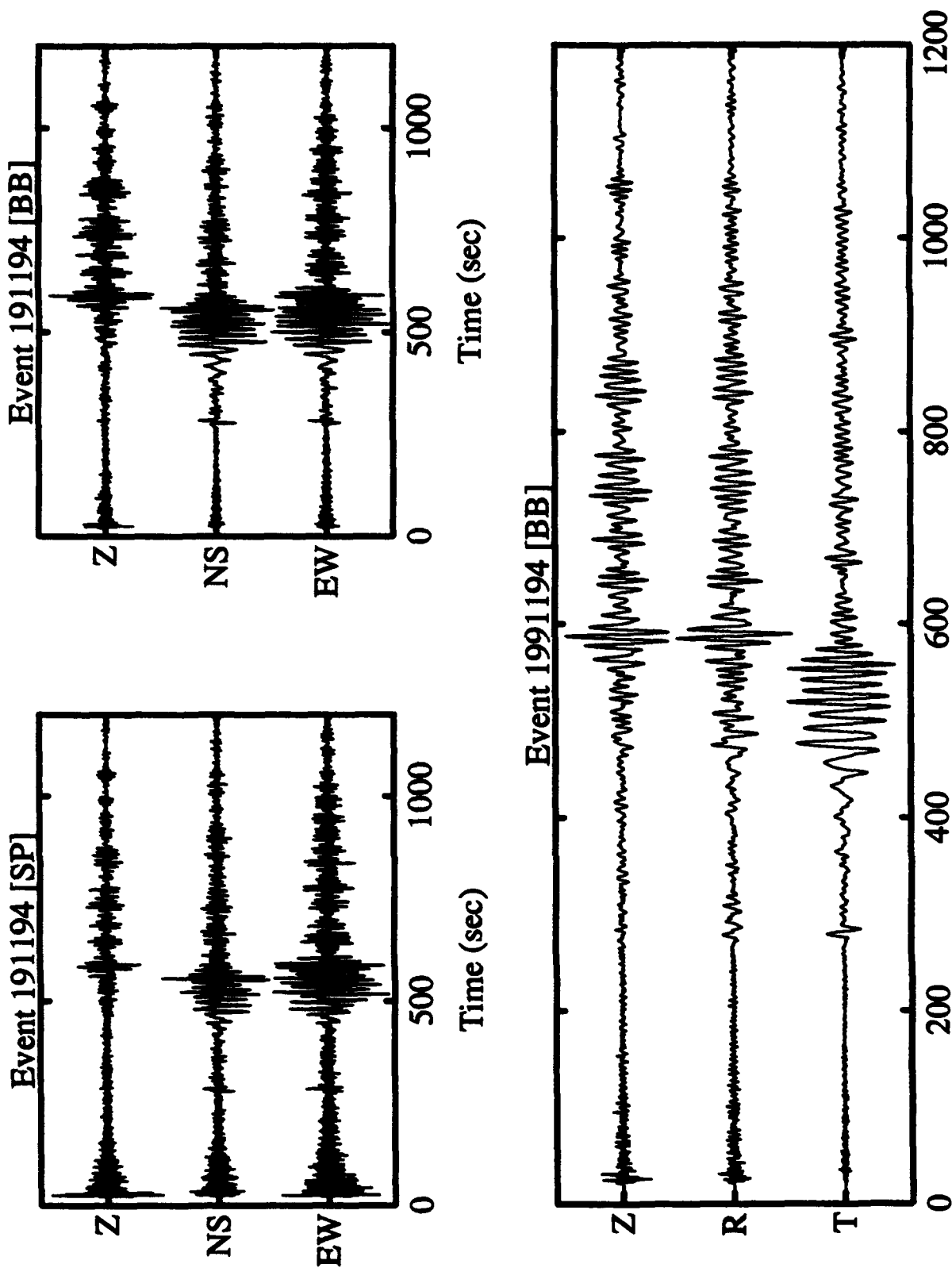
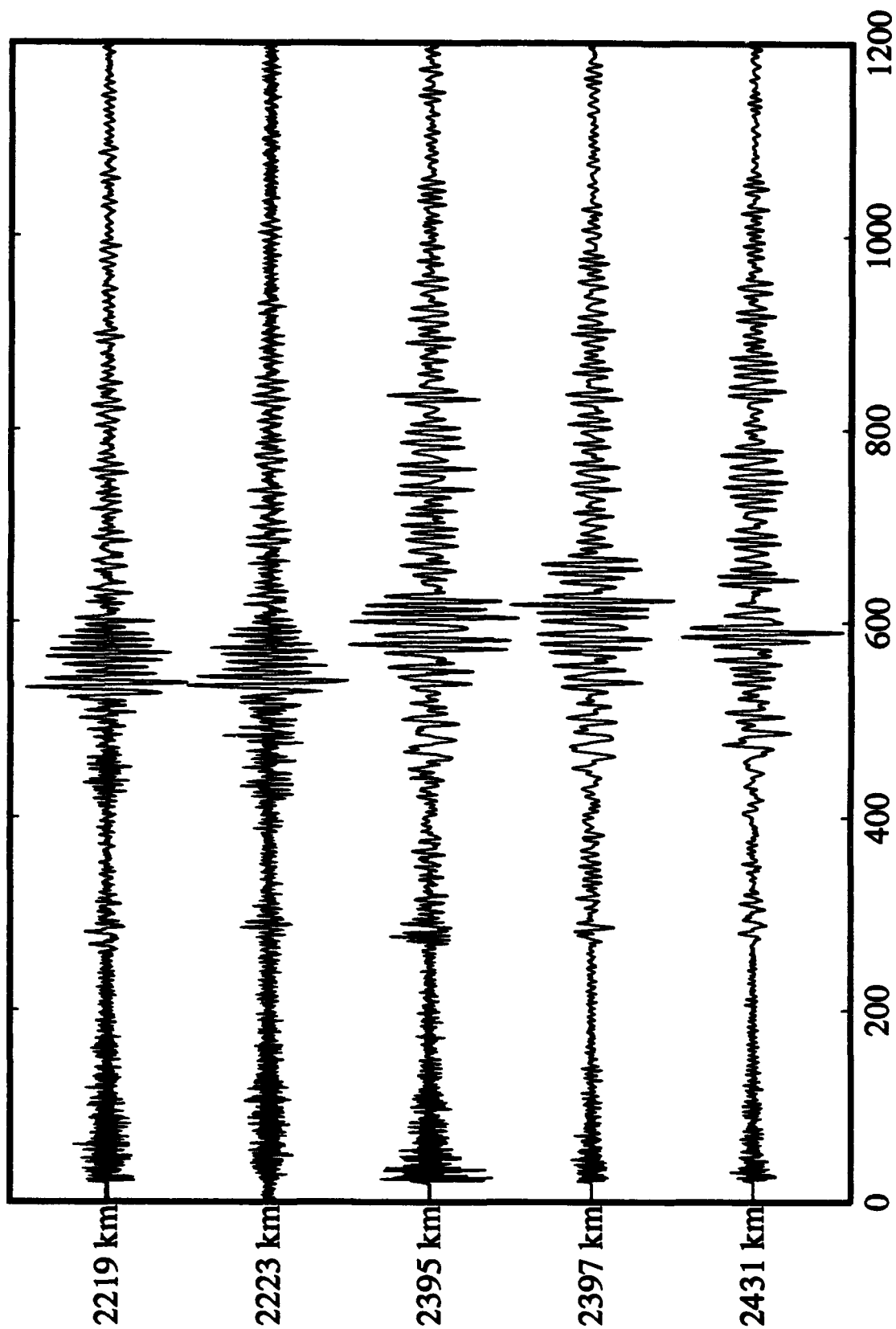


Figure 3

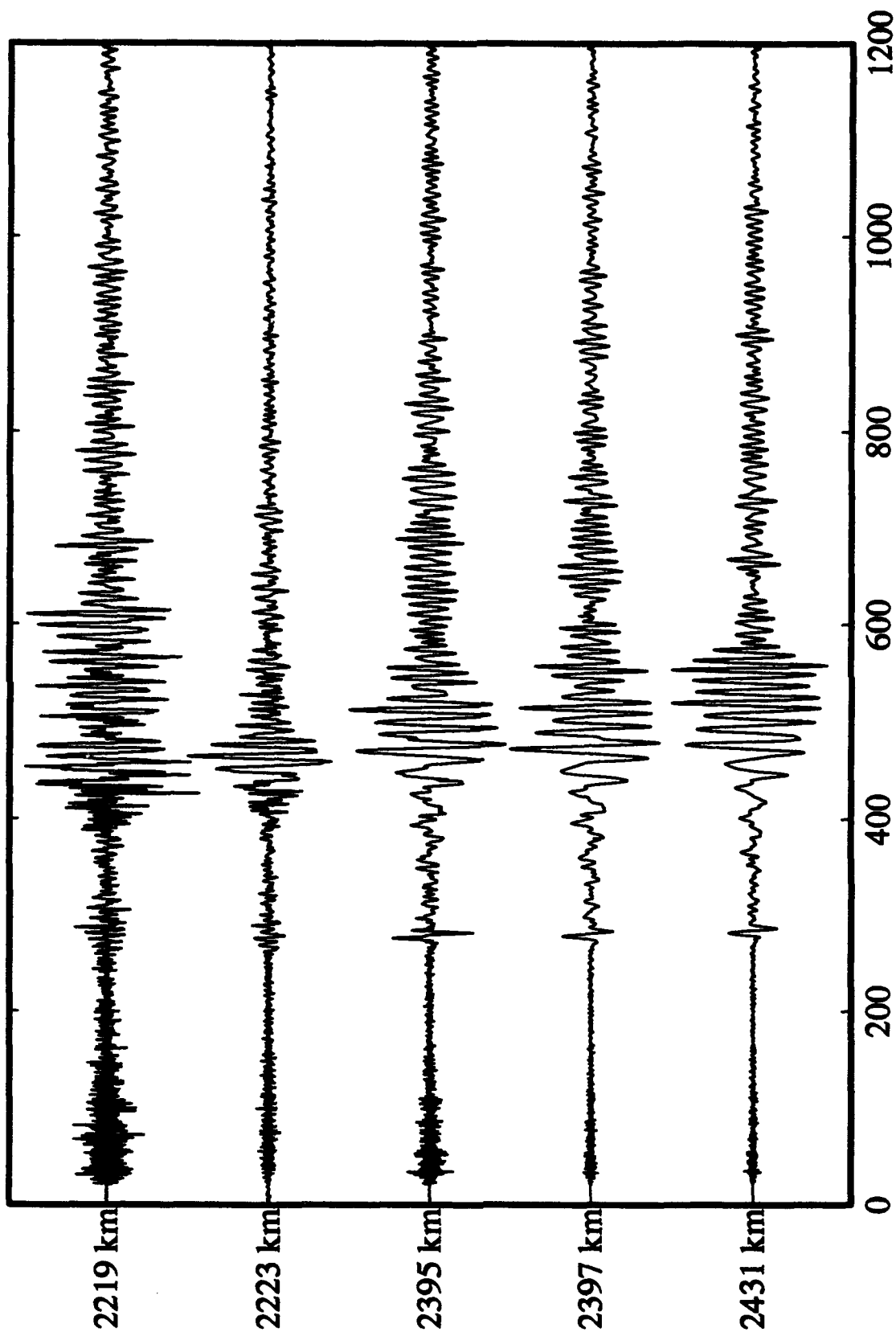
Radial Seismograms; Distance > 2000 km [BB]



Time (sec)

Figure 4a

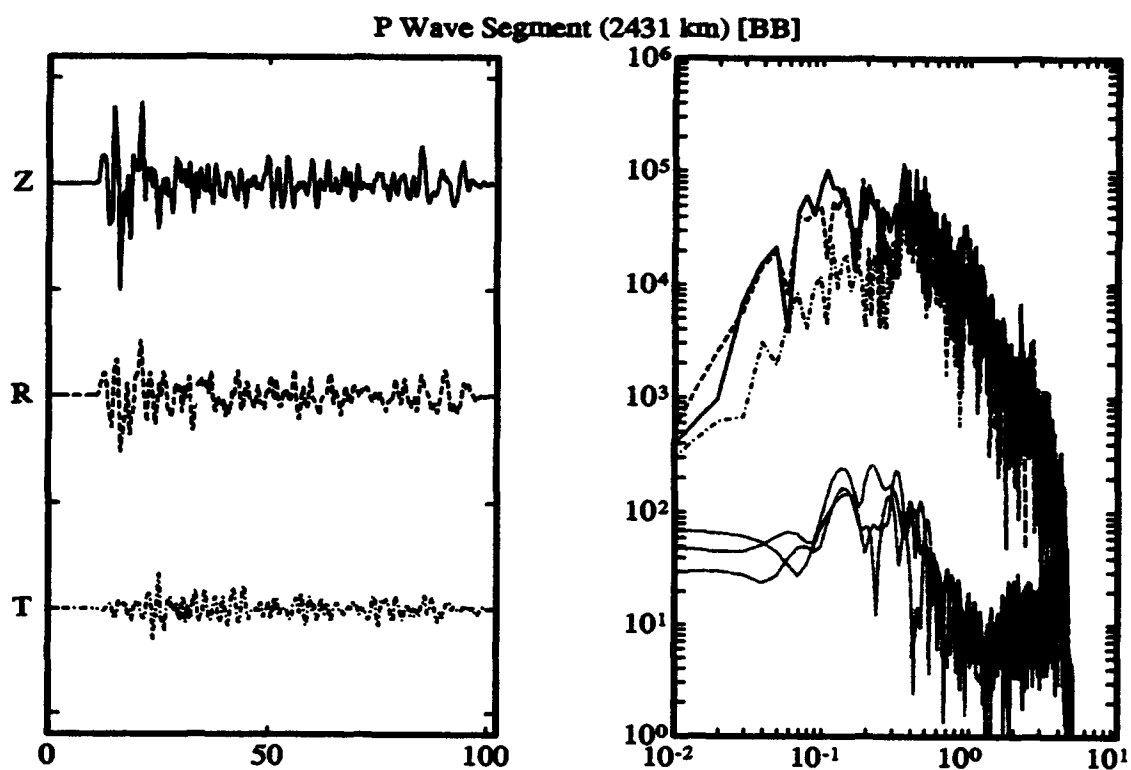
Transverse Seismograms; Distance > 2000 km [BB]



Time (sec)

Figure 4b

a)



b)

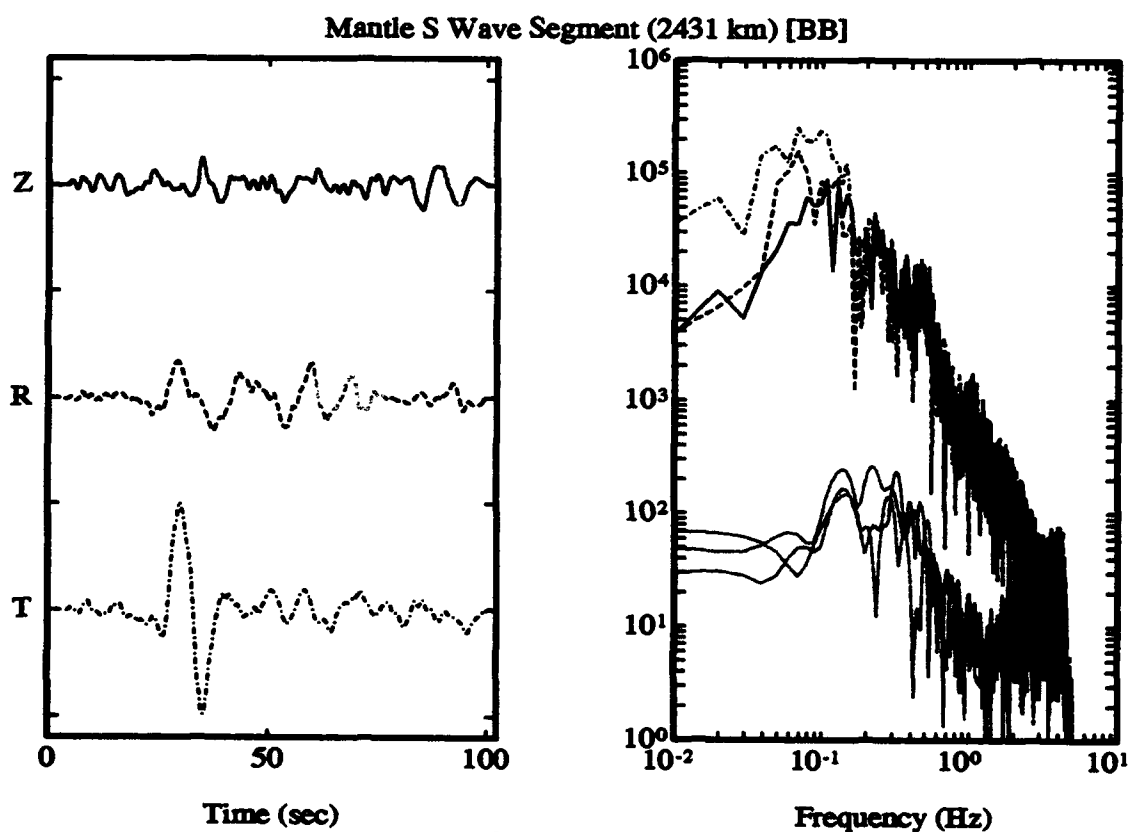


Figure 5

Moment Tensor Solutions

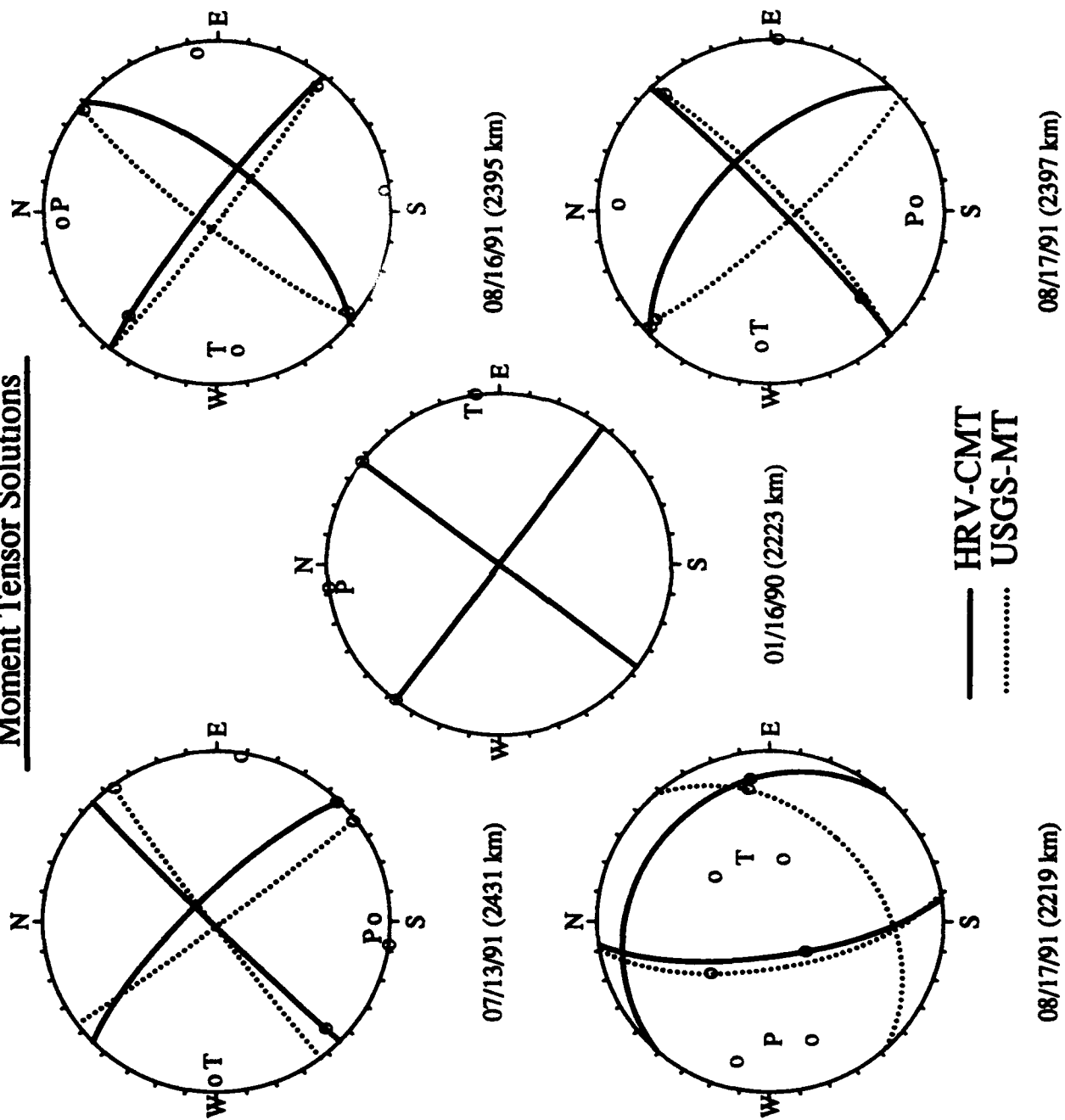


Figure 6

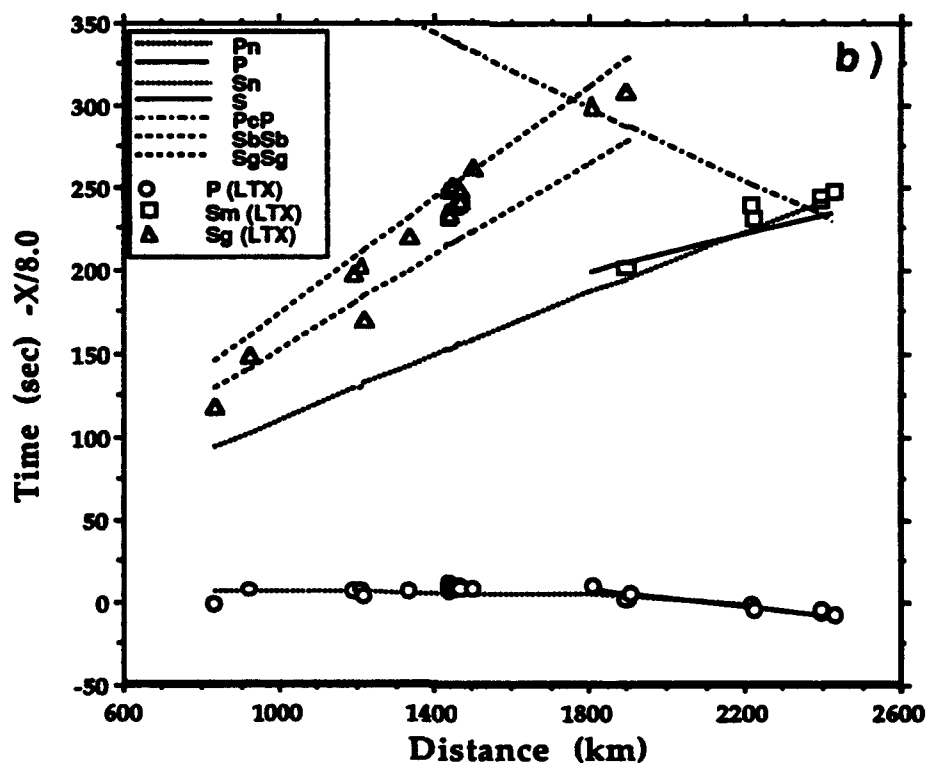
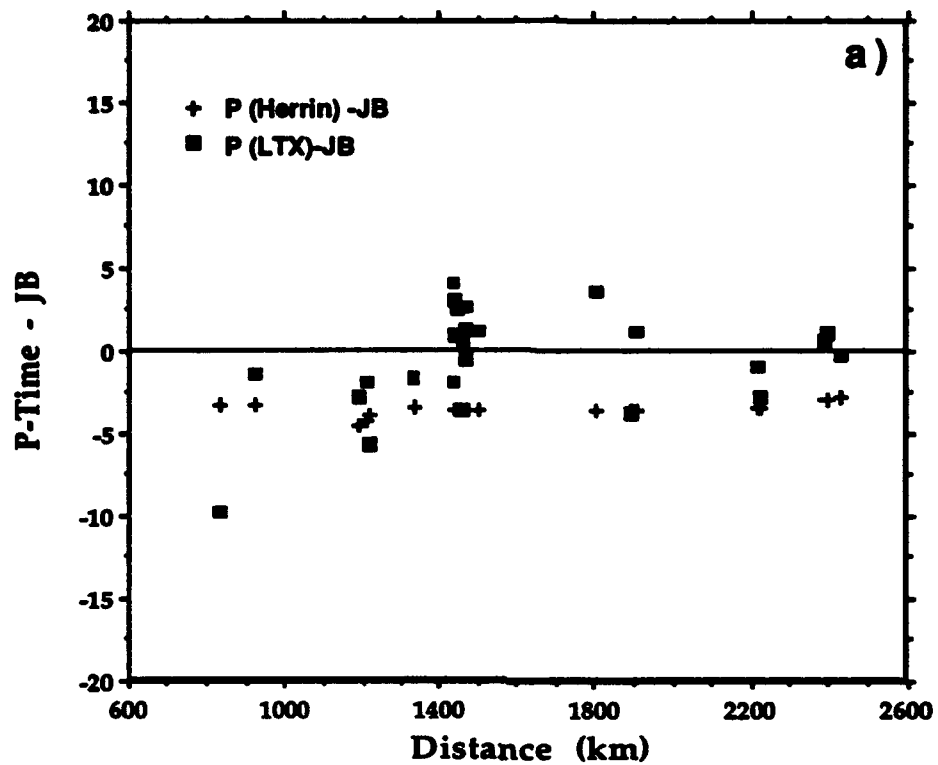
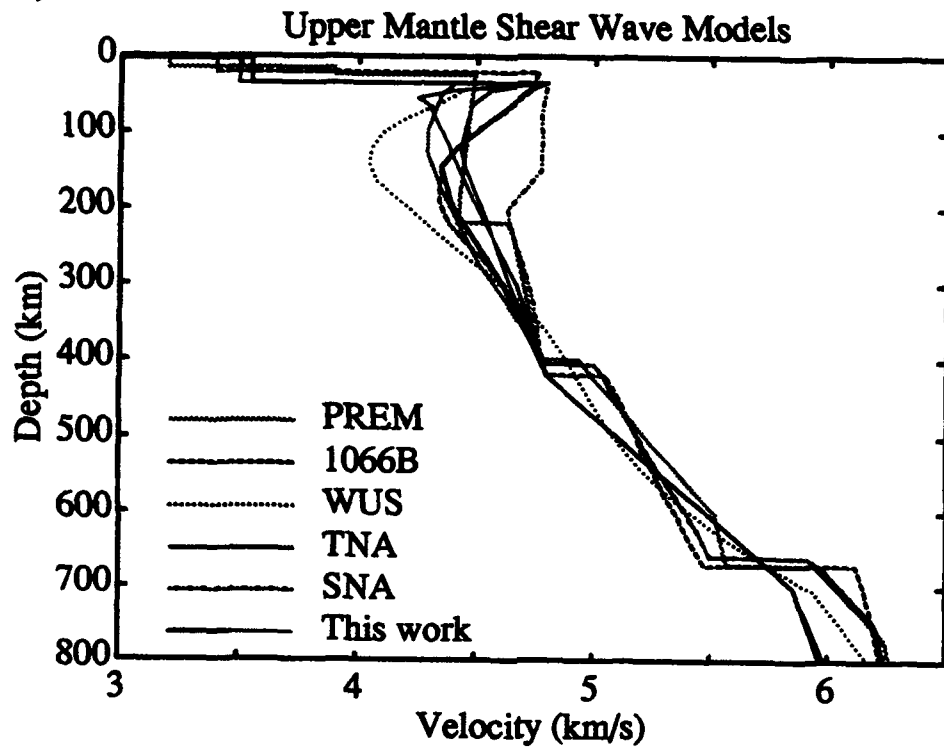


Figure 7

a)



b)

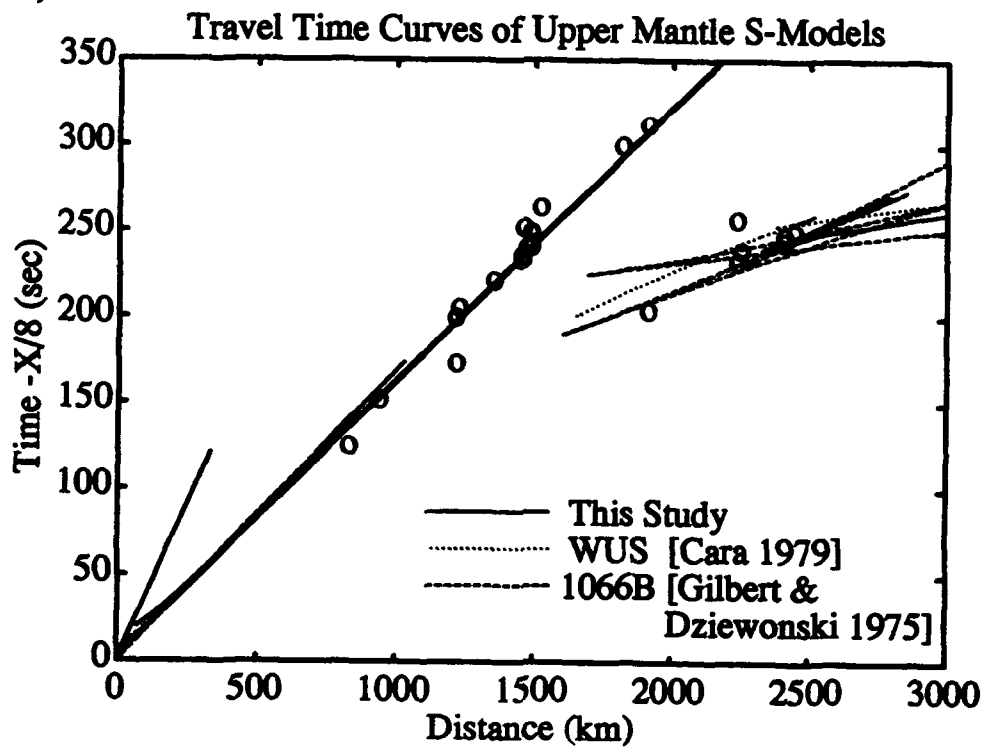
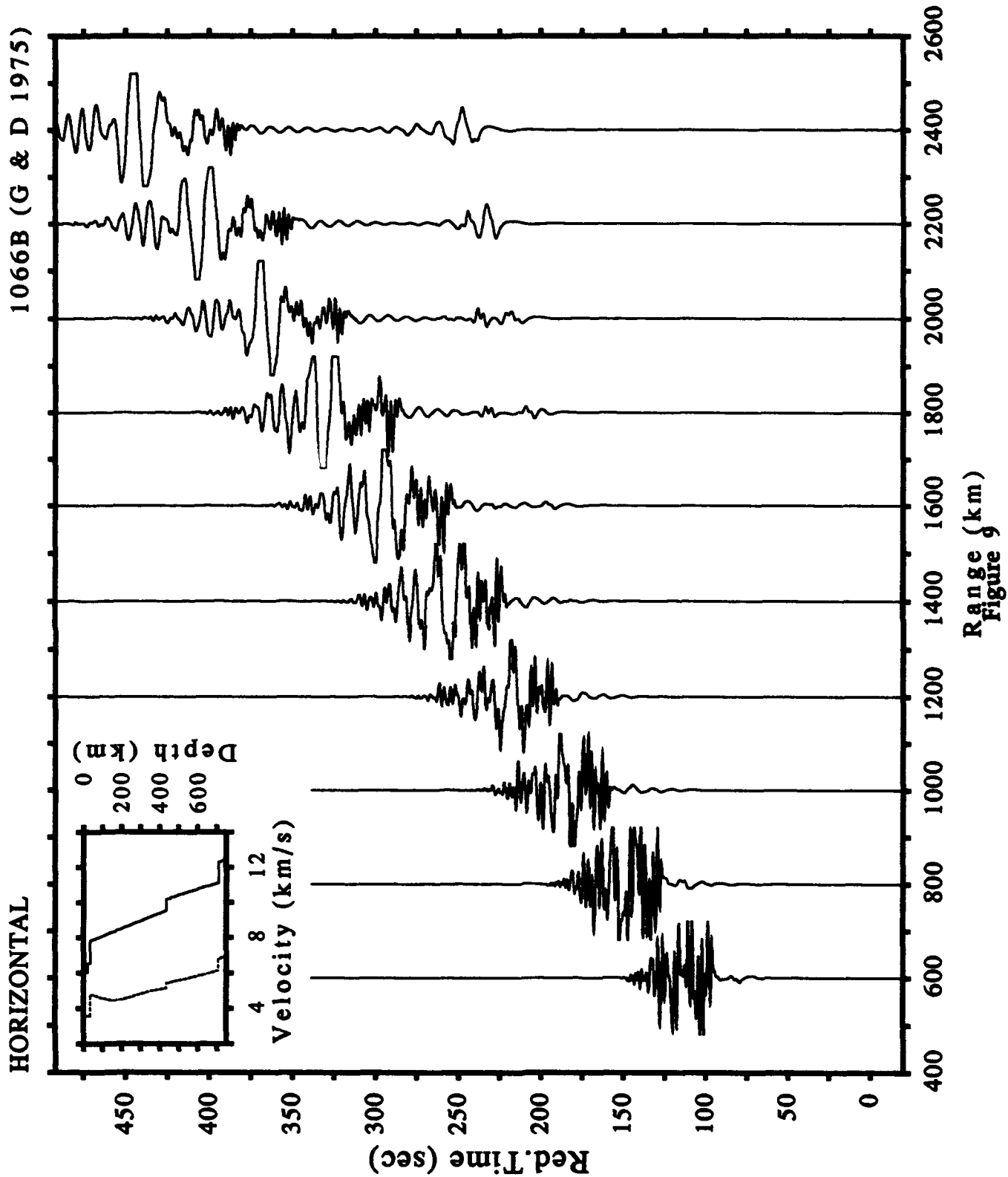
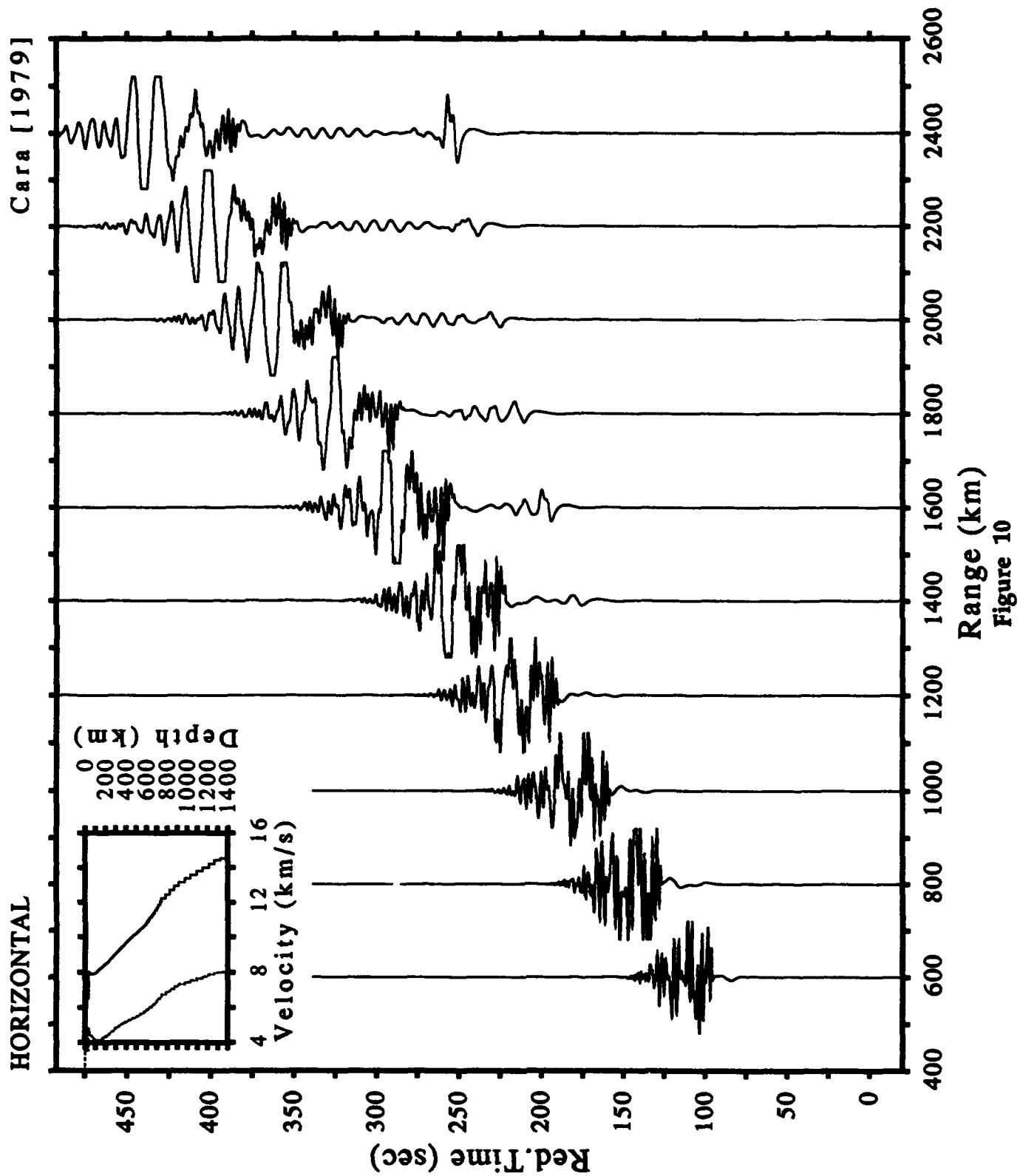
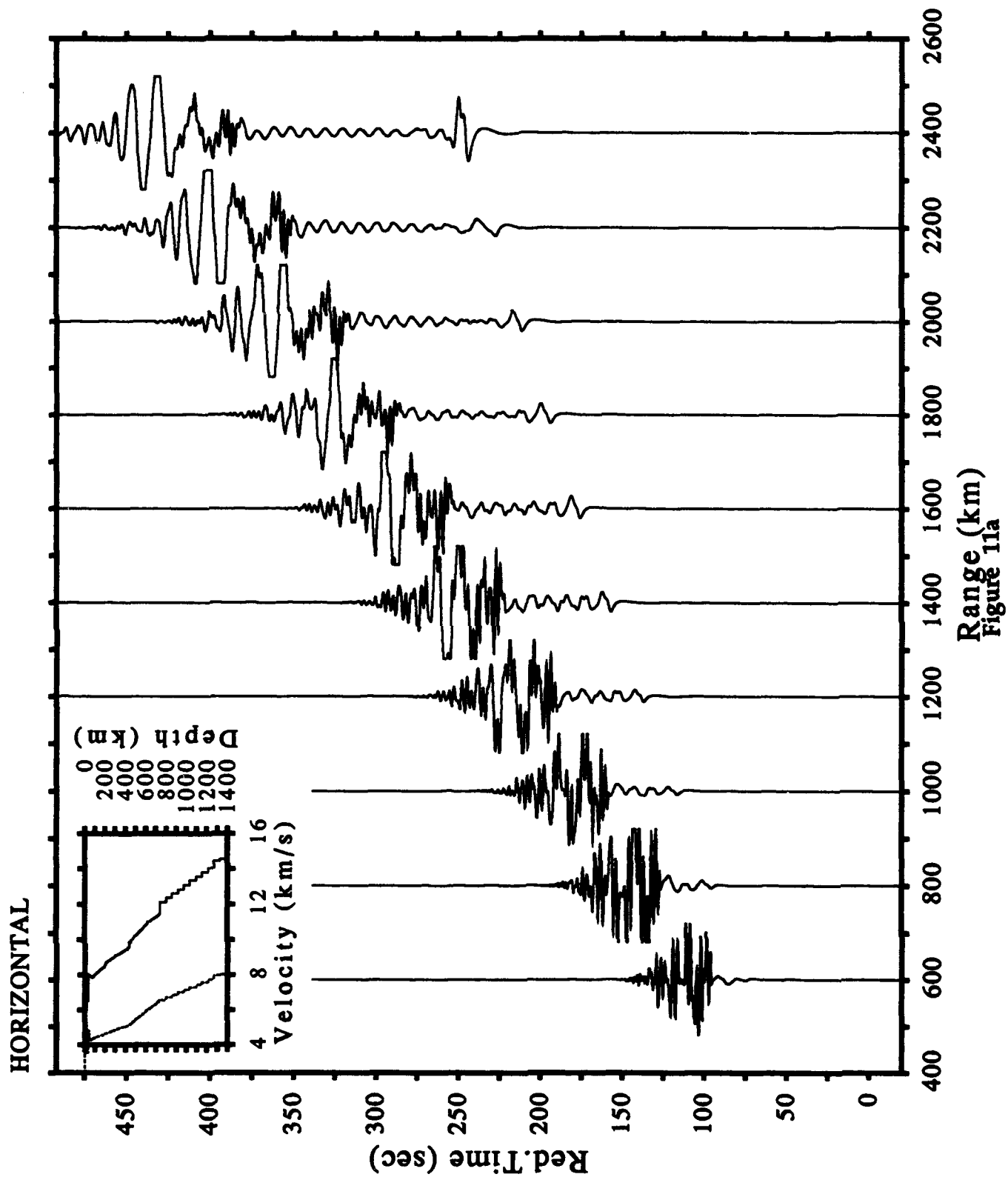


Figure 8







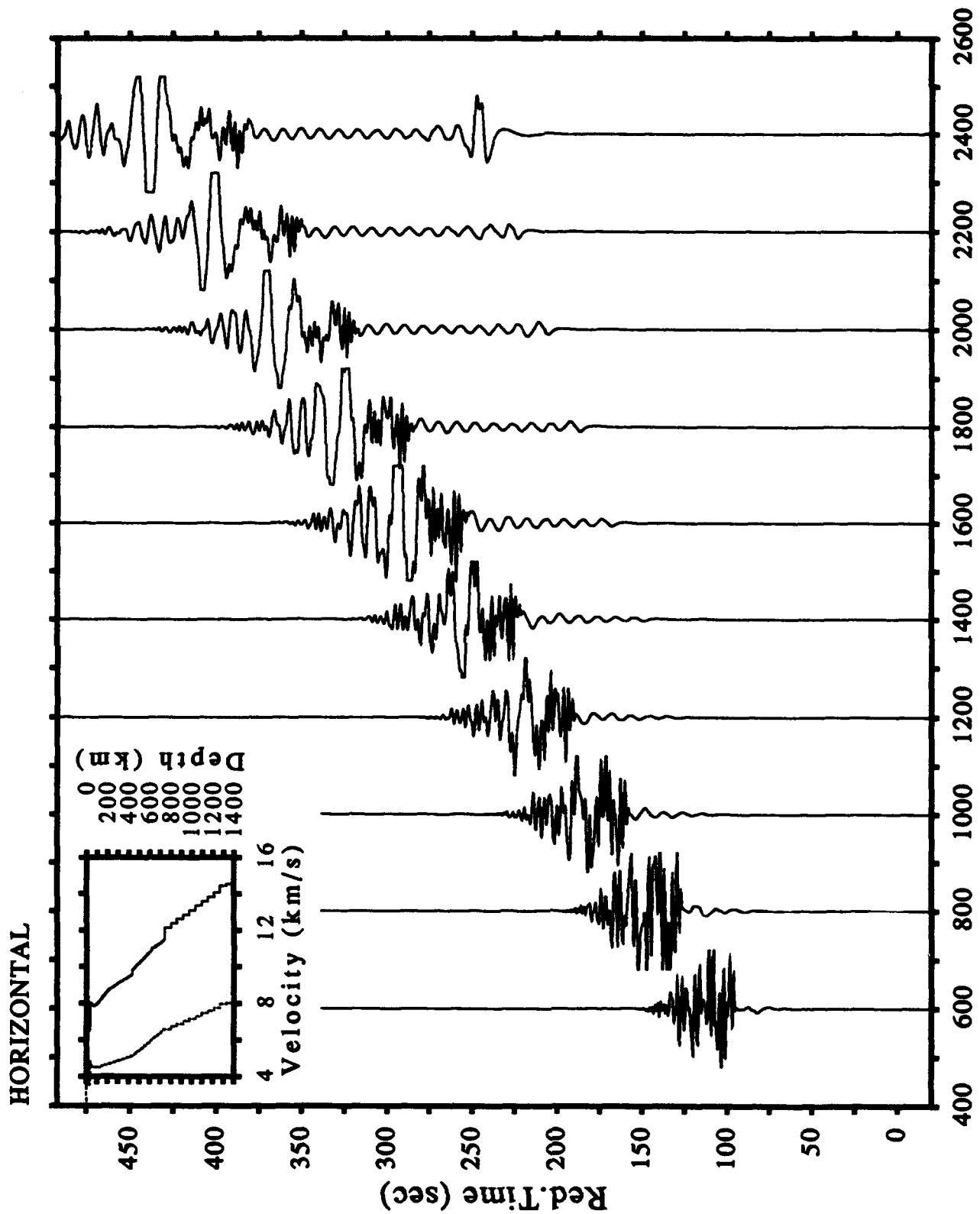


Figure 11b

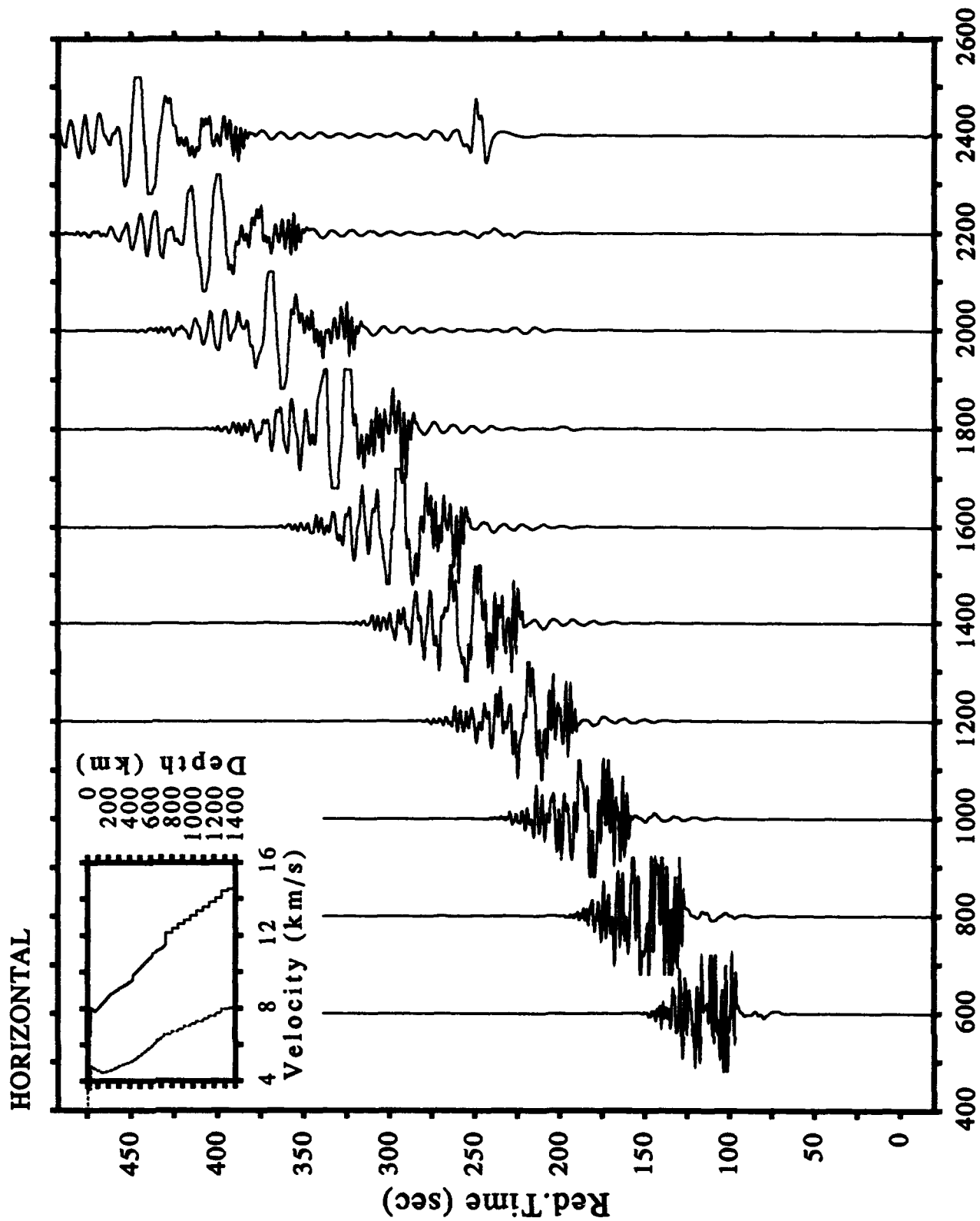
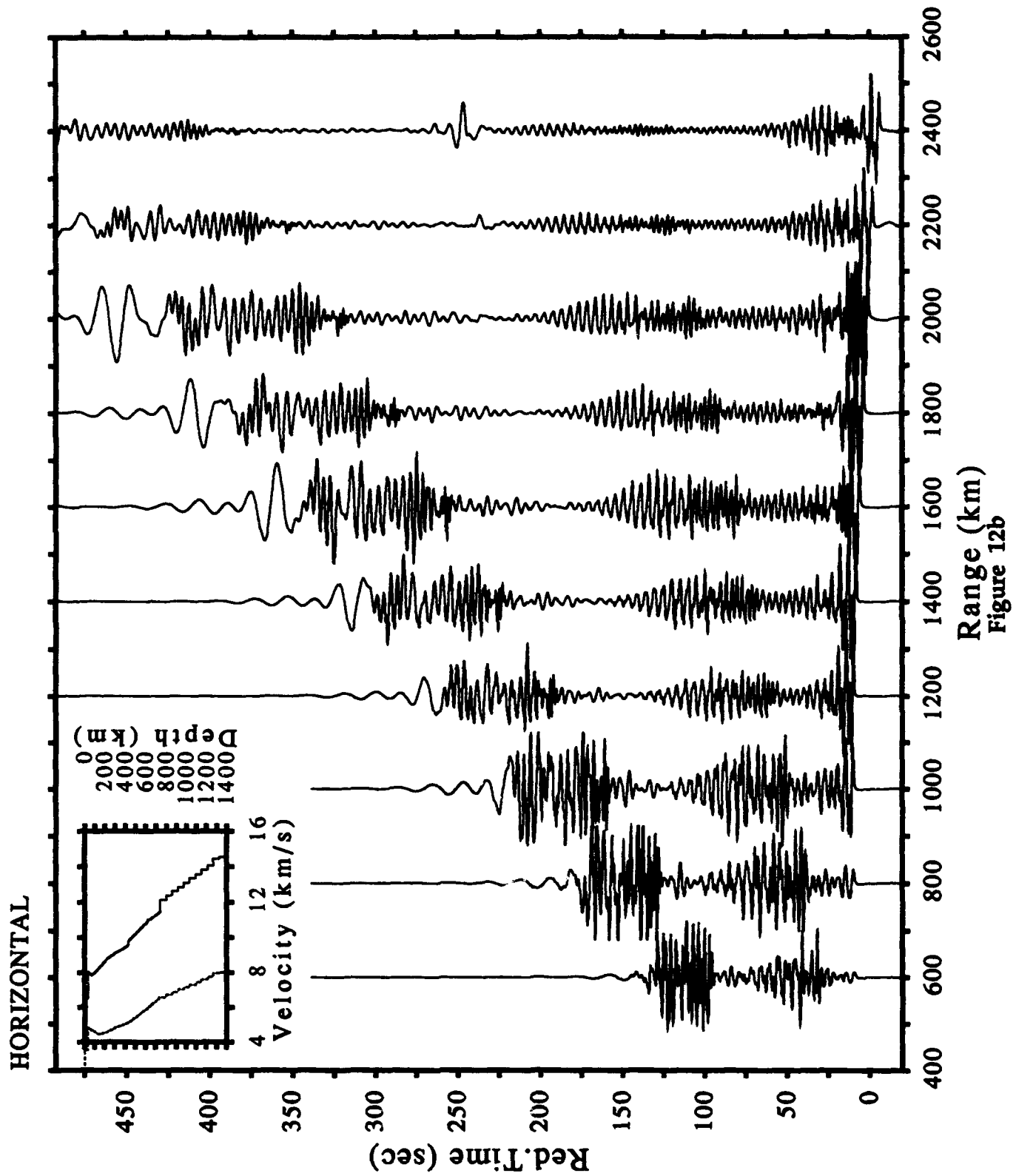


Figure 12a



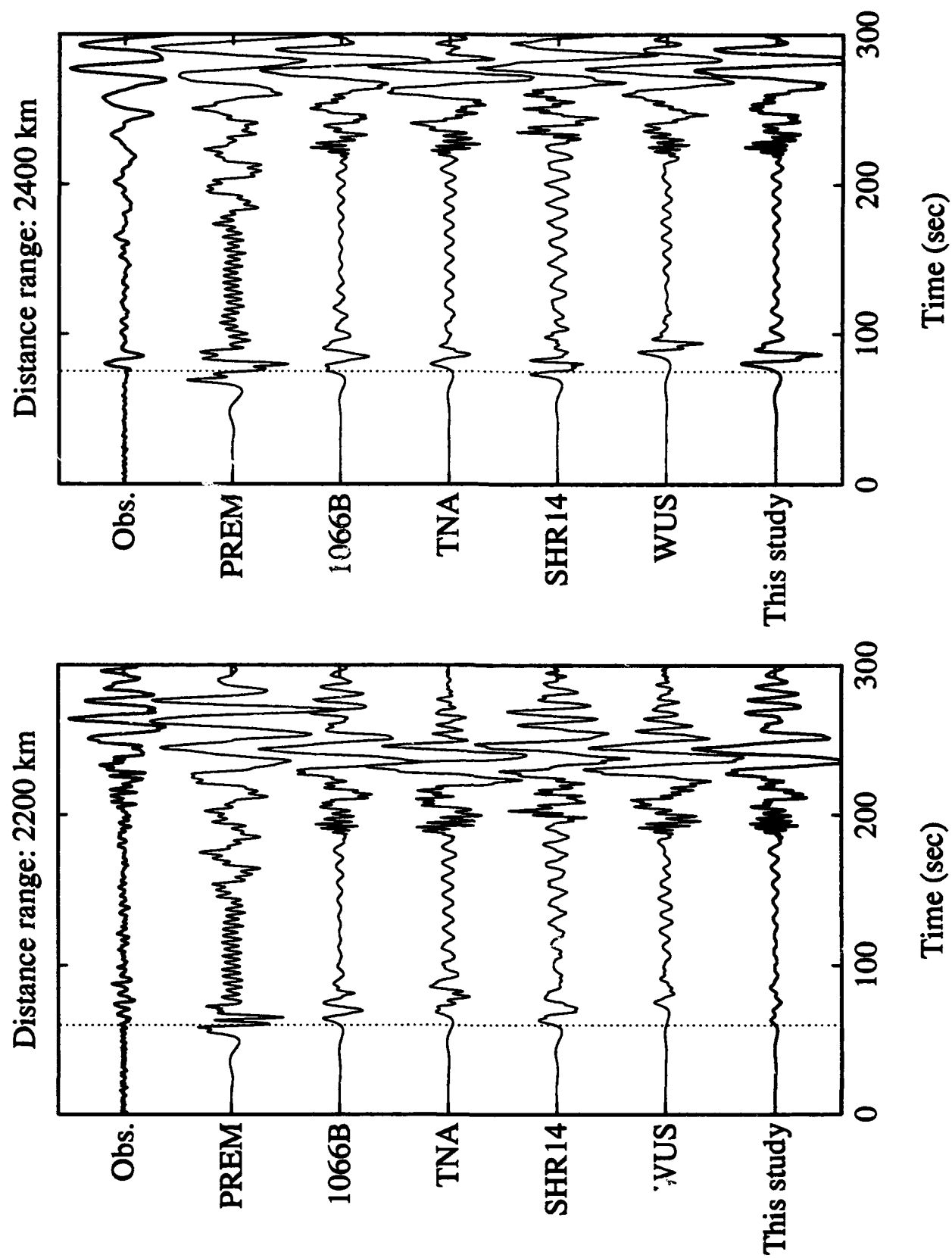


Figure 13

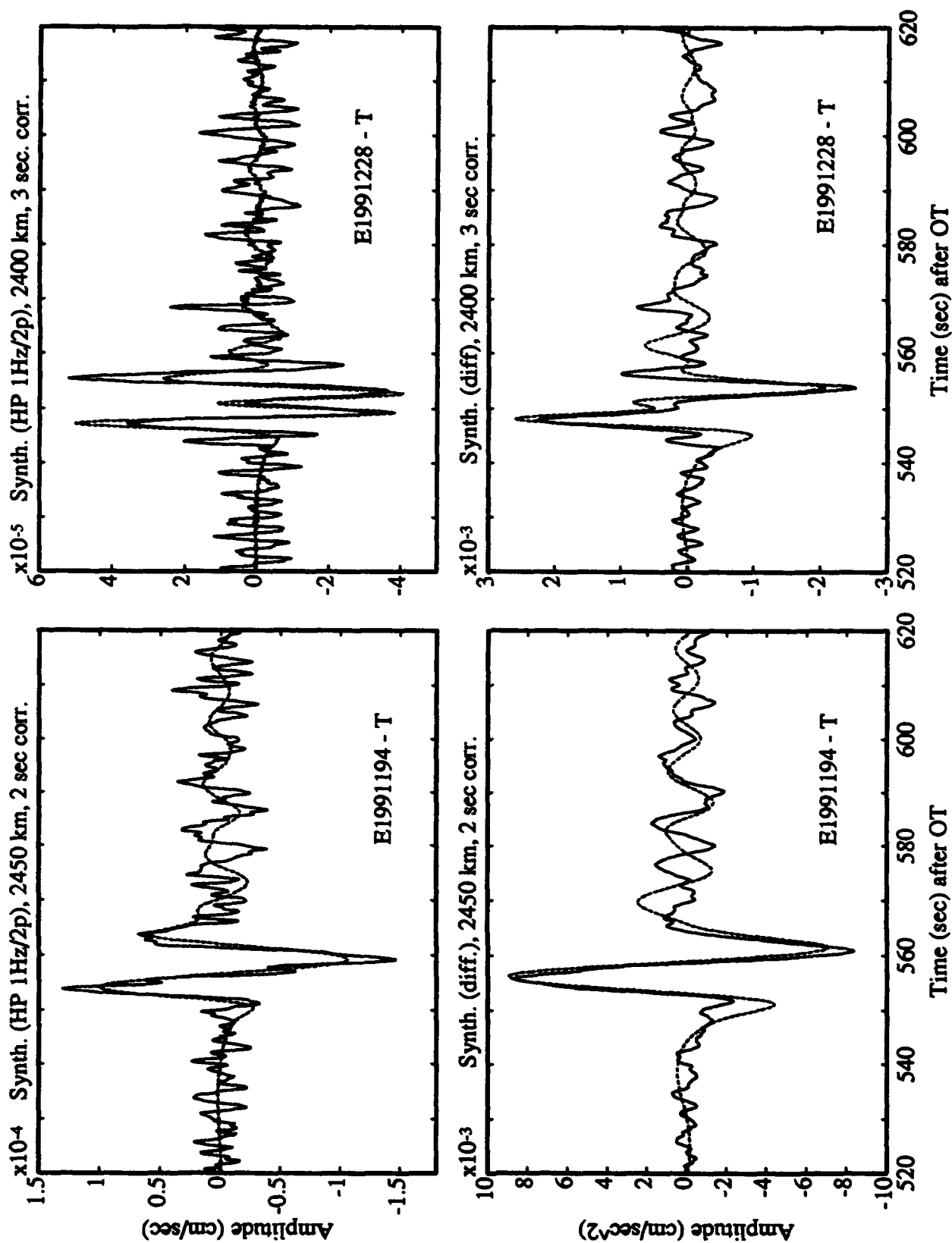


Figure 14

CONSTRAINTS FOR UPPER MANTLE SHEAR WAVE MODELS OF THE BASIN AND RANGE FROM SURFACE WAVE INVERSION

K. Koch & B.W. Stump
Department of Geological Sciences
Southern Methodist University
Dallas, Texas 75275

Abstract

Earthquakes on the coast of Northern California and off the coast of Oregon have provided a set of broad-band regional seismograms at Lajitas (LTX). These waveforms display significant Love and Rayleigh waves. Previous studies (using a subset of these sources) of mantle S waves suggest a smoothly varying S velocity structure above 400 km followed by a strong gradient between 400 km and 700 km. Surface wave inversions are performed in order to further constrain the upper mantle S model using group and phase velocity dispersion for periods between 10 and 100 sec. This period range gives good resolution for sub-Moho depths extending into the low velocity zone. Group velocities are extracted by multiple filter analysis and show significant differences for events on- and off-shore at periods around 50 sec, which can be shown to be an interference pattern with the mantle S body wave arrivals. As single station data were used, phase velocities are estimated by phase-matched filtering. The recovered surface wave dispersion data are used in an inversion procedure to recover shear wave structure and indicate a relatively thin mantle lid underlain by a low velocity channel probably extending to a depth of 200 km. Deeper structure is poorly resolved and trades-off with subtle changes in the shallower structure. However, the Rayleigh wave group velocity data favor models with a region of higher shear velocities within the low-velocity zone. Shear models from body waves require higher velocities below the Moho to match the observed travel times than are given by the surface wave inversion. The differences between the mantle S model and the inverted surface wave model may be attributed to lateral variation between the Basin and Range and the coast range provinces. The mantle S waves propagate through a different upper mantle above 300 km than is sampled by surface waves whose path is almost entirely in the Basin and Range.

1. Introduction

In two previous papers (Koch & Stump, 1993; Koch, 1993) we studied far-regional seismograms across the Basin and Range from data recorded at the Lajitas station (LTX) in Texas. The initial work (Koch & Stump, 1993) provided strong constraints for the upper mantle structure using P waves; however, the mantle S structure was poorly constrained primarily due to the lack of S wave observations at distances less than 1800 km. A follow-up study produced clearly observed, impulsive mantle S-waves (Koch, 1993) at larger distances (> 2100 km) and placed strong constraints on the upper mantle shear velocity distribution in the Western United States in the 400-700 km depth range. However, as before, these observations left some ambiguity in the structure of the shallower upper mantle, especially for the sub-Moho region, associated with the lithosphere and underlying low velocity region, referred to as the asthenosphere. A complemented data set from the shear wave study was used here to resolve the shallow upper mantle S velocities to depths of about 200 km using fundamental mode surface waves. This data set is distinguished from other such studies by the fact that dispersion curves are measured manifold for exactly the same path yielding very stable dispersion estimates.

Surface wave inversions have been extensively used for constraining the upper mantle shear structure in the Western United States. In a recent paper, Al-Khatib & Mitchell (1991) report the inversion of Rayleigh waves in the period range from 10-100 seconds for upper mantle anelasticity and shear wave structure for different regions of the Western United States - the Eastern Rocky Mountains, the Intermountain, and the Western Margin regions. While the first region is not relevant for the current investigation, the latter two cover the area of this study. They find in the shear velocities of these regions a well developed mantle lid and low-velocity region to depths of about 150 and 200 km, respectively. For the Western Margin model they also identify a high-velocity region around 80 km depth, which was earlier noted by Koizumi et al. (1973).

Priestley & Brune (1978) in contrast have found a homogeneous low velocity layer for the Basin and Range in Nevada and Western Utah between about 70 and 200 km, with a fairly abrupt discontinuity at 200 km. Their dispersion data spans the same period range as that by Al-Khatib & Mitchell (1991). They used the two-station method for the bulk of their analysis although the one-station method was applied

to local events and explosions at the Nevada test site. Their data indicate that a source phase term of $\pi/2$ is appropriate for the explosion data.

In this study we will apply different techniques to retrieve dispersion parameters from the surface wave observations. This approach is designed to minimize the possible bias introduced by the single station method. Multiple filter analysis (Dziewonski et al., 1969), which was extensively used in surface wave analysis (e.g. Bache et al., 1978; Stevens, 1986; Russell et al., 1988) will provide an initial group velocity estimate. Phase velocity information will be retrieved through application of a phase-matched filter (PMF) (Herrin & Goforth, 1977) following the work of several researchers (e.g. Goforth & Herrin, 1977; Jin & Herrin, 1980; Stevens, 1986; Russell et al., 1988; Al-Khatib & Mitchell, 1991). Both Love and Rayleigh wave dispersion curves were used in the surface wave inversion scheme. Inversions were performed on single event data as well as on dispersion curves averaged over all events. This approach was pursued in order to estimate the significance of differences in the velocity model solutions which may be due to data bias such as caused by source phase terms or initial velocity model constraints. The results will be compared to previous results from surface wave inversion along with a discussion of the shallower structure found in light of the previous work which emphasized the body wave contributions to the far-regional seismograms.

2. Data and Dispersion Analysis

Data at LTX are recorded with three component short period instruments (S-13) and three component broad-band instruments (BB-13). For the current study we primarily used data from the latter instrument, recorded broad-band in acceleration between about 300 sec and 5 Hz, from earthquakes on the coast of Northern California and off the coast of Oregon. For some of these events, whose source parameters are given in Table 1, some components of the broad-band instruments were either not recorded or had data glitches. For these events we used the short-period data and produced simulated broad-band data according to the procedures developed by Seidl (1980), while carefully checking the appropriateness of the procedure by comparing simulated and original broad-band data segments where available (see Figure 1). All Love wave data are shown in Figure 1a and the vertical component Rayleigh waves in Figure 1b. We do not show the radial component data, as they contain the same information (in terms of dispersion data) as the

vertical data, and, as will be discussed later, the results derived from radial components appeared unreliable due to multipathing and/or poor signal to noise ratios. The data shown were decimated to a sampling rate of 1.2 sec from an original sampling period of 0.1 sec and are arranged in chronological order. All the events are relatively shallow events with focal depths of less than 15 km according to the data given in Table 1, although some of the events favour shallower locations as demonstrated by waveform matching (Koch, 1993).

The data were first analyzed with a multiple filtering analysis technique (MFT) (Dziewonski et al., 1969; Herrmann, 1988). Results for one event are shown in Figure 2, which displays the original seismogram with linear time sampling to the far right and the same data in reciprocal time sampling (or equivalently linear group velocity) to the left. The group velocity dispersion curve (far left) is displayed with contour lines of the amplitude distribution in the group velocity-frequency domain. The dispersion curve is relatively smooth throughout the frequency range from 0.01 to 0.1 Hz (10 to 100 sec period, respectively). Above 0.1 Hz the data show amplitudes throughout the whole group velocity range due to interference of body wave coda. Spectral amplitudes for the fundamental mode group velocity curves show a signal to noise ratio of 10 or more for this mode in the useful period range ($T > 10$ sec).

The mantle S body wave arrival is manifested in the flat contour line (no dispersion) in Figure 2 near the group velocity 4.5 km/sec. This non-dispersive branch is very clear at periods below 10 sec, but there is some energy also observed between 20-30 sec. The observed local minimum of the dispersion curves for periods around 50-60 sec, similar to the pattern for an Airy phase, was suspected to be an interference phenomenon from the body wave arrival. A second dispersion analysis for the same event is shown in Figure 2b, where the surface wave train was windowed to eliminate the impulsive mantle S arrival. The local minimum has disappeared, identifying it as an artifact resulting from interference of the mantle S arrival with the surface wave train in the MFT procedure. As Dziewonski et al. (1969) pointed out, there is an influence between neighboring envelope points in the frequency-group velocity domain due to limited frequency and time resolution. While it was relatively easy to eliminate the localized mantle S energy in this case, we did not apply the windowing procedure to other events, as it proved difficult to choose a suitable window for the on-shore events, without truncating the longest period surface wave energy. A further reason for not trying to eliminate the body

wave arrivals was the fact, that we applied the PMF procedure with the expected benefit of rejecting the non-dispersed arrivals. Some further discussion is given below.

All Love wave dispersion curves from MFT for the events in Table 1 are shown in Figure 3. On-shore events are drawn with gray lines, while off-shore data are marked with solid lines. The Love wave group velocity dispersion is stable from event to event. The scatter of the data is of the order of 0.1 km/sec in the considered frequency band. As the events cluster near two locations, the interference of the group velocity curves with the mantle S arrivals in the MFT analysis is manifested by the crossing of the dispersion curves of either off-shore or on-shore events in one point, as a result of the difference in travel time for the body wave arrival.

The same analysis procedure was applied to vertical and radial component seismograms and the results from the MFT analysis for vertical records from two events are shown in Figure 4a-b. As the two events had rather different focal mechanisms, although at comparably shallow source depth, spectral holes due to the source type (Ben-Menahem & Harkrider, 1964; Harkrider, 1970) are seen at different frequencies. Outside the frequency band of these spectral holes, the dispersion data are consistent between the two figures. However, spectral amplitudes were only a factor 2-3 above the background noise for most data. The vertical component Rayleigh wave dispersion curves for all the events in Figure 5a show more scatter than found for the Love waves and is reflective of the lower signal to noise ratios. Dispersion curves appear to be useful between 70 and 10 sec. When trying to separate the data according to the source region or the source mechanism (both strike-slip and normal faulting events are used), a slightly smaller scatter appears to go along with normal faulting events, indicating stronger Rayleigh wave excitation for these events. While the vertical component data were useful for retrieving Rayleigh wave dispersion, radial component data gave inconsistent results, as is evidence by Figure 5b. It is suspected that multipathed Love-waves with relatively high signal/noise ratio are interfering with the Rayleigh waves on the radial component and therefore lead to a breakdown of this method.

The group velocity dispersion curves received from the MFT analysis can be used to refine the group velocity estimate as well as retrieve phase velocity information by phase-matched filtering (PMF) (e.g. Jin & Herrin, 1980; Stevens, 1986; Russell et al., 1988), see Appendix. The group delay as obtained from the group velocity dispersion

is used to estimate the phase spectrum by fitting it to the observed phase (Herrin & Goforth, 1977). This phase information is then used to obtain the phase velocity by

$$c(\omega) = \frac{-\omega R}{\Theta(\omega) - \Theta_0(\omega) - 2\pi N}$$

where R is distance, ω frequency and Θ and Θ_0 are observed phase and source phase, respectively. N is an integer number usually constrained so that the long period phase velocities match the values observed on a world-wide scale. For example, Stevens (1986) used this technique for estimating scalar moments from surface waves generated by nuclear explosions at the Nevada and East Kazakh test sites.

PMF filtering produces consistent results for the Love waves, as might be expected from the MFT analysis (Figures 6). Group velocities between 10-100 sec have scatter of less than 0.1 km/sec, with somewhat larger scatter for phase velocities at the longest periods (up to 0.2 km/sec). The PMF seismograms displayed in Figure 6b can be compared to the original records in Figure 1a. The waveshapes as well as the maximum amplitudes, given to the right of each trace, demonstrate the success of the PMF procedure and its capability of extracting the fundamental mode data. This point has been the subject of some controversy (Der et al, 1986; Stevens, 1986). Rayleigh waves from the vertical component data produce larger scatter, anticipated from the smaller signal/noise ratio, although both group and phase-velocity scatter does not exceed 0.2 km/sec. The larger scatter in the vertical dispersion curves at frequencies near the spectral holes is considerably reduced in the PMF results. The larger overall scatter is suspected to be the reason for the stronger event to event variations of the PMF seismograms plotted in Figure 7b. However, comparison with Figure 1b argues that the fundamental mode Rayleigh wave is nevertheless successfully extracted.

3. Surface Wave Inversion

The surface wave dispersion curves were combined in different ways to estimate the significance of a particular data set and its associated inversion model. One set of data contained only the dispersion curves from the event (July 13, 1991, see Table 1) with the best signal to noise ratio. Other data sets contained average dispersion

curves of either Love and Rayleigh dispersion. A third data set combined all available data, i.e. Rayleigh and Love wave data. These different inversions were performed to identify consistency in the resulting velocity models. Love wave dispersion is only dependent on the S- wave structure while Rayleigh wave dispersion is dependent on both P and S wave velocity structure (often the approach is taken to either constrain the Poisson's ratio or to assume a constant P wave velocity structure as the dependency on this parameter is weak (e.g. Bache et al., 1978)). The P wave velocity model was constrained based on previous body wave studies along the same propagation path (Koch & Stump, 1993). The use of a particular single event for the inversion was designed to see, whether source phase terms, that might be canceled out in the averaged dispersion curves can significantly bias the velocity models. The inversion procedure (Herrmann, 1988) is an iterative, non-linear damped least square method, and was previously used by e.g. Al-Khatib & Mitchell (1991). With the previous upper mantle work (Koch & Stump, 1993; Koch, 1993) we used the stochastic inversion method as the starting model was assumed to be reasonably well constrained, and to obtain improved resolution as a deterministic model will be smoother due to the inherent constraints between adjacent layers. However, the stability of the solution in this case appears to depend more critically on an optimal damping parameter. This topic was addressed by both using different starting models and an excessive number of iterations.

All inversion results will be summarized by displaying the starting model (S- wave structure), the model obtained from the inversion, and the model of Priestley & Brune (1978). As starting models the range of models suggested by Koch (1993) was considered which were equally well suited for the depth range above 300 km in modelling the mantle S body wave arrivals shown in Figure 1. These models from previous studies are displayed in Figure 8 and the dispersion curves predicted by them are shown in Figure 9. In both figures the crosses indicate the results from Priestley & Brune's model, while the closed symbols are from the work of Koch (1993). The Love wave dispersion at shorter periods tends to follow more closely the dispersion curves calculated from the models introduced by Koch (1993), in particular the model with the triangular symbols, for both group and phase velocities. For the longest periods (>50-60 sec), the dispersion appears to be better modelled by the predictions from Priestley & Brune's model. For the Rayleigh waves the fit is more ambiguous as the measured group and phase velocities scatter between the predicted dispersion from the previous models, but with a slight

indication that Priestley & Brune's model might be superior for the longest periods and hence for the greatest significant depths in the upper mantle models.

Single Event Love Wave Data

The Love wave seismogram with the best signal/noise ratio was obtained for the event of July 13, 1991 off the coast of Oregon (see also Figures 1, 2, 6, Table 1). This event had a magnitude $M_s=6.9$ and provided the cleanest dispersion results, although some later events had larger published surface wave magnitudes. The inversion result for this data set is shown in Figure 10. On the left side of the figure, the thin solid line marks the starting model used in the non-linear inversion procedure, the bold solid line is the result of the inversion with the crossbars indicating the error estimate, and the dotted line displays the model (USWESPB) of Priestley & Brune (1978). On the right side, the normalized resolution kernels are reproduced for selected layers at depth (indicated by the number at each curve). The dashed line gives the zero line for reference. The velocity model recovered from the inversion shows a fairly consistent and expected picture for the crustal structure (velocities around 3.5 km/sec), while the mantle lid shows significant change from the starting model as well as the reference model by Priestley & Brune (1978). For depths larger than about 60 or 70 km, the model shows more similarity with USWESPB than with the starting model, and almost no difference for depths larger than 200-250 km, which is due to the lack of resolution at these depths. This is also indicated by the resolving kernels, which peak at the depth of the corresponding layers for depths less than 200 km, while at larger depths, the maximum is at considerably shallower depth. Significant trade-offs between layers as indicated by positive and negative values at various depths are obtained. In addition, the absolute magnitude of these deeper kernels are very small.

Average Love Wave Data

The average Love wave dispersion data produce a velocity model which is consistent with the single event data (Figure 11), although minor differences do exist. As in the previous case, a very thin high-velocity lid is recovered. The size and magnitude of the low-velocity layer is also comparable to the single event analysis. This inversion suggests more obviously a possible secondary low-velocity region below 120 km. The resolving kernels in this case are quite similar to the previous results from the single event data, also showing double peaks for layers between 30-50 km depth indication a possible trade-off between individual layers. The similarity

between the inversions of single event and averaged Love wave data strongly argues for only minor bias of the results due to source phase terms.

Average Rayleigh Wave Data

As discussed earlier, the signal to noise ratio on the seismograms containing the Rayleigh waves is reduced. The Rayleigh wave inversions are also dependent on the P wave model and a different source phase term. Thus, the possibility exists for a systematic error to be introduced if the adopted assumptions are invalid. However, as is evidence from Figure 12a, the model from inversion of the Rayleigh wave dispersion is consistent with the results obtained earlier (Figure 10, 11). The model contains both the thin mantle lid and the same extent of the low velocity layer, which in this case is even more prominently divided into two distinct low-velocity regions, the first at the base of the mantle lid and the second at depths between 120-150 km.

Due to the trade-off in the resolution kernels, in particular for greater depths, the applied damping parameter is critical. The solution in the underdamped case tends to increase the velocities in the depth region below 250 km unrealistically, while compensating these values by too small velocities at shallower depth. In order to assess the stability of the model, hence the appropriateness of the chosen damping parameter, the previous inversion (Figure 12a) is compared to an inversion with the number of iterations doubled (Figure 12b). Although there are minor differences, this new inversion indicates the solution to be stable. Hence, the chosen damping parameter must be considered optimal based on the small model differences.

Simultaneous Inversion of Love and Rayleigh Waves

As expected, the combined Rayleigh and Love wave inversions (Figure 13a) provide essentially the same velocity model as before. The thin mantle lid produced by this inversion is similar with one of the models (triangles) introduced in Figure 8, whose dispersion prediction favored the observations. Using this model as starting model (Figure 13b) produces only slight differences, with the prominent features in the model, such as the thin mantle lid and increased velocities within the low-velocity region, preserved. This starting model also contained an increased number of layers in the lower crust, designed to resolve a possible trade-off between the lower crust and the mantle-lid, and the implications will be discussed in the next section. These different inversions document that the model constructed from the

inversion procedure reflects the nature of the dispersion curves and is fairly independent on the initial conditions, data selection, or the errors within the data set.

4. Discussion and Conclusion

The inversion of surface wave data from a number of different data sets has resulted in a very consistent pattern for the shear wave structure of the Basin and Range province. The fit of the inversion model for the combined data set of Love and Rayleigh waves (Figure 13a) to the observed dispersion data is given in Figure 14 with a reasonable good fit to the data, using the given error bars as error estimates throughout the inversions (except for the inversion of the single event data, where only the residuals in the dispersion data were considered). Apparent jumps in the dispersion curves, often associated with strong changes in the standard error estimates of the data are related to the elimination of events with poor signal/noise ratios especially for the long periods. From the dispersion data, only the group velocity dispersion of the Rayleigh waves shows a poor fit between periods of 20 and 50 sec, where the inversion model (Figure 13a) predicts a much steeper increase in the group velocities at these periods.

An additional set of inversions were performed in which the measured dispersion was assumed to be better than given by the standard deviations. The inversion procedure in this case only considered the residuals of the dispersion curves. This assumption is justified by the fact, that three out of four curves were well matched even when including these errors. The resulting inversion model is shown in Figure 15 (left half) as the solid line, giving us a similar velocity model as before except for the more predominant high velocity ridge within the low velocity region. These higher velocities had also been found when inverting the Rayleigh wave data alone. The surface wave dispersion (Figure 15, right half) from this model is distinguished by giving a better match of the Rayleigh wave group velocity curve. Bloch et al. (1969) showed that group velocity dispersion is more sensitive to the model parameters, which can be directly correlated to our results, if we consider the improved fit of the Rayleigh wave group velocities as significant.

Motivated by the theoretical observation that a laminated lower crust is very efficient in generating the Lg wave for explosion sources, as argued for e.g. by

Campillo & Paul (1992) and Koch & Stump (1993), we used starting models that allowed for a finer structure in the lower crust (15 km thick, 3 layers). This model was further considered to investigate the possibility of trade-offs between crustal thickness and lid velocity. The starting model was the same as before, with higher velocities in the lower crust (3.8 km/s compared to 3.55 in the upper crust). Two inversions with and without the standard errors are also shown in Figure 15 which favor a kind of high-to-low velocity alternation in the lower crust. Whether this effect might also be influenced by a change in the Moho depth along the propagation path is difficult to assess. However, as there are quite high-velocities found below the Moho, and this mantle lid is present in all the previous inversions, it does not appear to be a trade-off effect, and hence not likely to be related to Moho topography.

Support for our conclusions concerning the shear wave velocity inversions is also found in the independent work of Al-Khatib & Mitchell (1991). They find a similar result for the Western Margin region shear velocity structure with indication of a high-velocity lid on top of the low-velocity layer. Based on the low velocities recovered, they argue about the possibility of a very thin lid, which has been suggested by Grand & Helmberger (1984) for the western United States. Their low-velocity zone is also marked by a high velocity ridge. Differences between Al-Khatib & Mitchell and our results include their Moho depth (assuming the high velocity lid represents the Moho) which is more than 10 km shallower than found in this study (35 km). The shallow Moho depth contradicts results from other geophysical investigations in the Basin and Range (e.g. Priestley & Brune, 1978; Benz et al., 1990), which argue for a depth to the Moho of 30 to 35 km. Al-Khatib & Mitchell's model for the Intermountain region, though giving a more consistent depth of the Moho, unfortunately suffers from the lack of longer period data as well as their large standard errors, so that the resolving power through the low-velocity region should be small.

The Basin and Range model of Priestley & Brune (1978) is included in Figures 11-15 for reference. Most inversions suggest, that the new model is compatible with their model throughout the upper mantle, except for minor differences in the low-velocity layer. Priestley & Brune incorporated a fairly thick upper mantle lid on the order of 30 km, where the new model suggests a very thin mantle lid. In order to investigate the effect of model parameterization on this characteristic, the fairly fine layering in the lid region was replaced with a single thick layer. The inversion with this parameterization produces a velocity model, which is almost identical with that

proposed by Priestley & Brune (1978) except for decreased velocity (0.1-0.3km/sec), indicating that the difference can be attributed to this discretization. However, when comparing the residuals between the two models, the differences appear to be not significant to apply a statistical test.

Priestley et al. (1980) considered the effect of lid thickness on fundamental and higher mode surface waves in the Great Basin. They argue for a lid thickness of 29 km and against a thickness of one-half and one-quarter thereof, respectively, based on the phase of fundamental mode data, while higher mode data were considered as being unaffected. The rather small differences in the residuals for different lid-thickness as discussed in the previous paragraph, however, seem not to support their conclusions.

The results of this surface wave study are somewhat at odds with the previous study of mantle shear arrivals (Koch, 1993) along identical paths. The body wave velocity model produced higher velocities in the uppermost mantle in order to match the mantle S arrival times. Two explanations for these model differences are most likely. The higher velocities at shallower depth were introduced in order to use smaller gradients at larger depths to prevent synthetic mantle S arrivals at distances shorter than 2000 km in support of the observation. It is thus possible, that the smaller shear velocities at depths shallower than 200 km trade-off with higher velocities at larger depths. This discrepancy might be addressed by inverting longer period surface wave data. A second explanation for the discrepancy lies in the different regions that mantle body waves and surface waves sample at the shallower depths. While the body waves turning below 400 km are quite steeply dipping through the upper 200 km close to the shore line, the surface waves are sampling the upper 200 km of the entire Basin and Range province. Thus, the discrepancies could be indication of the lateral heterogeneous upper mantle in the western United States.

Acknowledgements

This research was supported by the Air Force Phillips Laboratory under contract F19628-91-K-0016.

References

- Al-Khatib, H. & B.Mitchell (1991): Upper mantle anelasticity and tectonic evolution of the western United States from surface wave attenuation, *J. Geophys. Res.*, 96, 18129-18146
- Bache, T.C. W.L.Rodi & D.G.Harkrider (1978): Crustal structures inferred from Rayleigh-wave signatures of NTS explosions, *Bull.Seism.Soc.Am.*, 68, 1399-1413
- Ben-Menahem, A. & D.G. Harkrider (1964): Radiation patterns of seismic surface waves from buried dipolar point sources in a flat stratified earth, *J. Geophys. Res.*, 69, 2605-2620
- Benz,H., R.B.Smith, and W.D.Mooney (1990): Crustal structure of the north-western Basin and Range province from the 1986 program for array seismic studies of the continental lithosphere seismic experiment, *J.Geophys.Res.*, 95, 21823-21842
- Bloch, S., A.L.Hales & M.Landisman (1969): Velocities in the crust and upper mantle of southern Africa from multi-mode surface wave dispersion, *Bull.Seism. Soc.Am.*, 59, 1599-1629
- Campillo, M. & A. Paul (1992): Influence of the lower crustal structure on the early coda of regional seismograms, *J.Geophys.Res.*, 97, 3405-3416
- Der, Z.A. (1986): Comments on the paper 'Estimation of scalar moments from explosion-generated surface waves' by Jeffry.L.Stevens, *Bull.Seism.Soc. Am.*, 76, 1822-1824
- Dziewonski,A.M, S.Bloch & M.Landisman (1969): A technique for the analysis of transient seismic signals, *Bull.Seism.Soc.Am.*, 59, 429-444
- Goforth, T. & F.T. Herrin (1979): Phase-matched filters: application to the study of Love waves, *Bull.Seism.Soc.Am.*, 69, 27-44
- Grand, S.P. & D.V.Helmberger (1984): Upper mantle shear structure of North America, *Geophys.J.R.astr.Soc.*, 76, 399-438
- Harkrider, D. G. (1970): Surface waves in multilayered media. Part II. Higher mode spectra and spectral ratios from point sources in plane-layered earth models, *Bull.Seism.Soc.Am.* 60, 1937-1987
- Herrin, E. & T. Goforth (1977): Phase-matched filters: application to the study of Rayleigh waves, *Bull.Seism.Soc.Am.*, 67, 1259-1275
- Herrmann, R.B. (1988): Computer programs in seismology, Vols. II-IV, St.Louis University

- Jin, D.J. & E.T. Herrin (1980): Surface wave studies of the Bering sea and Alaska area, *Bull.Seism.Soc.Am.*, 70, 2117-2144
- Koch, K. & B.Stump (1993): Implications for upper mantle structure in the Western United States from complete far-regional seismograms, submitted to *Bull.Seism.Soc.Am.*
- Koch, K. (1993): On short period mantle S waves for large regional propagation paths in the Western United States, this report
- Koizumi, C.J., A.Ryall & K.Priestley (1973): Evidence for a high-velocity litho-spheric plate under northern Nevada, *Bull.Seism.Soc.Am.*, 63, 2135-2144
- Priestley, K. & J.N.Brune (1978): Surface waves and the structure of the Great Basin of Nevada and western Utah, *J.Geophys.Res.*, 83, 2265-2272
- Priestley, K., J.Orcutt & J.N.Brune (1980): Higher-mode surface waves and structure of the Great Basin of Nevada and western Utah, *J.Geophys.Res.*, 85, 7166-7174
- Russell, D.R., R.B.Herrmann & H.-J.Hwang (1988): Application of frequency variable filters to surface wave amplitude analysis, *Bull. Seism. Soc. Am.*, 78, 339-354
- Seidl, D. (1980): The simulation problem for broad-band seismograms, *J.Geophys.*, 48, 84-93
- Stevens, J.L. (1986): Estimation of scalar moments from explosion-generated surface waves, *Bull.Seism.Soc.Am.*, 76, 123-151

Appendix: A summary of the theory of phase-matched filtering

Starting from a group velocity estimate, i.e. from a group velocity dispersion curve for particular continental path already published or from the MFT analysis, the group delay is estimated. The group delay (T_{gr}) is determined from the group velocity (U)

$$T_{gr}(\omega) = \frac{R}{U(\omega)} \quad (A.1)$$

where R is the epicentral distance (in km) between source and receiver for the single station method or the great circle path distance between two stations in the case of the two station method. From standard textbooks (e.g. Papoulis (1962)), it is well known that the group delay in turn represents the derivative of the phase spectrum, i.e.

$$T_{gr}(\omega) = \frac{d\Theta(\omega)}{d\omega} \quad (A.2)$$

with $\Theta(\omega)$ denoting the phase spectrum representing the trial group velocity dispersion curve. After integration, we obtain the phase spectrum, which is determined up to a constant factor:

$$\Theta(\omega) = \int_0^{\omega} T_{gr}(\Omega) d\Omega \quad (A.3)$$

The retrieved phase spectrum can then be used to calculate phase velocity through the formula given in the text.

With an estimate of the phase of the signal, we can build a phase-matched filter (Herrin & Goforth, 1977), which matches its phase spectrum to that of a given signal, in surface wave analysis the recorded Love and Rayleigh waveforms. The phase spectrum of the filter is obtained through the calculation of the Pseudo-Autocorrelation-Function (PAF) by multiplying the observed surface wave spectrum with the estimated phase spectrum, yielding

$$\begin{aligned} \text{PAF}(\omega) &= |S(\omega)| \cdot e^{i\sigma(\omega)} \cdot e^{-i\Theta(\omega)} & (\text{A.4}) \\ &= |S(\omega)| \cdot e^{i[\sigma(\omega)-\Theta(\omega)]} \end{aligned}$$

and which, hence the notion, represents the autocorrelation function if the observed and the matched phase are the same. In the relation above, $S(\omega)$ is the signals amplitude spectrum and $\sigma(\omega)$ is its phase spectrum, the searched for parameter. From this relation, a iterative procedure is performed, until the PAF is as close as possible to an autocorrelation function. With proper windowing of the PAF, only the correlated phases in the frequency band of interested are included, and multipathed arrivals, body wave arrivals, noise, or higher modes with large phase differences are rejected.

Table 1: Summary of event parameters ^{o)}

No.	Date	Origin Time	Latitude	Longitude	Depth	M _B	M _{sz}	Range ^{†)}
1	01/16/1990(016)	200822.0	40.232N	124.138W	2	5.1	5.5	2223
2	07/31/1990(212)	031946.8	42.416N	126.682W	10	5.7	5.4	2519
3	07/13/1991(194)	025014.7	42.182N	125.641W	11	6.2	6.9	2427
4	08/16/1991(228)	222617.2	41.697N	125.385W	10	5.5	6.3	2389
5	08/17/1991(229)	192940.0	40.235N	124.348W	12	6.0	6.2	2235
6	08/17/1991(229)	221714.7	41.821N	125.397W	14	6.2	7.1	2391
7 ^{†)}	03/08/1992(069)	034304.4	40.228N	124.291W	13	5.3	5.5	2231
8	04/25/1992(116)	180604.2	40.368N	124.316W	15	6.3	7.1	2239
9	04/26/1992(117)	074139.7	40.415N	124.603W	20	5.9	6.6	2263
10	04/26/1992(117)	111825.7	40.378N	124.575W	26	6.5	6.6	2260

^{o)}

NEIC : PDE - Monthly Listings

^{†)}

Epical distance to Lajitas, TX (LTX) from PDEs

^{‡)}

Data from QED

Figure captions

- 1: Broad-band seismograms observed at Lajitas (LTX) and used in surface wave inversions; (a) transverse component seismograms (Love waves); (b) vertical component seismograms (Rayleigh waves) (Note: traces with BS are broad-band simulations from the short-period records; compare traces T(V)-BB and T(V)-BS of event 1992_069)
- 2: (a) Result of multiple filter (MFT) analysis to obtain group velocity estimate for the event of July 13, 1991 off the coast of Oregon, with strike-slip source mechanism, analyzing the complete record; (b) same as (a), but signal including the impulsive mantle S arrival were windowed out.
- 3: Group velocity dispersion curves for Love wave for all data shown in Figure 1a between 100 sec and 3 sec period; solid lines and symbols indicate off-shore events, while on-shore events are indicated by hatched lines.
- 4: Result of MFT analysis to obtain group velocity estimate for Rayleigh waves using the vertical component records from (a) event 1991_194 (same events as used in Figure 2) and (b) event 1991_229f on the coast of Northern California, with normal-faulting source mechanism.
- 5: Group velocity dispersion curves for Rayleigh waves for (a) vertical and (b) radial component data between 100 sec and 3 sec period; off-shore events (solid), on-shore (hatched), strike-slip events (thin lines), normal faulting events (thick lines).
- 6: Results from phase-matched filtering (PMF): (a) group and phase velocity dispersion curves for Love waves; (b) seismograms from PMF of data in Figure 1a.
- 7: Results from PMF: (a) group and phase velocity dispersion curves for Rayleigh waves using vertical component records only; (b) seismograms from PMF of data in Figure 1b.
- 8: Previously used shear-wave models from Koch (1993) (open symbols) and Priestley & Brune (1978) (crosses) in the depth range 0-400 km.

- 9: Theoretical dispersion curves (group/phase velocities) for the velocity models shown in Figure 8 (symbols correspond to those used there) and comparison with the measured values (circles); (a) for Love wave and (b) for Rayleigh wave dispersion. In both cases, the shorter period observations are closer to the dispersion predicted from models proposed by Koch (1993) while the very long period observations better match the predictions from Priestley & Brune's model (1978).
- 10: Inversion of the Love wave dispersion values from event 1991_194 which was considered as having superior signal to noise ratio within the used frequency band.
- 11: Inversion of the Love wave dispersion curves averaged over all events
- 12: Same as in Figure 11 but for Rayleigh wave dispersion curves; (a) initial inversion result for 5 iterations, (b) result for 10 iterations to test stability of results
- 13: Same as in Figure 12 but for both Love and Rayleigh wave dispersion curves for two different starting models; (a) is the model with the triangular symbols in Figure 8, and (b) is for the model represented by diamonds
- 14: Average dispersion data at LTX for surface waves propagating across the Basin and Range from events in Northern California and off the coast of Oregon. Error bars give standard deviations computed from the dispersion curves given in Figures 7-8. These error estimates were used in the inversions shown in Figures 11-13. Also shown are the predicted group and phase velocities for the model in Figure 13a.
- 15: Velocity models and dispersion curves determined from inversions which used only the residuals between data and model. The dotted line is for a model including the standard errors of the data in the inversion, while solid and dashed line is for the inversions which considered only the residuals. The solid line is for model with simple lower crust, while dashed and dotted models include a 3-layered lower crust. The velocity structure (high-velocity region) in the low velocity layer is enhanced due to the better fit of the Rayleigh wave group velocities.

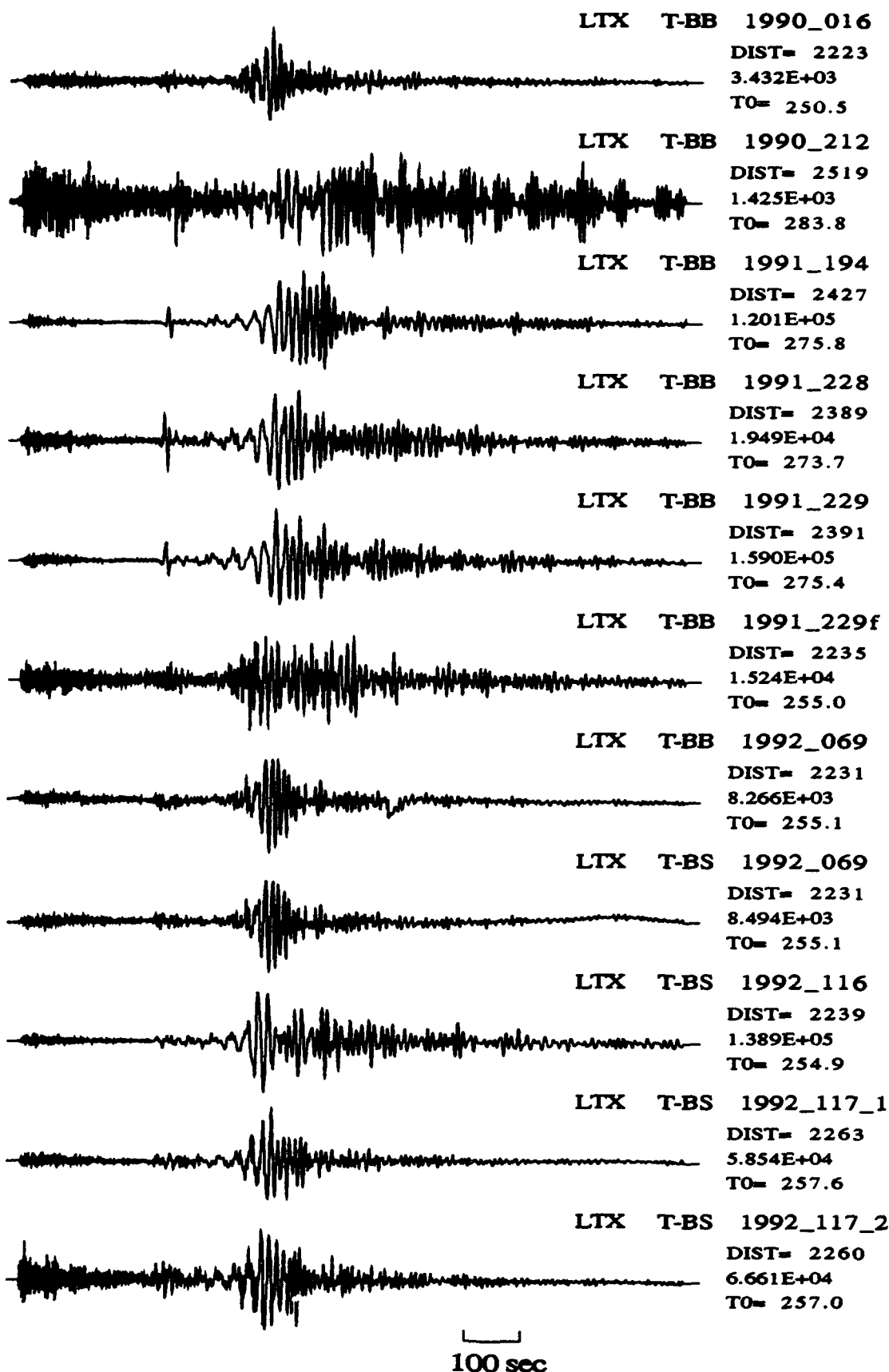


Figure 1a

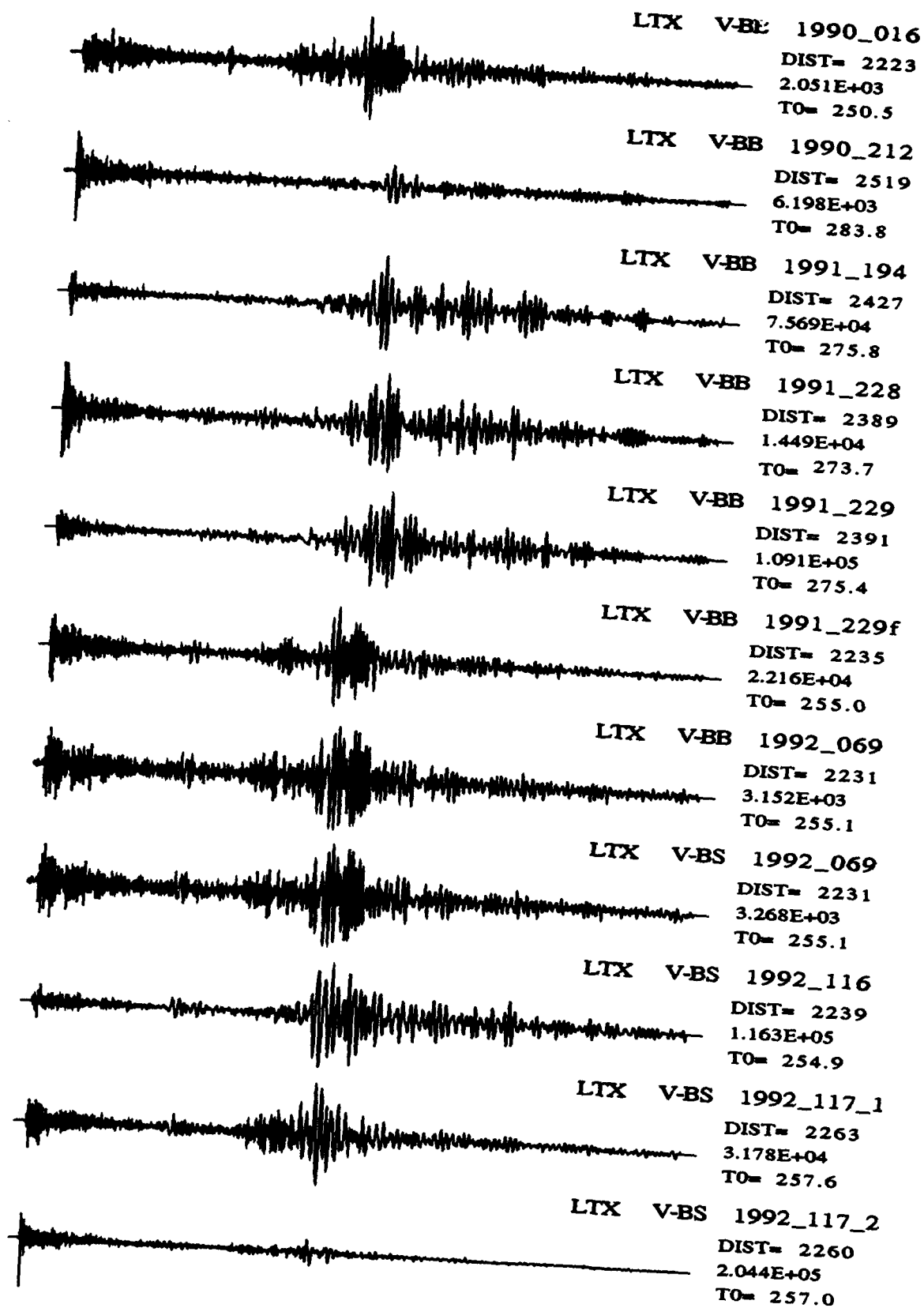


Figure 1b

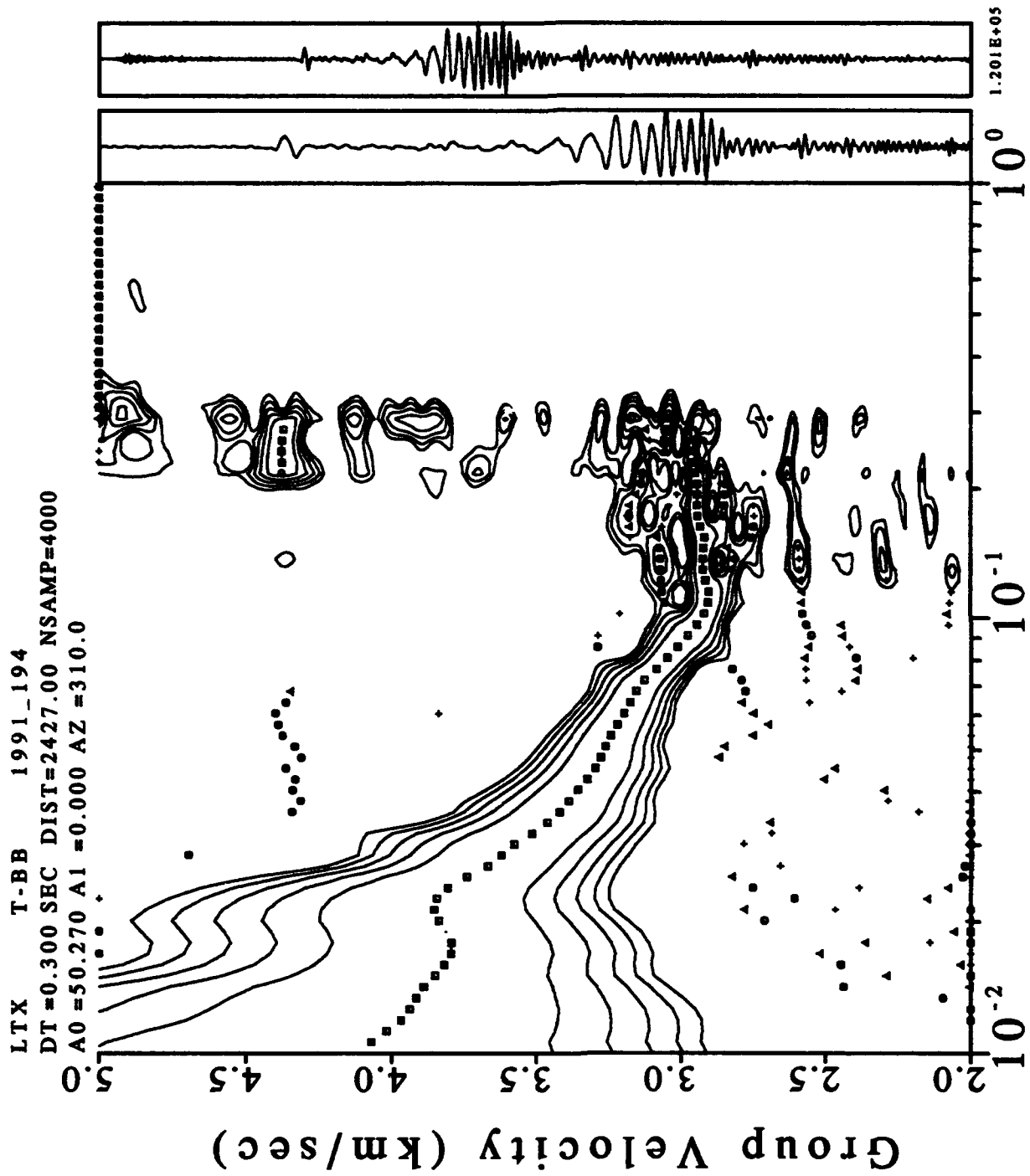


Figure 2a

LTX T-BB 1991_194
 DT=0.300 SEC DIST=2427.00 NSAMP=4000
 A0=50.270 A1=0.000 AZ=310.0

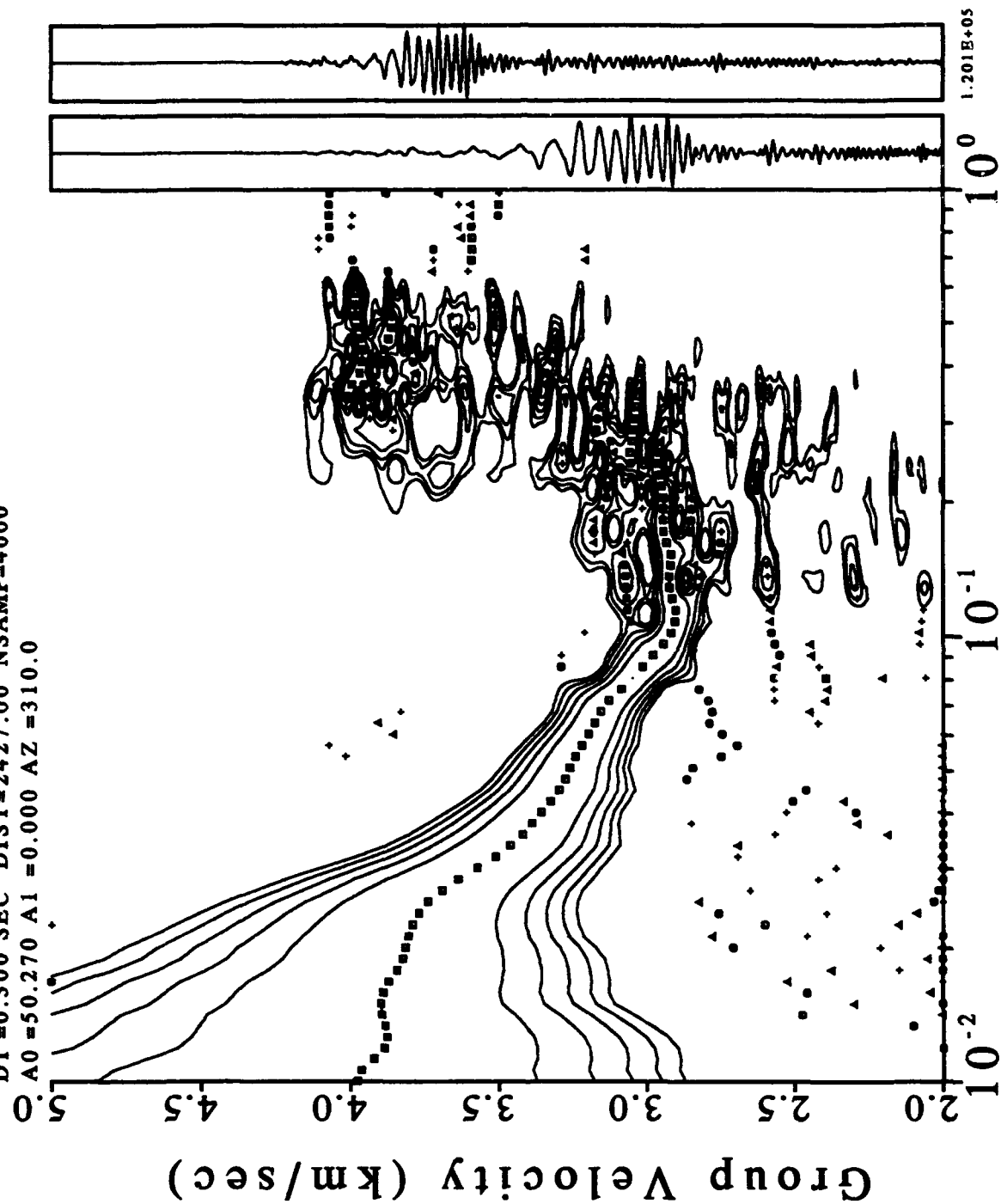


Figure 2b

Group velocities for Northern California events at LTX Periods from 100 to 3 sec

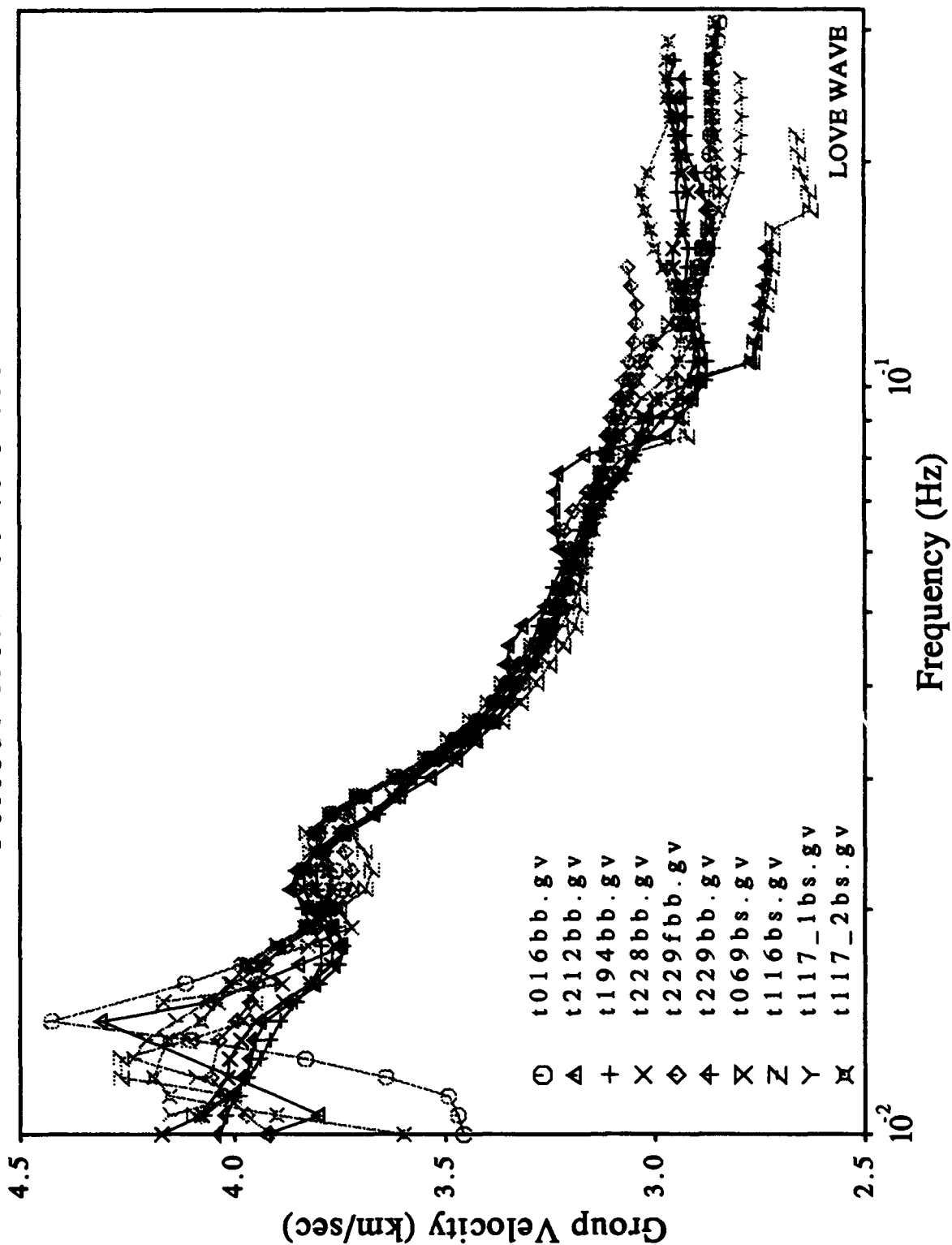


Figure 3

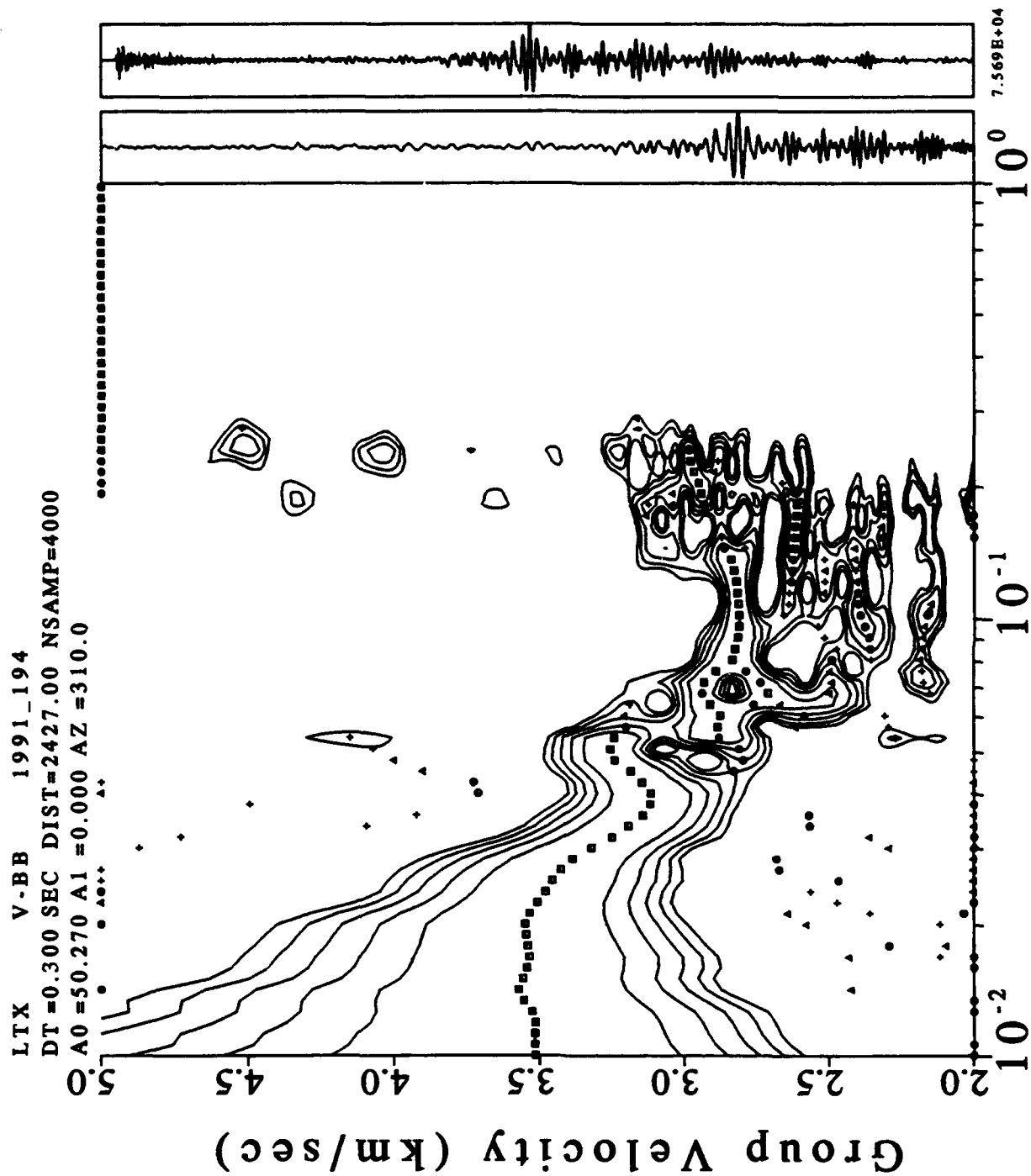


Figure 4a

LTX V-BB 1991_229f
 DT=0.300 SEC DIST=2235.00 NSAMP=4000
 A0=50.270 A1=0.000 AZ=310.0

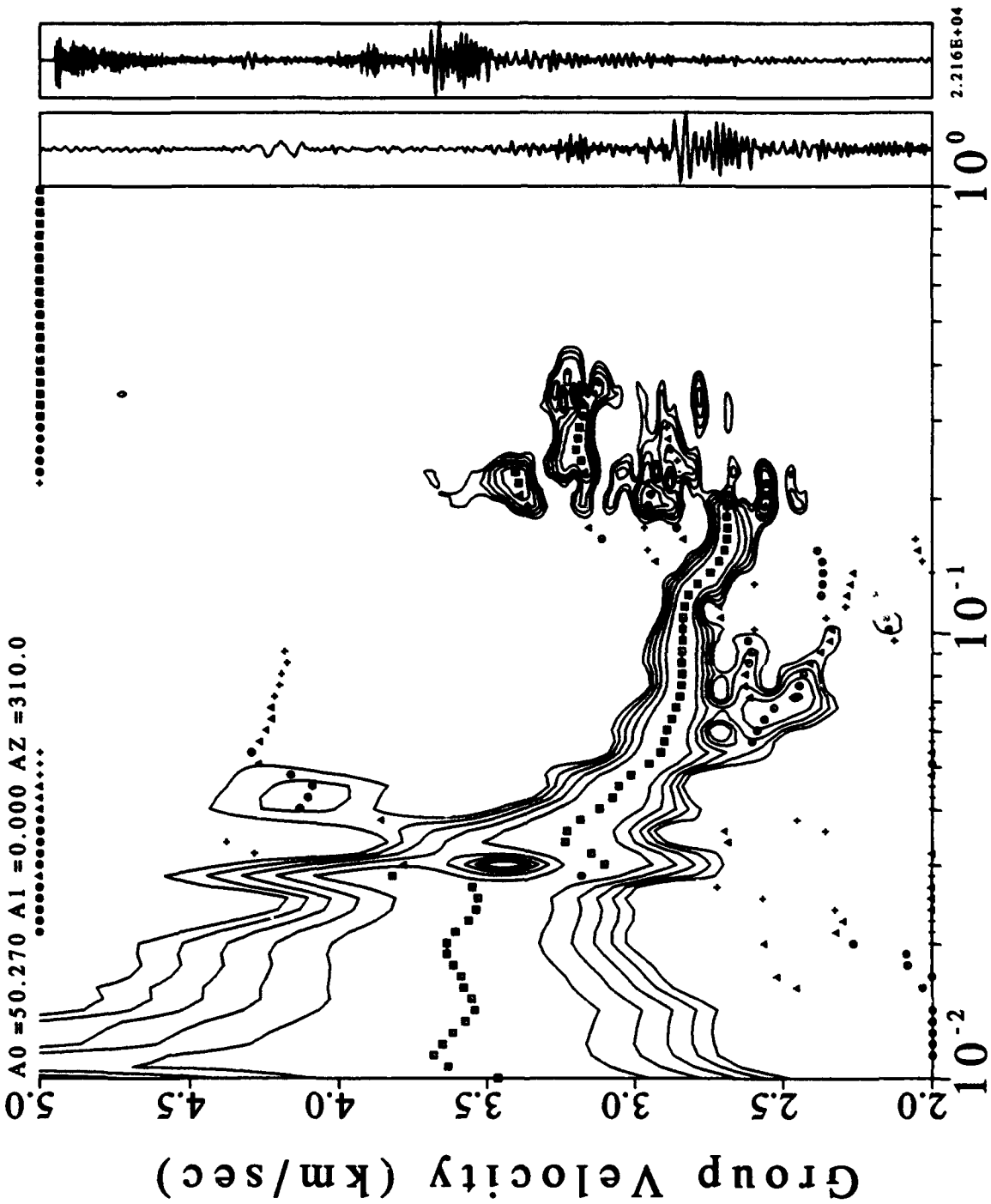


Figure 4b

Group velocities for Northern California event at LTX Periods from 100 to 3 sec

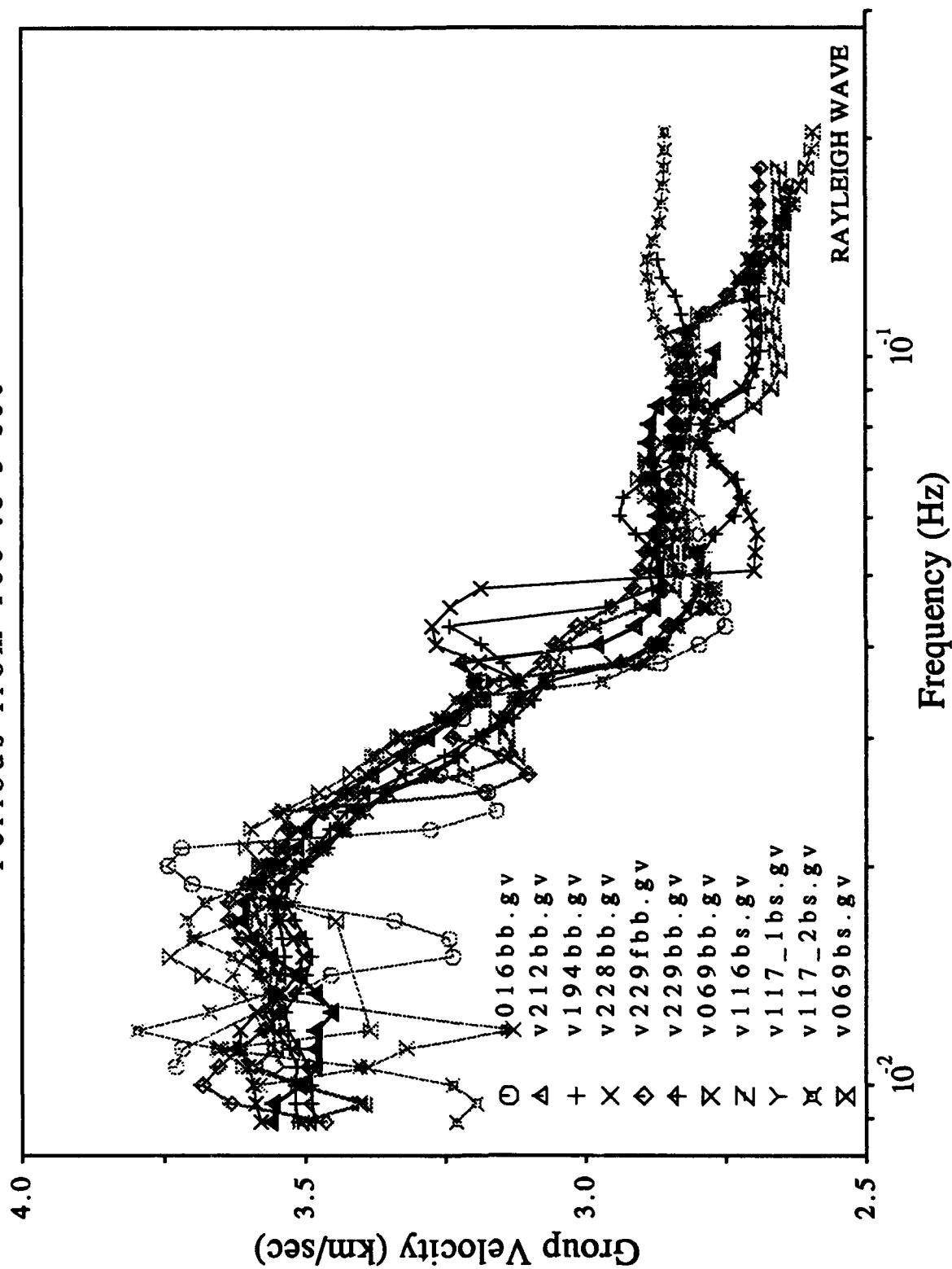


Figure 5a

Group velocities for Northern California events at LTX Periods from 100 to 3 sec

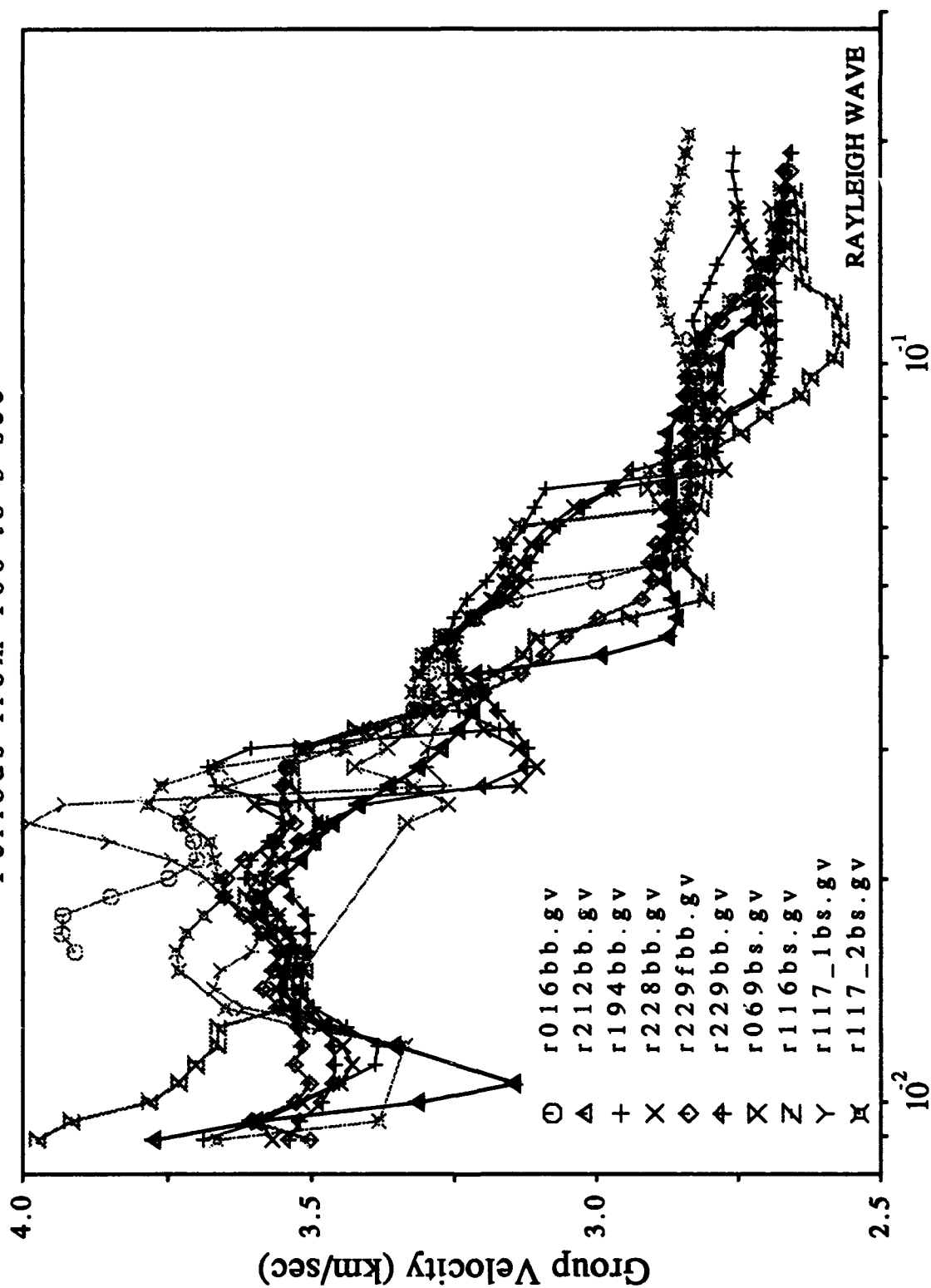


Figure 5b

Phase and group velocities from phase-matched filtering

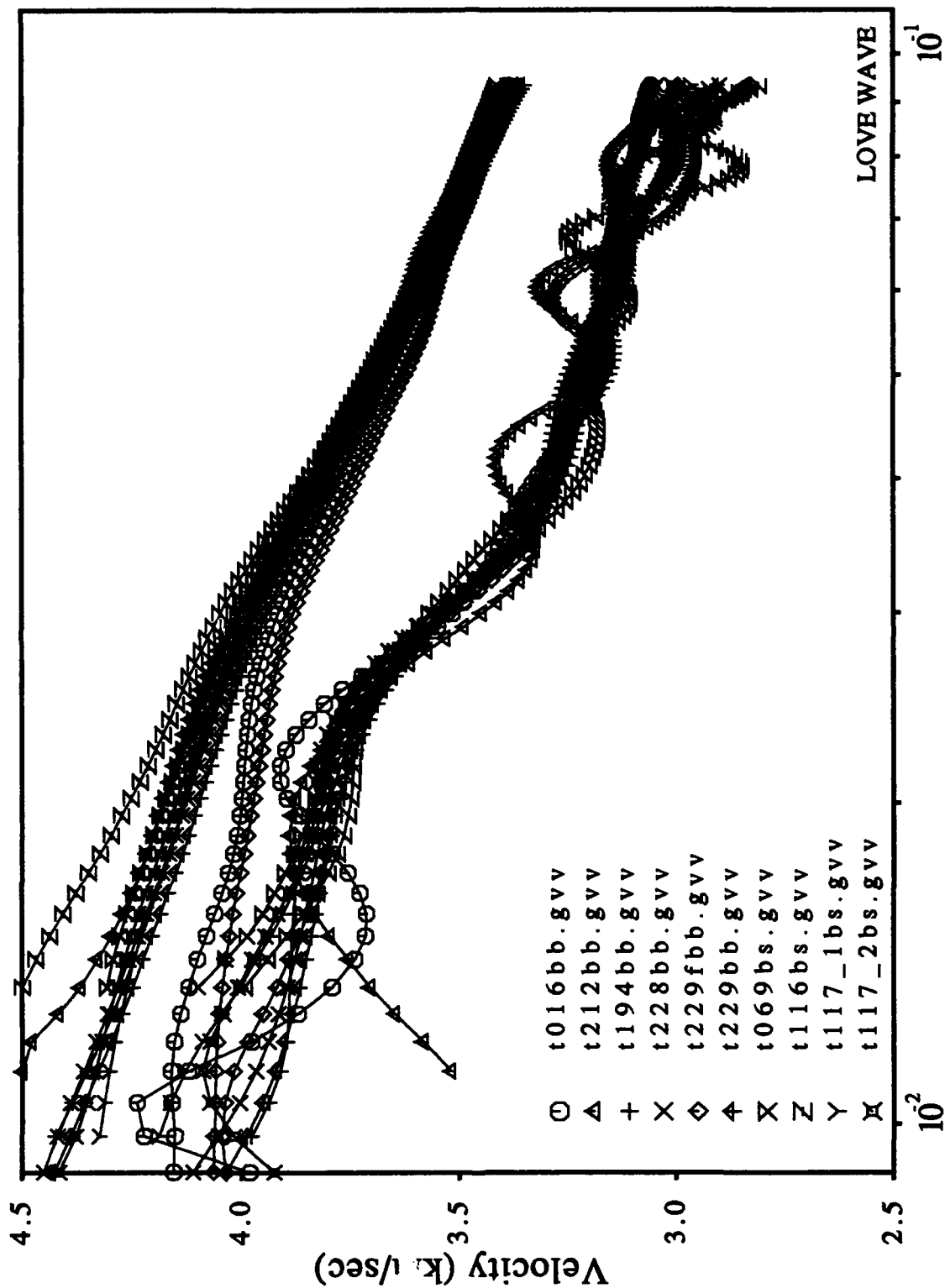


Figure 6a

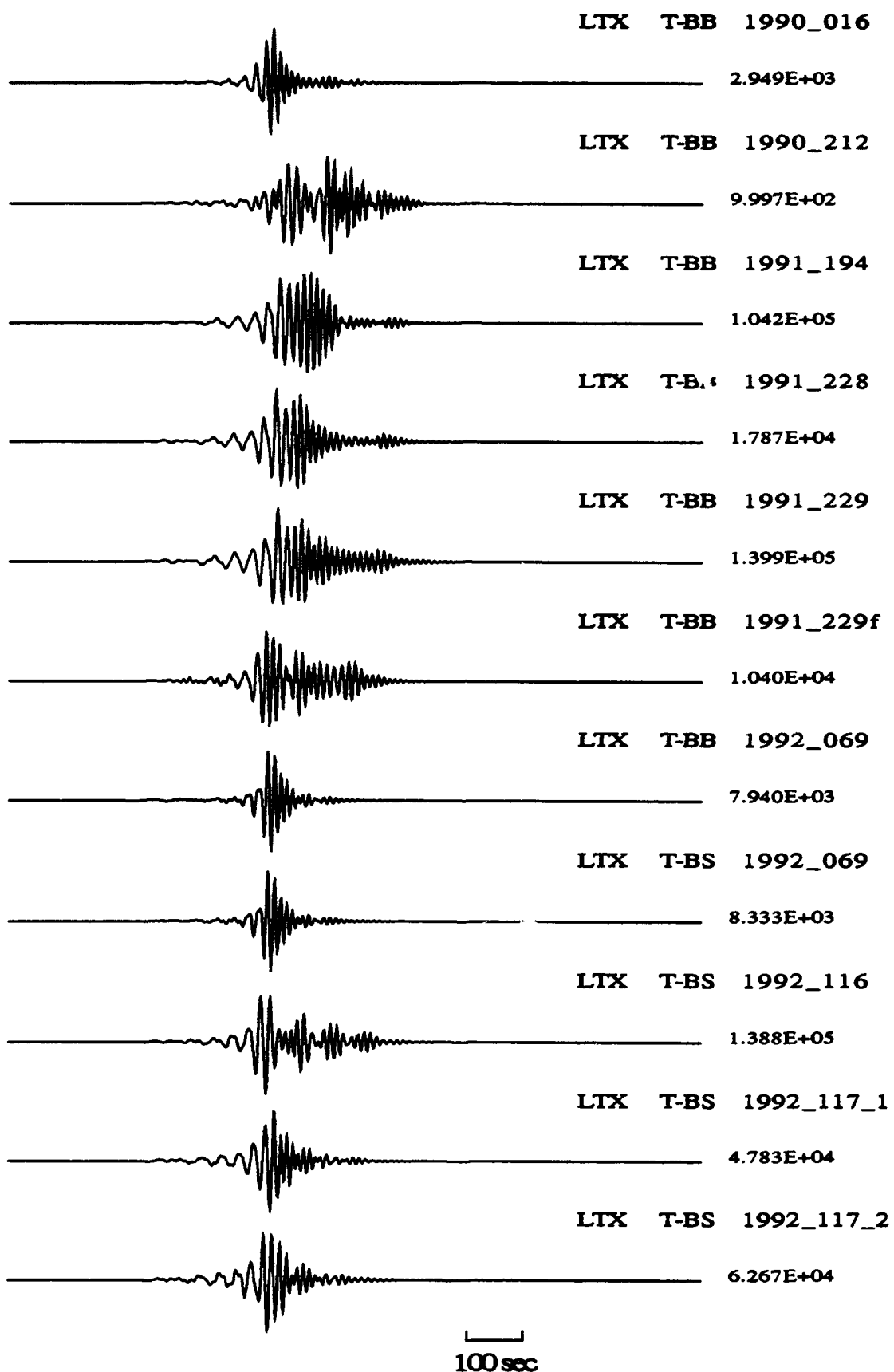


Figure 6b

Group and phase velocities from phase-matched filtering

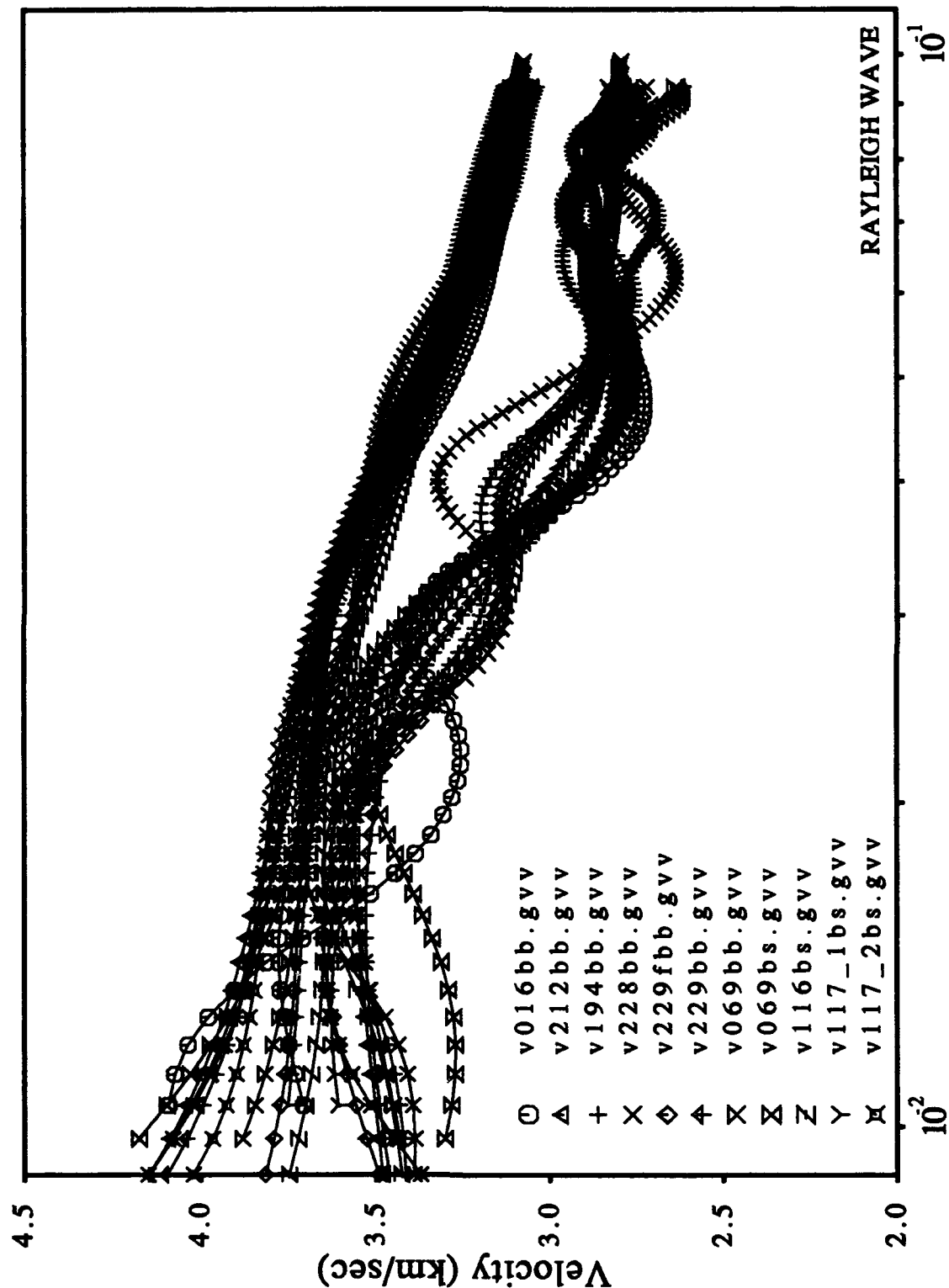


Figure 7a

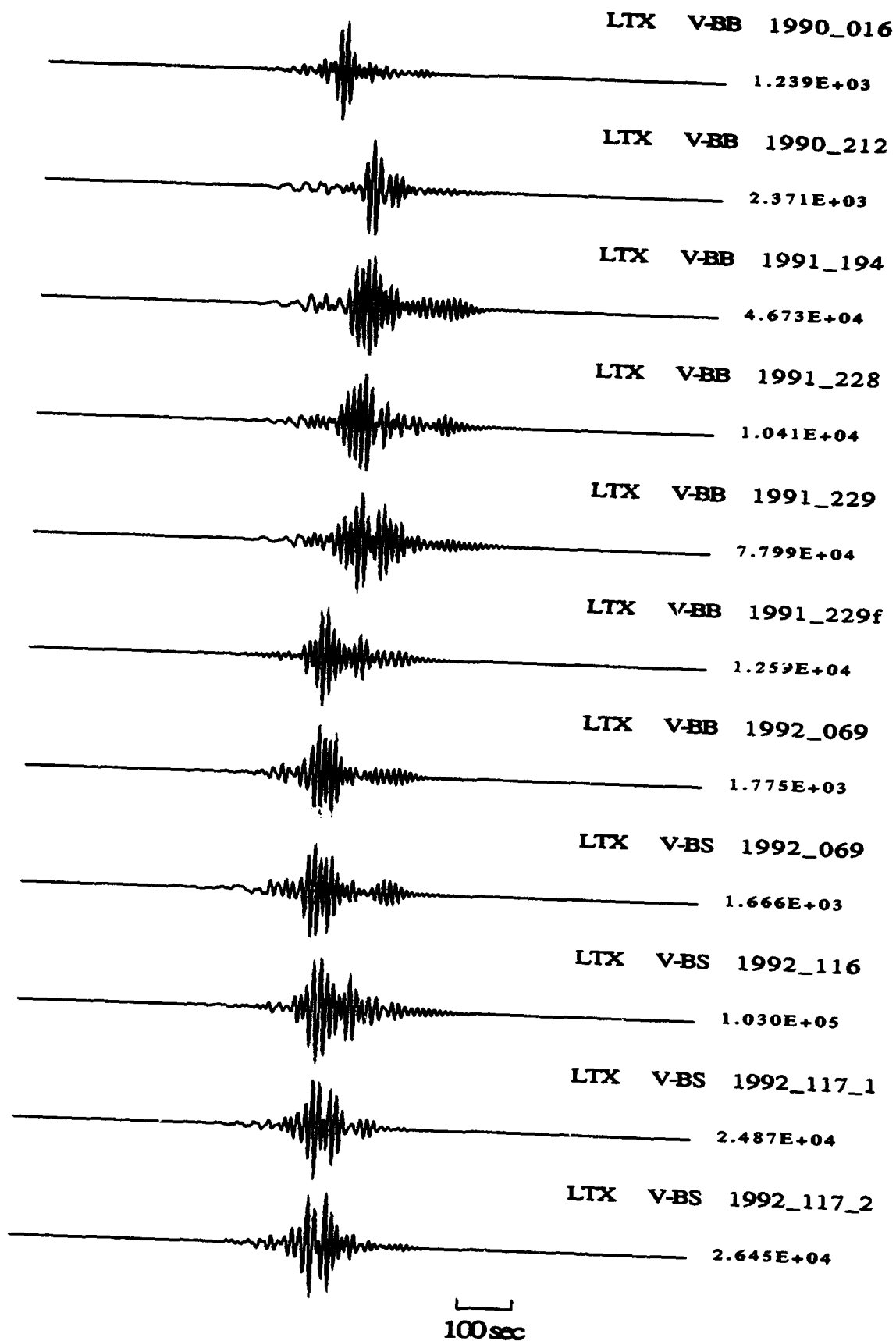


Figure 7b

Velocity models from mantle S-wave modelling

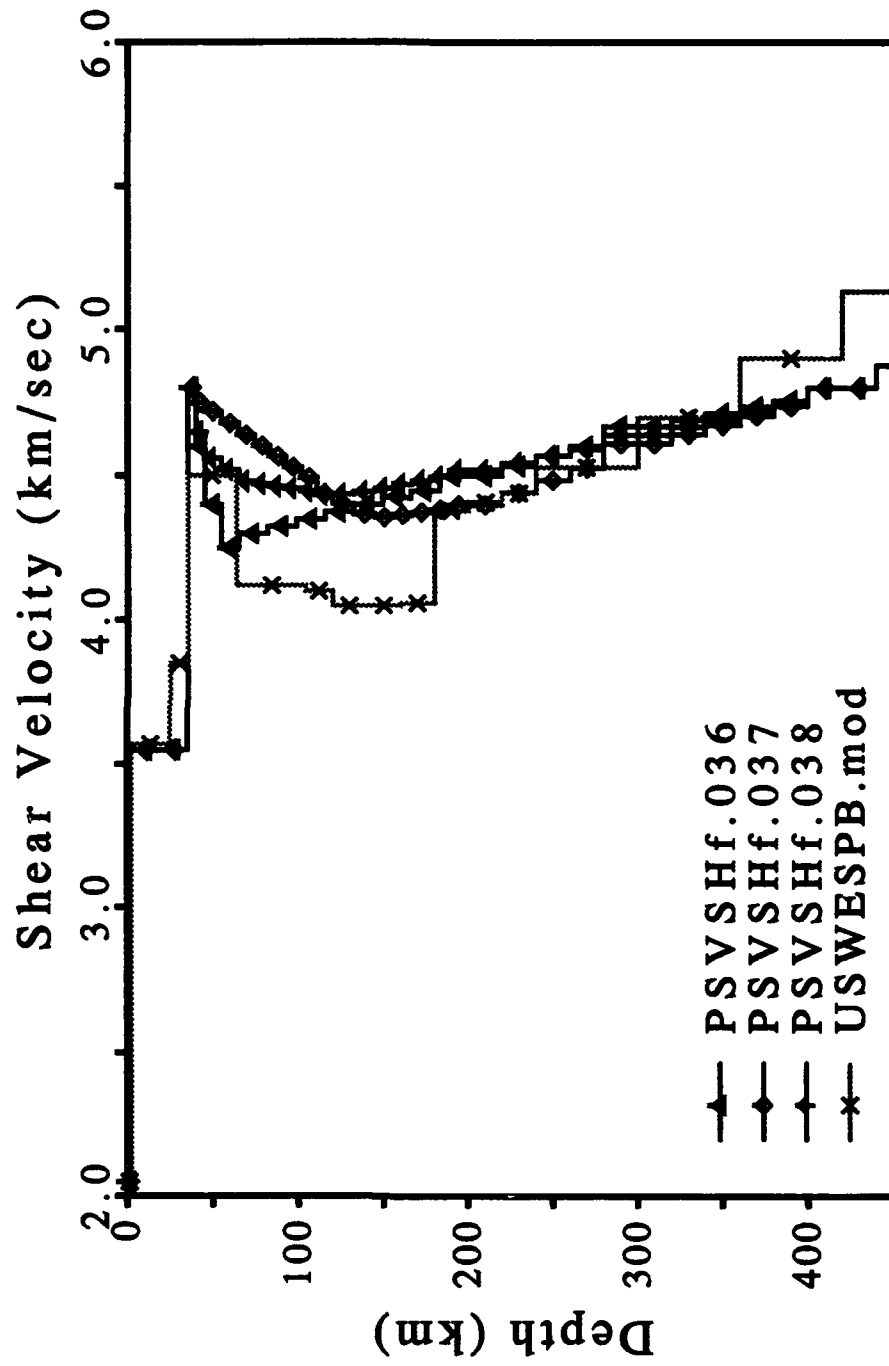


Figure 8

Dispersion Curves for Inversion Models Northern California events at LTX

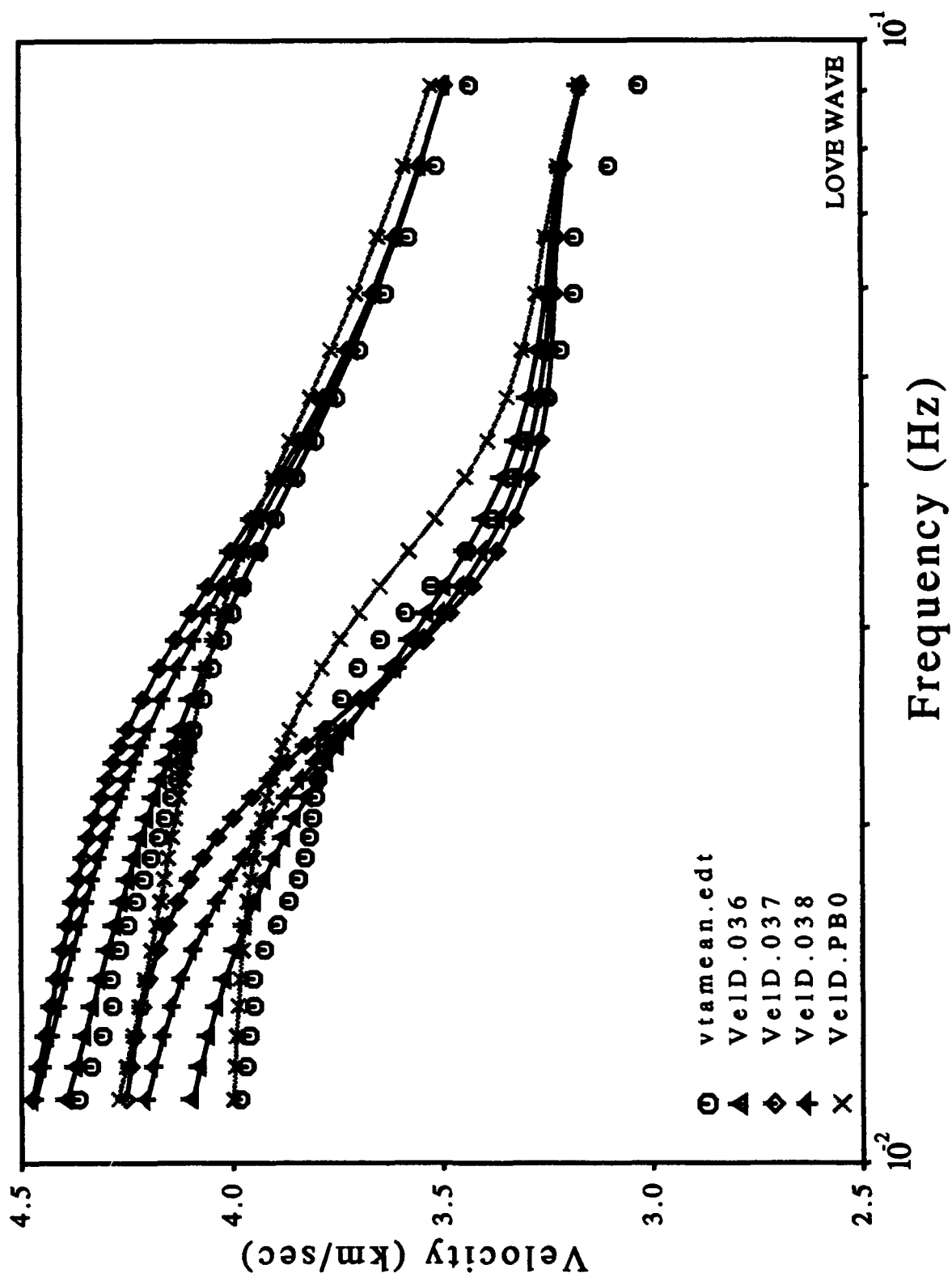


Figure 9a

Dispersion Curves for Inversion Models Northern California events at LTX

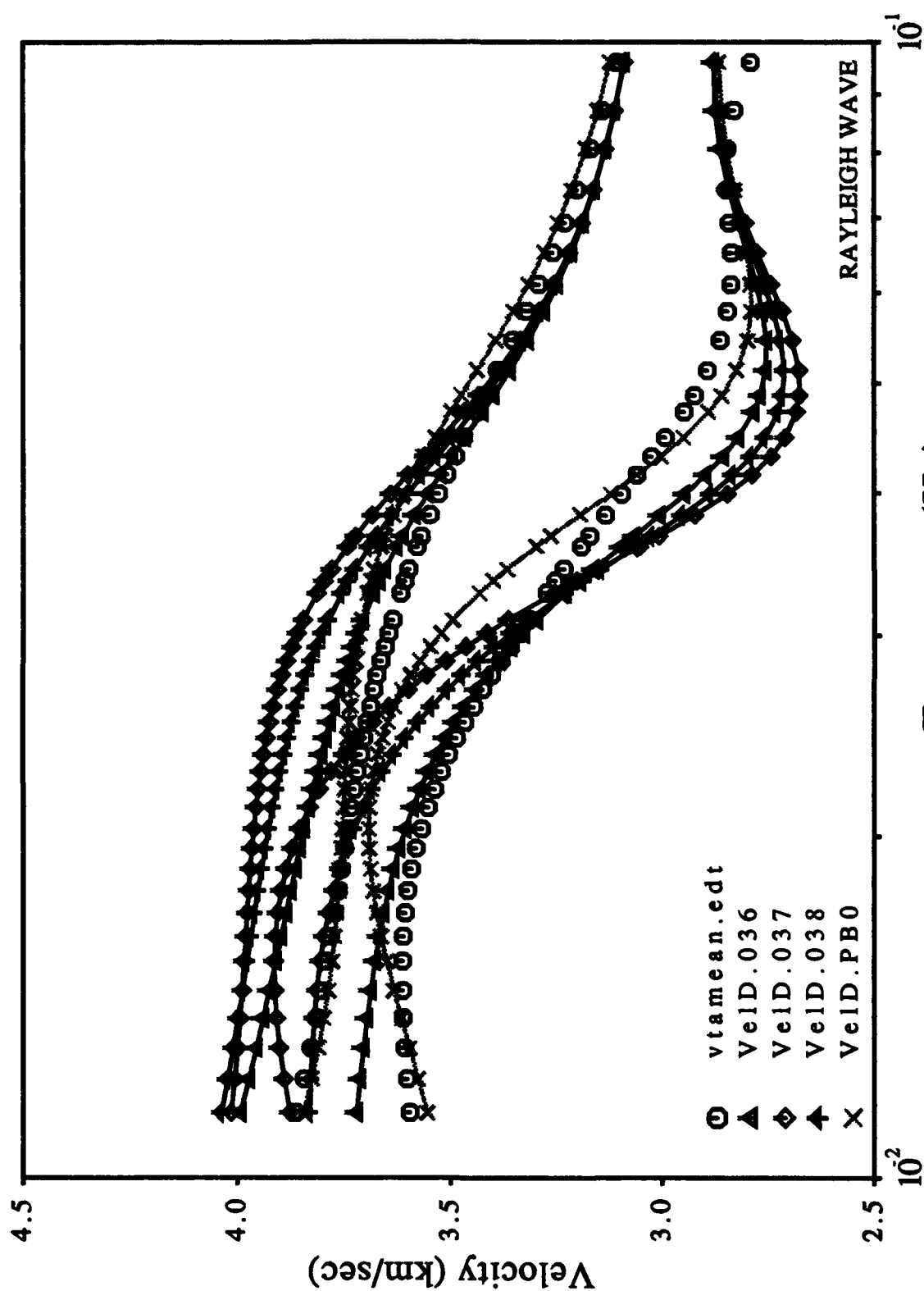


Figure 9b

Velocity inversion - Love waves (1991_194)

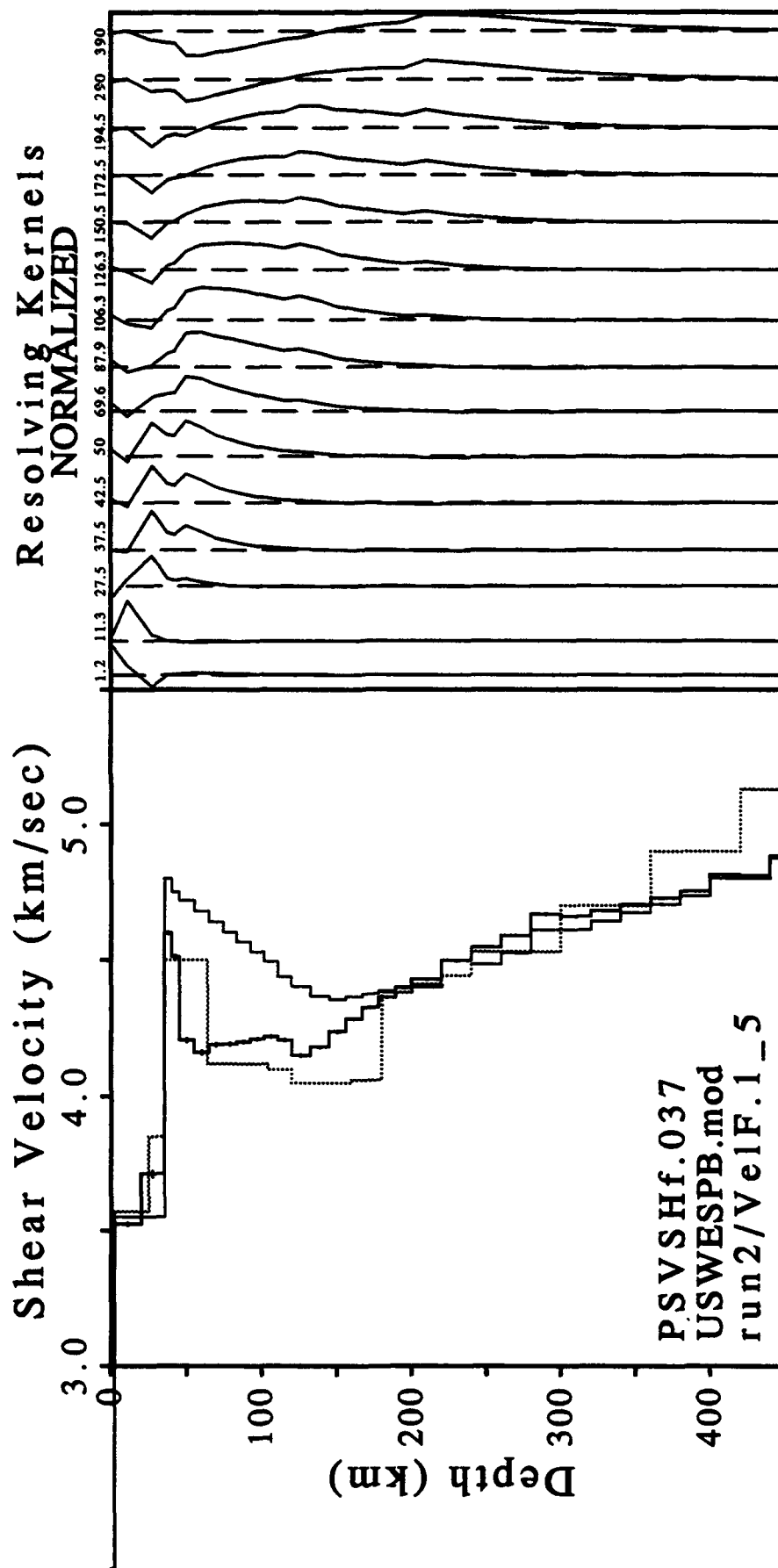


Figure 10

Velocity inversion - Love waves (10-100 sec)

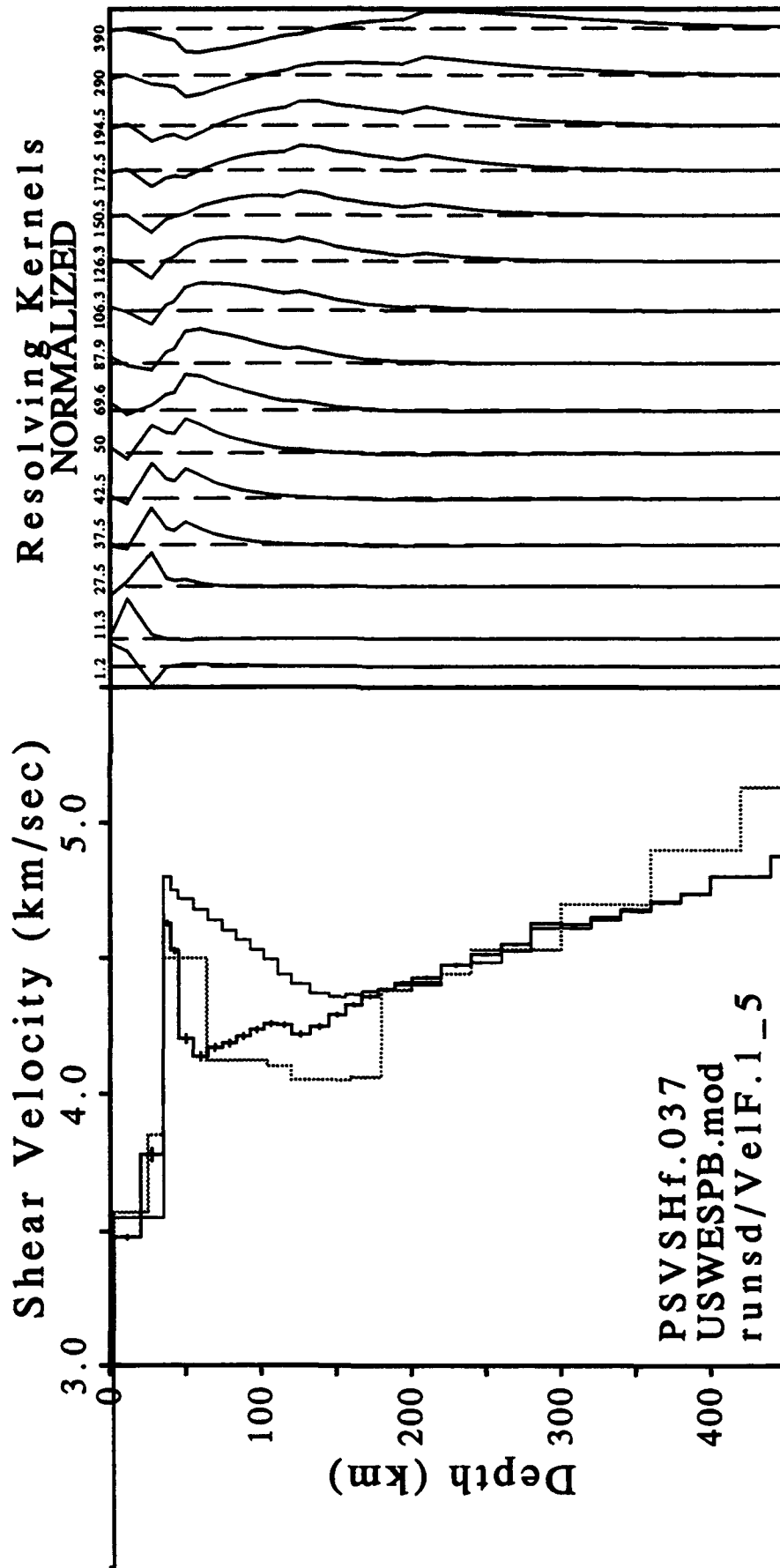


Figure 11

Velocity inversion - Rayleigh waves (vertical component)

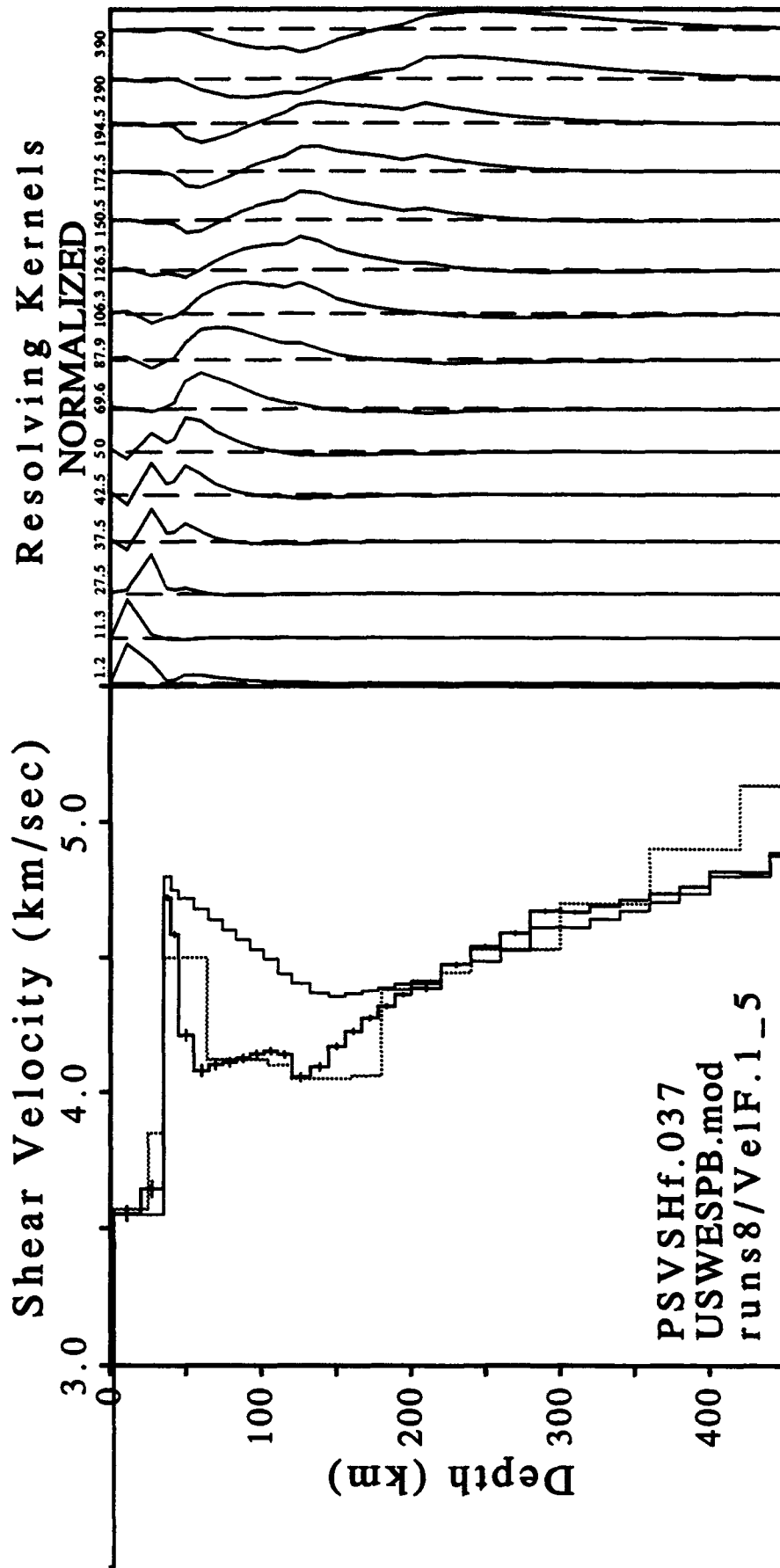


Figure 12a

Velocity inversion - Rayleigh waves (vertical component)

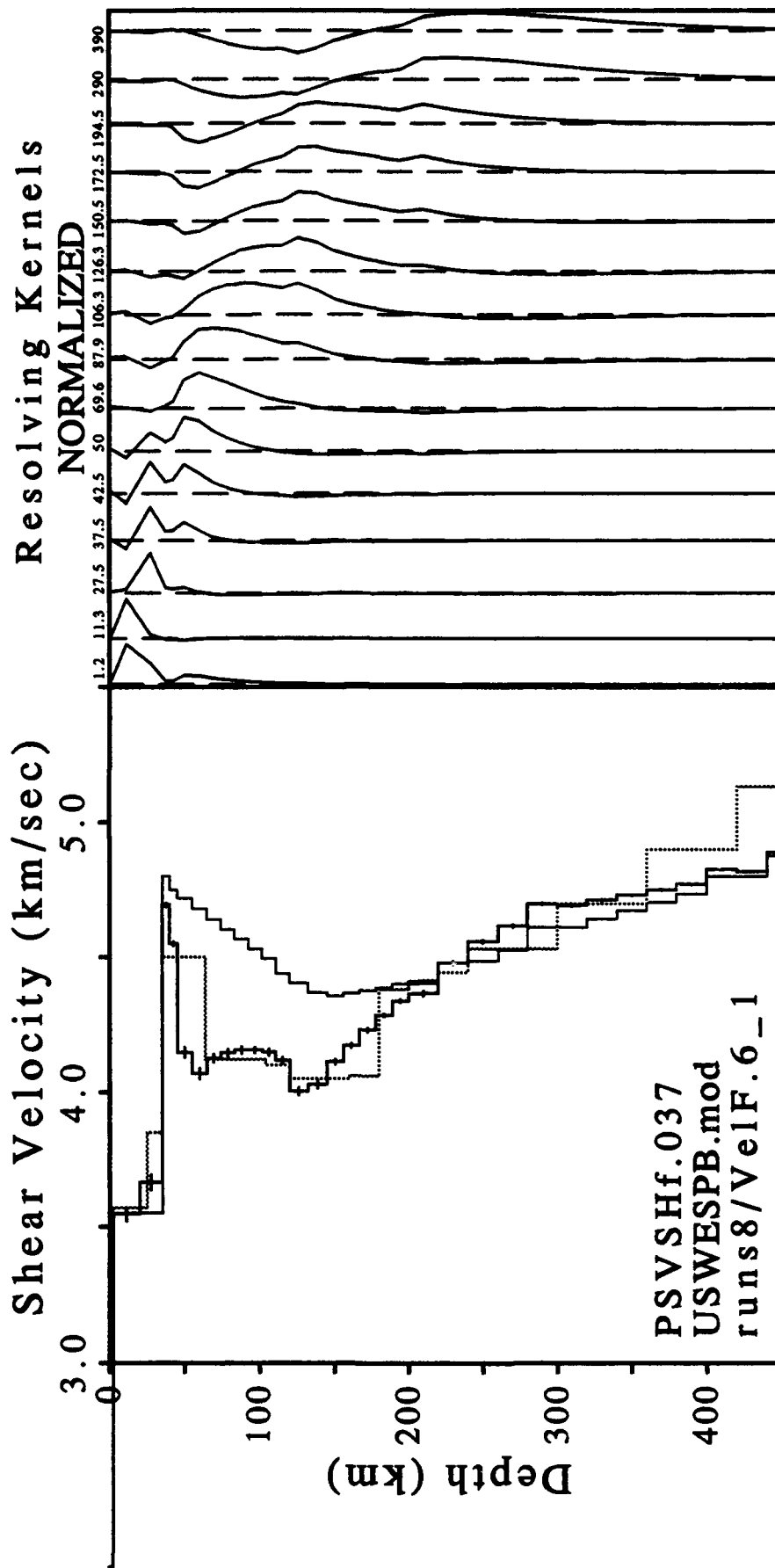


Figure 12b

Velocity inversion - Rayleigh and Love waves (10-100 sec)

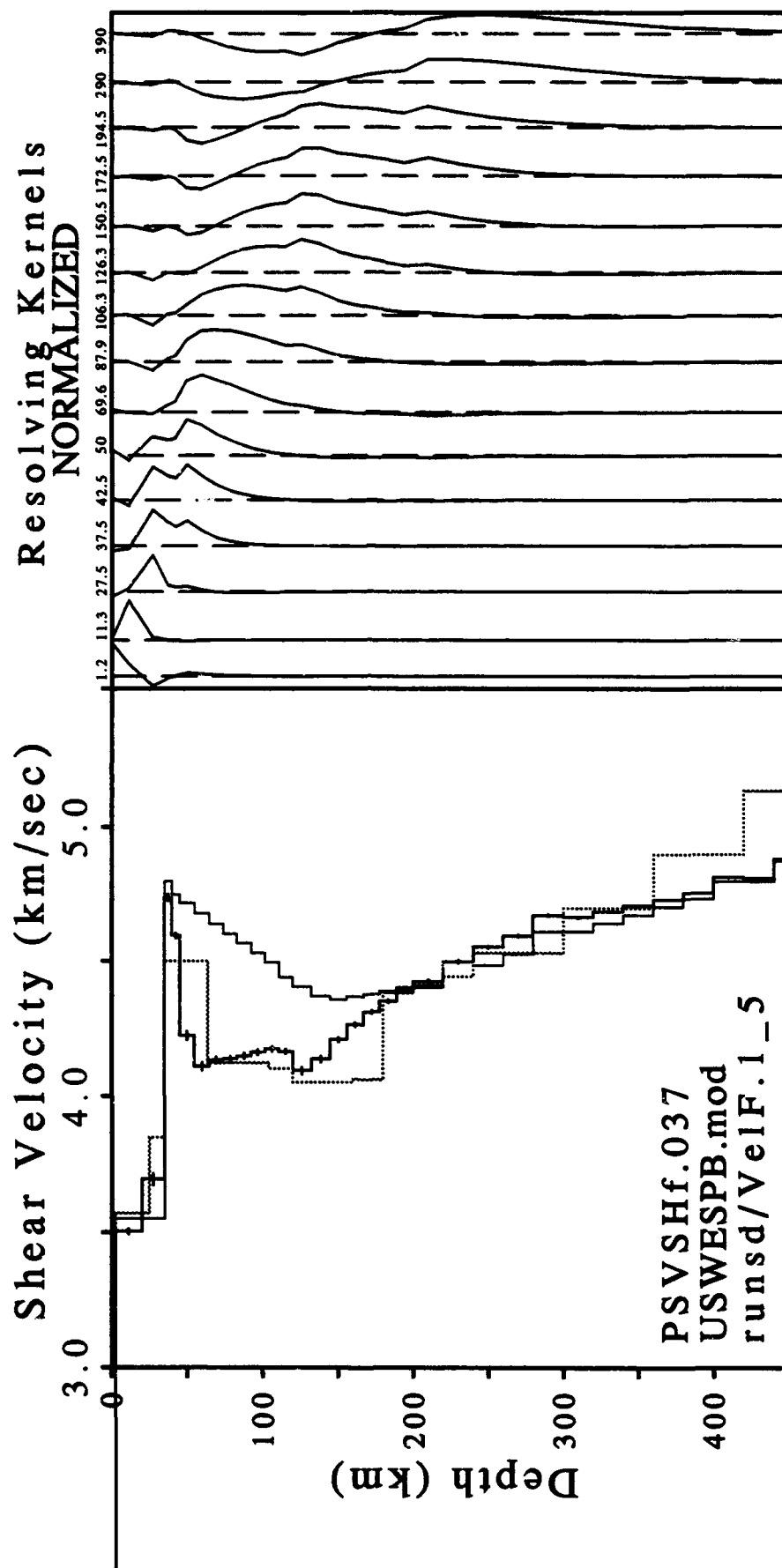


Figure 13a

Velocity inversion - Rayleigh and Love waves (10-100 sec)

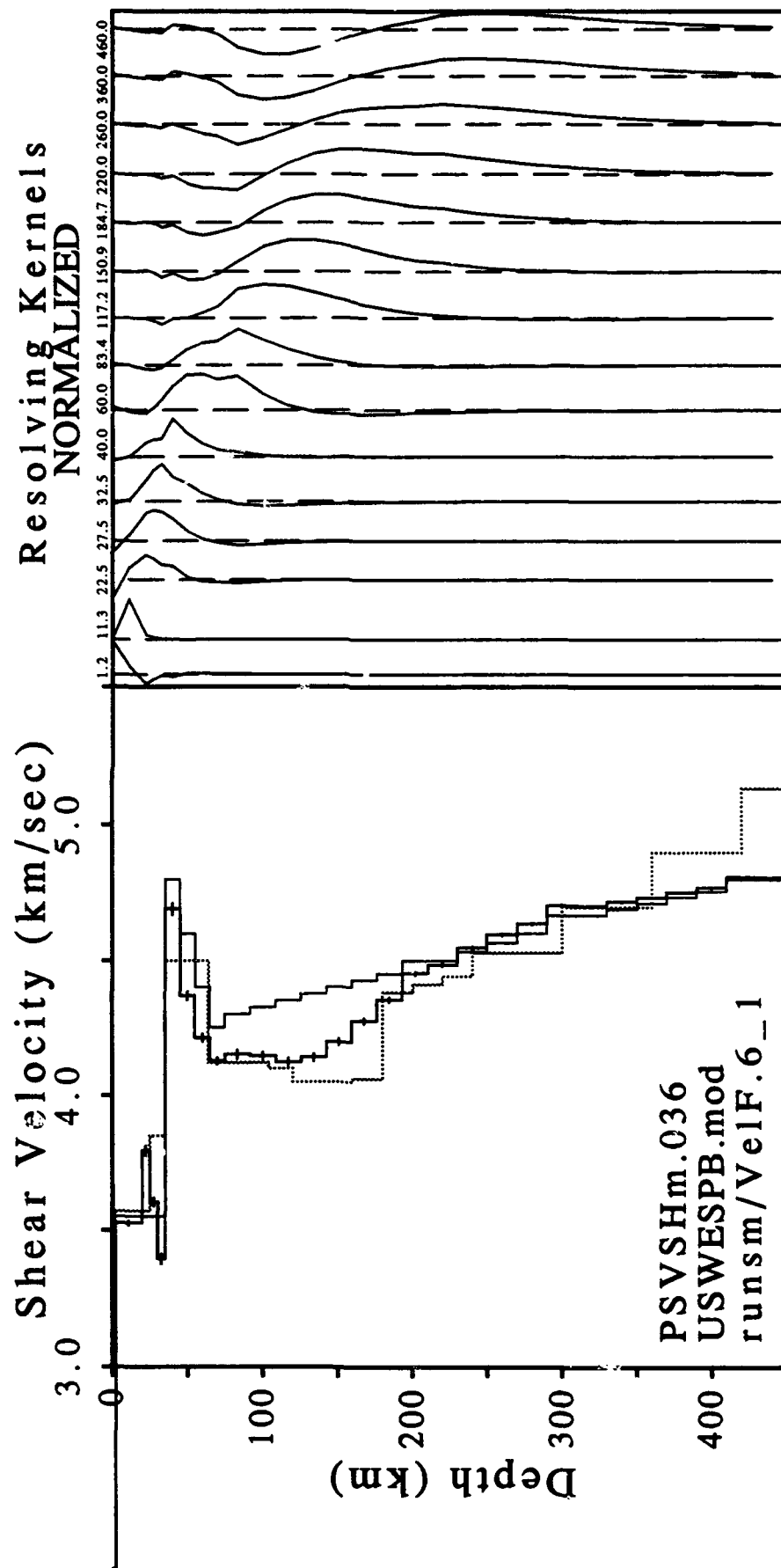


Figure 13b

Measured Dispersion and Curves from Inversion

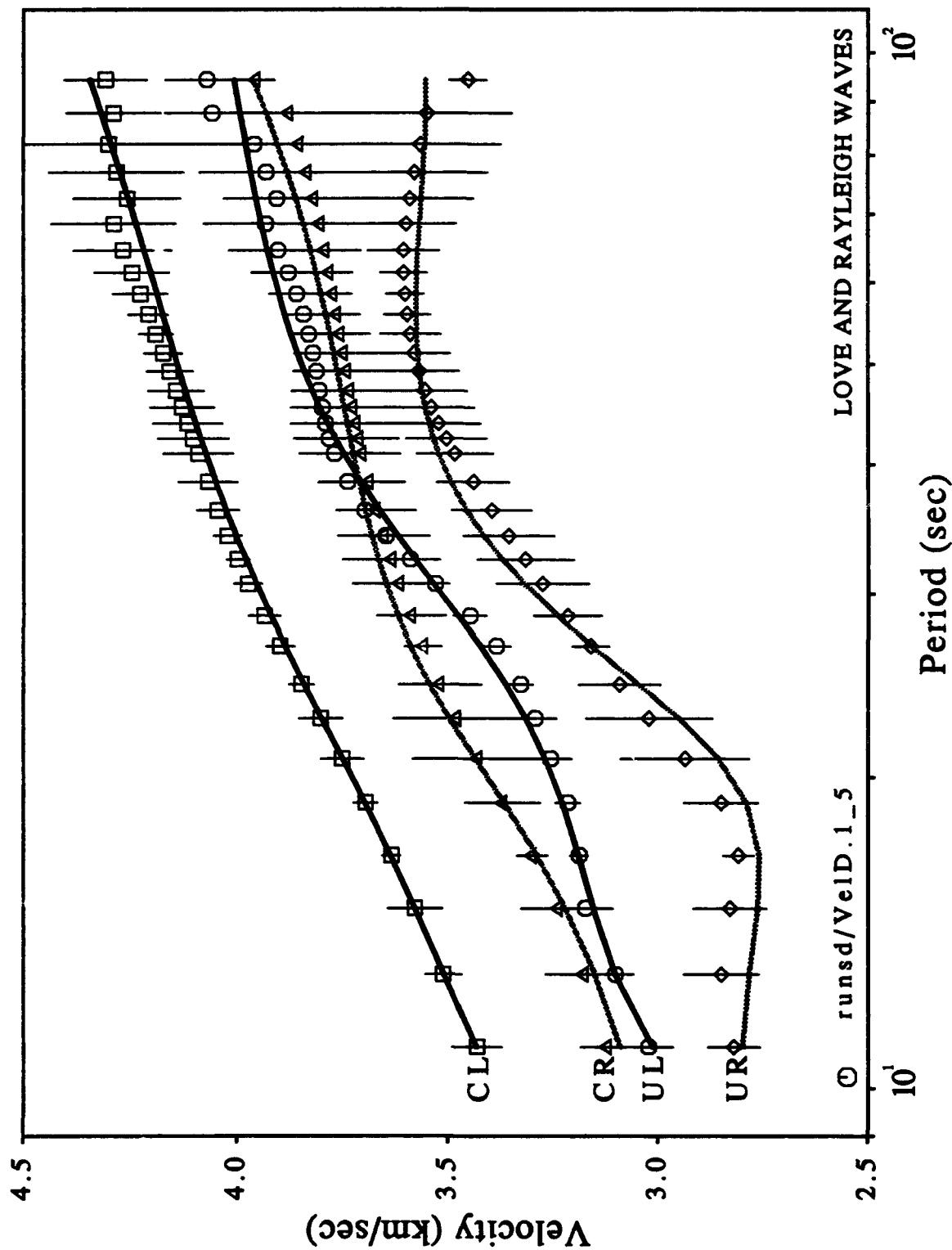


Figure 14

Velocity inversion - Rayleigh and Love waves (10-100 sec)

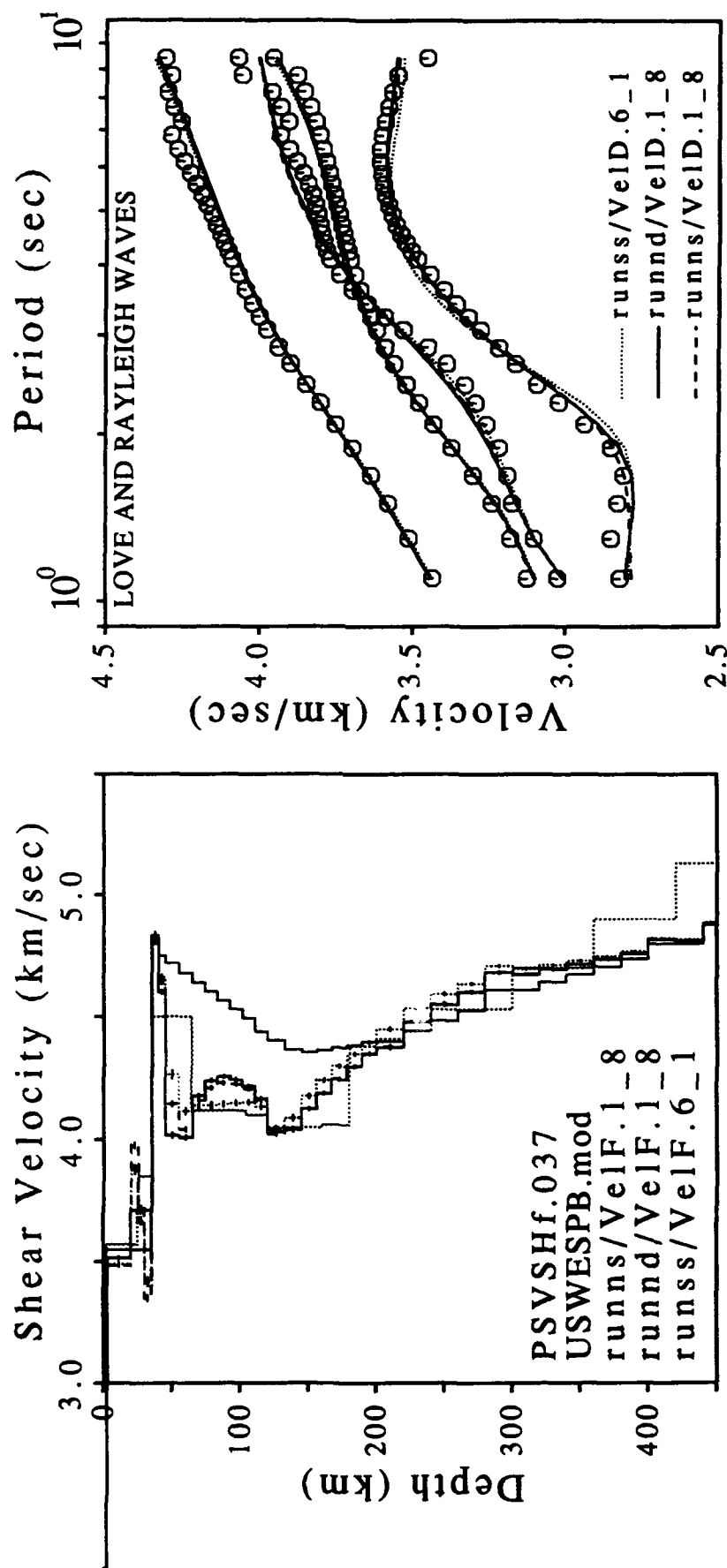


Figure 15

Prof. Thomas Ahrens
Seismological Lab, 252-21
Division of Geological & Planetary Sciences
California Institute of Technology
Pasadena, CA 91125

Prof. Keiiti Aki
Center for Earth Sciences
University of Southern California
University Park
Los Angeles, CA 90089-0741

Prof. Shelton Alexander
Geosciences Department
403 Deike Building
The Pennsylvania State University
University Park, PA 16802

Prof. Charles B. Archambeau
CIRES
University of Colorado
Boulder, CO 80309

Dr. Thomas C. Bache, Jr.
Science Applications Int'l Corp.
10260 Campus Point Drive
San Diego, CA 92121 (2 copies)

Prof. Muawia Barazangi
Institute for the Study of the Continent
Cornell University
Ithaca, NY 14853

Dr. Jeff Barker
Department of Geological Sciences
State University of New York
at Binghamton
Vestal, NY 13901

Dr. Douglas R. Baumgardt
ENSCO, Inc
5400 Port Royal Road
Springfield, VA 22151-2388

Dr. Susan Beck
Department of Geosciences
Building #77
University of Arizona
Tucson, AZ 85721

Dr. T.J. Bennett
S-CUBED
A Division of Maxwell Laboratories
11800 Sunrise Valley Drive, Suite 1212
Reston, VA 22091

Dr. Robert Blandford
AFTAC/TT, Center for Seismic Studies
1300 North 17th Street
Suite 1450
Arlington, VA 22209-2308

Dr. Stephen Bratt
ARPA/NMRO
3701 North Fairfax Drive
Arlington, VA 22203-1714

Dr. Lawrence Burdick
IGPP, A-025
Scripps Institute of Oceanography
University of California, San Diego
La Jolla, CA 92093

Dr. Robert Burrige
Schlumberger-Doll Research Center
Old Quarry Road
Ridgefield, CT 06877

Dr. Jerry Carter
Center for Seismic Studies
1300 North 17th Street
Suite 1450
Arlington, VA 22209-2308

Dr. Eric Chael
Division 9241
Sandia Laboratory
Albuquerque, NM 87185

Dr. Martin Chapman
Department of Geological Sciences
Virginia Polytechnical Institute
21044 Derring Hall
Blacksburg, VA 24061

Mr Robert Cockerham
Arms Control & Disarmament Agency
320 21st Street North West
Room 5741
Washington, DC 20451,

Prof. Vernon F. Cormier
Department of Geology & Geophysics
U-45, Room 207
University of Connecticut
Storrs, CT 06268

Prof. Steven Day
Department of Geological Sciences
San Diego State University
San Diego, CA 92182

Marvin Denny
U.S. Department of Energy
Office of Arms Control
Washington, DC 20585

Dr. Cliff Frolich
Institute of Geophysics
8701 North Mopac
Austin, TX 78759

Dr. Zoltan Der
ENSCO, Inc.
5400 Port Royal Road
Springfield, VA 22151-2388

Dr. Holly Given
IGPP, A-025
Scripps Institute of Oceanography
University of California, San Diego
La Jolla, CA 92093

Prof. Adam Dziewonski
Hoffman Laboratory, Harvard University
Dept. of Earth Atmos. & Planetary Sciences
20 Oxford Street
Cambridge, MA 02138

Dr. Jeffrey W. Given
SAIC
10260 Campus Point Drive
San Diego, CA 92121

Prof. John Ebel
Department of Geology & Geophysics
Boston College
Chestnut Hill, MA 02167

Dr. Dale Glover
Defense Intelligence Agency
ATTN: ODT-1B
Washington, DC 20301

Eric Fielding
SNEE Hall
INSTOC
Cornell University
Ithaca, NY 14853

Dan N. Hagedorn
Pacific Northwest Laboratories
Battelle Boulevard
Richland, WA 99352

Dr. Petr Firbas
Institute of Physics of the Earth
Masaryk University Brno
Jecna 29a
612 46 Brno, Czech Republic

Dr. James Hannon
Lawrence Livermore National Laboratory
P.O. Box 808
L-205
Livermore, CA 94550

Dr. Mark D. Fisk
Mission Research Corporation
735 State Street
P.O. Drawer 719
Santa Barbara, CA 93102

Prof. David G. Harkrider
Seismological Laboratory
Division of Geological & Planetary Sciences
California Institute of Technology
Pasadena, CA 91125

Prof Stanley Flatte
Applied Sciences Building
University of California, Santa Cruz
Santa Cruz, CA 95064

Prof. Danny Harvey
CIRES
University of Colorado
Boulder, CO 80309

Prof. Donald Forsyth
Department of Geological Sciences
Brown University
Providence, RI 02912

Prof. Donald V. Helmberger
Seismological Laboratory
Division of Geological & Planetary Sciences
California Institute of Technology
Pasadena, CA 91125

Dr. Art Frankel
U.S. Geological Survey
922 National Center
Reston, VA 22092

Prof. Eugene Herrin
Institute for the Study of Earth and Man
Geophysical Laboratory
Southern Methodist University
Dallas, TX 75275

Prof. Robert B. Herrmann
Department of Earth & Atmospheric Sciences
St. Louis University
St. Louis, MO 63156

Prof. Lane R. Johnson
Seismographic Station
University of California
Berkeley, CA 94720

Prof. Thomas H. Jordan
Department of Earth, Atmospheric &
Planetary Sciences
Massachusetts Institute of Technology
Cambridge, MA 02139

Prof. Alan Kafka
Department of Geology & Geophysics
Boston College
Chestnut Hill, MA 02167

Robert C. Kemerait
ENSCO, Inc.
445 Pineda Court
Melbourne, FL 32940

Dr. Karl Koch
Institute for the Study of Earth and Man
Geophysical Laboratory
Southern Methodist University
Dallas, Tx 75275

Dr. Max Koontz
U.S. Dept. of Energy/DP 5
Forrestal Building
1000 Independence Avenue
Washington, DC 20585

Dr. Richard LaCoss
MIT Lincoln Laboratory, M-200B
P.O. Box 73
Lexington, MA 02173-0073

Dr. Fred K. Lamb
University of Illinois at Urbana-Champaign
Department of Physics
1110 West Green Street
Urbana, IL 61801

Prof. Charles A. Langston
Geosciences Department
403 Deike Building
The Pennsylvania State University
University Park, PA 16802

Jim Lawson, Chief Geophysicist
Oklahoma Geological Survey
Oklahoma Geophysical Observatory
P.O. Box 8
Leonard, OK 74043-0008

Prof. Thorne Lay
Institute of Tectonics
Earth Science Board
University of California, Santa Cruz
Santa Cruz, CA 95064

Dr. William Leith
U.S. Geological Survey
Mail Stop 928
Reston, VA 22092

Mr. James F. Lewkowicz
Phillips Laboratory/GPEH
29 Randolph Road
Hanscom AFB, MA 01731-3010(2 copies)

Mr. Alfred Lieberman
ACDA/VI-OA State Department Building
Room 5726
320-21st Street, NW
Washington, DC 20451

Prof. L. Timothy Long
School of Geophysical Sciences
Georgia Institute of Technology
Atlanta, GA 30332

Dr. Randolph Martin, III
New England Research, Inc.
76 Olcott Drive
White River Junction, VT 05001

Dr. Robert Masse
Denver Federal Building
Box 25046, Mail Stop 967
Denver, CO 80225

Dr. Gary McCartor
Department of Physics
Southern Methodist University
Dallas, TX 75275

Prof. Thomas V. McEvelly
Seismographic Station
University of California
Berkeley, CA 94720

Dr. Art McGarr
U.S. Geological Survey
Mail Stop 977
U.S. Geological Survey
Menlo Park, CA 94025

Dr. Keith L. McLaughlin
S-CUBED
A Division of Maxwell Laboratory
P.O. Box 1620
La Jolla, CA 92038-1620

Stephen Miller & Dr. Alexander Florence
SRI International
333 Ravenswood Avenue
Box AF 116
Menlo Park, CA 94025-3493

Prof. Bernard Minster
IGPP, A-025
Scripps Institute of Oceanography
University of California, San Diego
La Jolla, CA 92093

Prof. Brian J. Mitchell
Department of Earth & Atmospheric Sciences
St. Louis University
St. Louis, MO 63156

Mr. Jack Murphy
S-CUBED
A Division of Maxwell Laboratory
11800 Sunrise Valley Drive, Suite 1212
Reston, VA 22091 (2 Copies)

Dr. Keith K. Nakanishi
Lawrence Livermore National Laboratory
L-025
P.O. Box 808
Livermore, CA 94550

Prof. John A. Orcutt
IGPP, A-025
Scripps Institute of Oceanography
University of California, San Diego
La Jolla, CA 92093

Prof. Jeffrey Park
Kline Geology Laboratory
P.O. Box 6666
New Haven, CT 06511-8130

Dr. Howard Patton
Lawrence Livermore National Laboratory
L-025
P.O. Box 808
Livermore, CA 94550

Dr. Frank Pilotte
HQ AFTAC/TT
1030 South Highway A1A
Patrick AFB, FL 32925-3002

Dr. Jay J. Pulli
Radix Systems, Inc.
201 Perry Parkway
Gaithersburg, MD 20877

Dr. Robert Reinke
ATTN: FCTVTD
Field Command
Defense Nuclear Agency
Kirtland AFB, NM 87115

Prof. Paul G. Richards
Lamont-Doherty Geological Observatory
of Columbia University
Palisades, NY 10964

Mr. Wilmer Rivers
Teledyne Geotech
314 Montgomery Street
Alexandria, VA 22314

Dr. Alan S. Ryall, Jr.
ARPA/NMRO
3701 North Fairfax Drive
Arlington, VA 22203-1714

Dr. Richard Sailor
TASC, Inc.
55 Walkers Brook Drive
Reading, MA 01867

Prof. Charles G. Sammis
Center for Earth Sciences
University of Southern California
University Park
Los Angeles, CA 90089-0741

Prof. Christopher H. Scholz
Lamont-Doherty Geological Observatory
of Columbia University
Palisades, NY 10964

Dr. Susan Schwartz
Institute of Tectonics
1156 High Street
Santa Cruz, CA 95064

Secretary of the Air Force
(SAFRD)
Washington, DC 20330

Office of the Secretary of Defense
DDR&E
Washington, DC 20330

Thomas J. Sereno, Jr.
Science Application Int'l Corp.
10260 Campus Point Drive
San Diego, CA 92121

Dr. Michael Shore
Defense Nuclear Agency/SPSS
6801 Telegraph Road
Alexandria, VA 22310

Dr. Robert Shumway
University of California Davis
Division of Statistics
Davis, CA 95616

Dr. Matthew Sibol
Virginia Tech
Seismological Observatory
4044 Derring Hall
Blacksburg, VA 24061-0420

Prof. David G. Simpson
IRIS, Inc.
1616 North Fort Myer Drive
Suite 1050
Arlington, VA 22209

Donald L. Springer
Lawrence Livermore National Laboratory
L-025
P.O. Box 808
Livermore, CA 94550

Dr. Jeffrey Stevens
S-CUBED
A Division of Maxwell Laboratory
P.O. Box 1620
La Jolla, CA 92038-1620

Lt. Col. Jim Stobie
ATTN: AFOSR/NL
110 Duncan Avenue
Bolling AFB
Washington, DC 20332-0001

Prof. Brian Stump
Institute for the Study of Earth & Man
Geophysical Laboratory
Southern Methodist University
Dallas, TX 75275

Prof. Jeremiah Sullivan
University of Illinois at Urbana-Champaign
Department of Physics
1110 West Green Street
Urbana, IL 61801

Prof. L. Sykes
Lamont-Doherty Geological Observatory
of Columbia University
Palisades, NY 10964

Dr. David Taylor
ENSCO, Inc.
445 Pineda Court
Melbourne, FL 32940

Dr. Steven R. Taylor
Los Alamos National Laboratory
P.O. Box 1663
Mail Stop C335
Los Alamos, NM 87545

Prof. Clifford Thurber
University of Wisconsin-Madison
Department of Geology & Geophysics
1215 West Dayton Street
Madison, WS 53706

Prof. M. Nafi Toksoz
Earth Resources Lab
Massachusetts Institute of Technology
42 Carleton Street
Cambridge, MA 02142

Dr. Larry Turnbull
CIA-OSWR/NED
Washington, DC 20505

Dr. Gregory van der Vink
IRIS, Inc.
1616 North Fort Myer Drive
Suite 1050
Arlington, VA 22209

Dr. Karl Veith
EG&G
5211 Auth Road
Suite 240
Suitland, MD 20746

Prof. Terry C. Wallace
Department of Geosciences
Building #77
University of Arizona
Tuscon, AZ 85721

Dr. Thomas Weaver
Los Alamos National Laboratory
P.O. Box 1663
Mail Stop C335
Los Alamos, NM 87545

Dr. William Wortman
Mission Research Corporation
8560 Cinderbed Road
Suite 700
Newington, VA 22122

Prof. Francis T. Wu
Department of Geological Sciences
State University of New York
at Binghamton
Vestal, NY 13901

Prof Ru-Shan Wu
University of California, Santa Cruz
Earth Sciences Department
Santa Cruz
, CA 95064

ARPA, OASB/Library
3701 North Fairfax Drive
Arlington, VA 22203-1714

HQ DNA
ATTN: Technical Library
Washington, DC 20305

Defense Intelligence Agency
Directorate for Scientific & Technical Intelligence
ATTN: DTIB
Washington, DC 20340-6158

Defense Technical Information Center
Cameron Station
Alexandria, VA 22314 (2 Copies)

TACTEC
Battelle Memorial Institute
505 King Avenue
Columbus, OH 43201 (Final Report)

Phillips Laboratory
ATTN: XPG
29 Randolph Road
Hanscom AFB, MA 01731-3010

Phillips Laboratory
ATTN: GPE
29 Randolph Road
Hanscom AFB, MA 01731-3010

Phillips Laboratory
ATTN: TSML
5 Wright Street
Hanscom AFB, MA 01731-3004

Phillips Laboratory
ATTN: PL/SUL
3550 Aberdeen Ave SE
Kirtland, NM 87117-5776 (2 copies)

Dr. Michel Bouchon
I.R.I.G.M.-B.P. 68
38402 St. Martin D'Heres
Cedex, FRANCE

Dr. Michel Campillo
Observatoire de Grenoble
I.R.I.G.M.-B.P. 53
38041 Grenoble, FRANCE

Dr. Kin Yip Chun
Geophysics Division
Physics Department
University of Toronto
Ontario, CANADA

Prof. Hans-Peter Harjes
Institute for Geophysics
Ruhr University/Bochum
P.O. Box 102148
4630 Bochum 1, GERMANY

Prof. Eystein Husebye
NTNF/NORSAR
P.O. Box 51
N-2007 Kjeller, NORWAY

David Jepsen
Acting Head, Nuclear Monitoring Section
Bureau of Mineral Resources
Geology and Geophysics
G.P.O. Box 378, Canberra, AUSTRALIA

Ms. Eva Johannisson
Senior Research Officer
FOA
S-172 90 Sundbyberg, SWEDEN

Dr. Peter Marshall
Procurement Executive
Ministry of Defense
Blacknest, Brimpton
Reading FG7-FRS, UNITED KINGDOM

Dr. Bernard Massinon, Dr. Pierre Mechler
Societe Radiomana
27 rue Claude Bernard
75005 Paris, FRANCE (2 Copies)

Dr. Svein Mykkeltveit
NTNT/NORSAR
P.O. Box 51
N-2007 Kjeller, NORWAY (3 Copies)

Prof. Keith Priestley
University of Cambridge
Bullard Labs, Dept. of Earth Sciences
Madingley Rise, Madingley Road
Cambridge CB3 0EZ, ENGLAND

Dr. Jorg Schlittenhardt
Federal Institute for Geosciences & Nat'l Res.
Postfach 510153
D-30631 Hannover, GERMANY

Dr. Johannes Schweitzer
Institute of Geophysics
Ruhr University/Bochum
P.O. Box 1102148
4360 Bochum 1, GERMANY

Trust & Verify
VERTIC
Carrara House
20 Embankment Place
London WC2N 6NN, ENGLAND